



TECHNISCHE
UNIVERSITÄT
WIEN

DISSERTATION

Improving Water-Repellent and De-Icing Surface Properties via Femtosecond Laser Structuring

for the purpose of obtaining the academic degree of

Doktor der Technik (Dr. techn.)

as part of the

Dr.-Studium der techn. Wissenschaften Maschinenbau

submitted by

Dipl.-Ing. Roland Fürbacher

Matrikelnummer 0625038

conducted at the Institute of Production Engineering and Photonic Technologies
of the Faculty of Mechanical and Industrial Engineering of the TU Wien

Supervisor: Ao.Univ.Prof. Dipl.-Ing. Dr.techn. Gerhard Liedl

Reviewers: Univ.Prof. Dipl.-Phys. Dr.-Ing. Andreas Otto
Univ.Prof. Dipl.-Ing. Dr.techn. Alexander Kaplan

Chairman of the

Examination Board: Univ.Prof. Dipl.-Ing. Dr.mont. Paul Heinz Mayrhofer

Wien, 25.07.2024



Roland Fürbacher

Gerhard Liedl

I acknowledge, that I am only entitled to print my work under the title

Dissertation

with the approval of the examination board.

Statutory declaration

Furthermore, I declare under oath, that the present work was created independently by me in accordance with the recognized principles for scientific treatises. All tools used, in particular the literature on which it is based, are named and listed in this work. The passages taken verbatim from the sources are marked as such.

The topic of this thesis has not been submitted by me to an assessor for assessment in any form as an examination paper, either in Austria or abroad. This work corresponds to the work evaluated by the assessors.

Vienna, 25.07.2024



Roland Fürbacher

Acknowledgements

This work would not have been possible without the support of the Austrian Research Promotion Agency FFG, which funded the research project NICE, on which this thesis is built. The research has been conducted at the Institute of Production Engineering and Photonic Technologies at TU Wien.

First, I would like to express my deep gratitude to my supervisor and mentor Professor Dr. Gerhard Liedl (TU Wien), for this extensive care and support. I am very grateful for the numerous discussions and the time he devoted patiently answering all my questions.

In addition to my advisor, I would like to thank Professor Dr. Andreas Otto (TU Wien) and Professor Dr. Alexander Kaplan (Luleå University of Technology) for reviewing this thesis and Professor Dr. Paul Heinz Mayrhofer (TU Wien) for chairing the examination board.

My sincere thanks also goes to my colleagues Dr. Serguei Murzin and DI Gabriel Grünsteidl for their contribution to the scientific work and to Michael Hellmold for proofreading this thesis.

I want to express my deepest gratitude to my parents, Robert and Monika, for their lifelong support and for always believing in me.

Most of all, I want to thank Jarmila, Flora, and Rosalie, my family.






Abstract

The application-specific modification of technical surfaces to increase their functional performance is becoming ever more important due to the development of new technologies. In many industrial applications where surfaces are exposed to humid and cold climates, ice formation and accumulation are inevitable unless countermeasures are taken. On the wings of wind turbines, atmospheric icing not only affects the aerodynamic performance but can also cause mass shifts on the rotor, which induce vibrations that can compromise the system's structural integrity. In addition to the resulting reduction in efficiency, there is a risk of ice being shed and thrown off the rotor blades, posing a threat to public health and safety. In severely affected areas, electro-thermal or aero-thermal heating systems are integrated into the rotor blades, which require a lot of energy to operate. Passive ice-repellent surfaces that reduce ice accumulation and promote de-icing would solve this problem. With laser structuring technology, it is possible to create superhydrophobic surfaces based on reducing surface energy and incomplete wetting. The present work deals with the laser structuring of surfaces to modify the wetting and de-icing properties to reduce freezing effects. A Titanium:Sapphire femtosecond laser is used, characterized by its ultra-short pulses and the associated high pulse energy. In experimental studies on stainless steel X5CrNi18-10 (1.4301 / AISI 304), the mechanisms and properties of so-called laser-induced periodic surface structures (LIPSS) are examined in more detail, which due to their nature and comparatively short processing time, have great potential for large-scale industrial application. Furthermore, the influence of the surface topography of different microstructures or superimposed hierarchical structures generated by selective laser ablation on their wetting and icing properties is considered based on the present work. In addition to the effect of pure laser structuring, different methods of chemical post-treatment (hydrocarbons, vacuum) were examined, which led to a significant increase in the contact angle, and a reduction in ice adhesion. During wind tunnel tests, hydrocarbon treated samples showed an improved water runback and a considerable time delay in ice bead formation on the leading edge. Since durability is essential for practical application in wind energy or aerospace sectors, experiments on the erosion resistance of laser-generated nano- and microstructures were carried out. Long-term field tests, where laser-structured samples were attached to the rotor blades of a small-scale wind turbine, confirmed the high resilience of different laser-generated structures under harsh alpine environmental conditions. Furthermore, tribological investigations showed the structure's capability to reduce the coefficient of friction. In summary, this work combines a comprehensive investigation of the potential of laser structuring in terms of targeted application-optimized surface modification with comprehensive experiments on resistance to environmental and other wear conditions. From the empirically collected data, predictions about the wetting and icing behavior of laser-structured surfaces, as well as their resistance to wear and corrosion, should be derived in the future.

Table of Content

Publication citations	I
Abbreviations	II
Variables and constants	III
1 Introduction	1
1.1 Problem	3
1.2 Objectives.....	7
1.3 Methodology	9
1.4 Synopsis	11
1.5 Scientific contribution	14
1.6 References	16
2 Publications	21
2.1. Experimental Study of Spatial Frequency Transition of Laser Induced Periodic Surface Structures.....	21
2.2. Improving Tribological Properties of Stainless Steel Surfaces by Femtosecond Laser Irradiation.....	29
2.3. Investigations on the Wetting and Deicing Behavior of Laser Treated Hydrophobic Steel Surfaces.....	41
2.4. Fast Transition from Hydrophilic to Superhydrophobic, Icephobic Properties of Stainless Steel Samples after Femtosecond Laser Processing and Exposure to Hydrocarbons	51
2.5. Icing Wind Tunnel and Erosion Field Tests of Superhydrophobic Surfaces Caused by Femtosecond Laser Processing	61

Publication citations

Paper	Citation	DOI	
1	Fuerbacher, R.; Liedl, G.; Murzin, S.P. Experimental study of spatial frequency transition of laser induced periodic surface structures. <i>Journal of Physics Conference Series</i> 2021 , vol. 1745, p. 012017.	https://doi.org/10.1088/1742-6596/1745/1/012017	
2	Murzin, S.P.; Balyakin, V.B.; Liedl, G.; Melnikov, A.A.; Fürbacher, R. Improving tribological properties of stainless steel surfaces by femtosecond laser irradiation. <i>Coatings</i> 2020 , vol. 10, 606.	https://doi.org/10.3390/coatings10070606	
3	Fürbacher, R.; Liedl, G. Investigations on the wetting and deicing behavior of laser treated hydrophobic steel surfaces. <i>Laser-based Micro- and Nanoprocessing XV</i> , 2021 .	https://doi.org/10.1117/12.2578138	
4	Fürbacher, R.; Liedl, G.; Otto, A. Fast transition from hydrophilic to superhydrophobic, icephobic properties of stainless steel samples after femtosecond laser processing and exposure to hydrocarbons. <i>Procedia CIRP</i> 2022 , vol. 111, p. 643–647.	https://doi.org/10.1016/j.procir.2022.08.016	
5	Fürbacher, R.; Liedl, G.; Grünsteidl, G.; Otto, A. Icing wind tunnel and erosion field tests of superhydrophobic surfaces caused by femtosecond laser processing. <i>Wind</i> 2024 , vol. 4., p. 155-171.	https://doi.org/10.3390/wind4020008	

Abbreviations

AFM	Atomic force microscopy
AISI	American Iron and Steel Institute
CC	Cold climate
CFD	Computational fluid dynamics
CPA	Chirped pulse amplification
DE	Deutschland/Germany
DIN	Deutsches Institut für Normung
DLA	Direct laser ablation
DLIP	Direct laser interference patterning
E	Erosion
EU	European Union
FFG	Austrian Research Promotion Agency
FHJIWT	FH Joanneum icing wind tunnel
FFT	Fast Fourier transform
GDD	Group delay dispersion
GSM	Global system for mobile communications
HSFL	High spatial frequency laser induced periodic surface structures
HV	Vickers hardness
IC	Icing climate
iCVD	Initiated chemical vapor deposition
ID	Identification
IEA	International Energy Agency
IPS	Ice protection system
IREA	International Renewable Energy Agency
ISO	International Organization for Standardization
IWT	Icing wind tunnel
LIPSS	Laser induced periodic surface structures
LSFL	Low spatial frequency laser induced periodic surface structures
LTC	Low-temperature climate
LWC	Liquid water content
MVD	Median volume diameter
NACA	National Advisory Committee for Aeronautics
PDMS	Polydimethylsiloxane
pDVB	Poly-divinyl benzene
PE	Polyethylene
PE-HD, HDPE	High-density polyethylene
PFA	Perfluoroalkoxy alkane
PFOTES	1H, 1H, 2H, 2H-perfluorooctyltriethoxysilane
PMMA	Polymethyl methacrylate
pPFDA	Poly-perfluorodecylacrylate
PTFE	Polytetrafluoroethylene
RON	Research octane number
SEM	Scanning electron microscopy
SLIPS	Slippery liquid infused porous surface
SPP	Surface plasmon polariton
Ti:Sa	Titanium:Sapphire
TKS	Tecalemit-Kilfrost-Sheepbridge Stokes
TEM	Transverse electromagnetic mode
TM	Transverse mode
UAV	Unmanned aerial vehicle
USTEM	University Service Centre for Transmission Electron Microscopy
XPS	X-ray photoelectron spectroscopy; Extruded polystyrene

Variables and constants

a	Gap width, hatch [μm]
A_{oA}	Angle of attack [$^{\circ}$]
α, Θ	Angle of incidence [$^{\circ}$]
c	Chord length [mm]
CAH	Contact angle hysteresis [$^{\circ}$]
d	Laser beam diameter [μm]
e	Euler's number
η	Real part of the effective index of the surface plasmon mode
f	Feed rate [mm/s]
ϕ, φ	Laser fluence [J/cm^2]
k	Sain-grain roughness [μm]
k_s	Equivalent sand-grain roughness [μm]
k_{RMS}	Root-mean-square roughness height [μm]
λ	Incident laser wavelength [nm]
λ_c	Roughness cut-off wavelength [nm]
λ_{LSFL}	Spatial LSFL period [nm]
λ_{HSFL}	Spatial HSFL period [nm]
$\Lambda, \Lambda_{\text{LIPSS}}$	Spatial LIPSS period [nm]
n	Number of laser pulses
RH	Relative humidity [%]
RoA	Roll-off angle [$^{\circ}$]
Rq	Root mean square roughness [μm]
Sa	Arithmetical mean height [μm]
SCA	Static contact angle [$^{\circ}$]
Sdr	Developed interfacial area ratio [%]
s_k	Skewness
Ssk	Area skewness
Sq	Root mean square height [μm]
Sz	Maximum height [μm]
T	Temperature [$^{\circ}\text{C}$]

1 Introduction

The demand for environmentally friendly energy generation significantly impacts the global energy market and has led to a steady expansion of renewable energy in recent decades. In 1990, the share of renewable energy in global electricity production was about 18.4%, with 18.3% generated by hydropower and only 0.03% by wind power [1]. In 2022, the share of renewable energy was already 29.9%, with the expansion of wind power to 7.5%, and solar power at 4.5% being the strongest drivers of this significant change. To drive global decarbonization and achieve the goal of a renewable and clean energy future, a study by the International Renewable Energy Agency (IREA) shows that the share of wind power in the overall energy mix would need to increase to 35% by 2050, which would be technically and economically feasible [2]. The European Union passed a climate law in 2021, including climate targets for reducing greenhouse gases, the energy transition, and climate neutrality by 2050. Accordingly, by 2030, the share of renewable energy should be increased to at least 32%, whereas in 2022, it was in the range of 22%, but above the set target of 20% [3]. In Austria, the federal government passed the "Bundesgesetz über den Ausbau von Energie aus erneuerbaren Quellen" in 2021, intending to implement the coverage of 32% of gross energy consumption by renewable energy by 2030, as required by the EU, and achieve climate neutrality by 2040 [4]. This results in a demand for wind turbines, which, due to the increasing scarcity of available land in the lowlands and the further development of technology, makes the installation of turbines in mountainous locations more attractive for operators. Aside from the ecological consequences, the disadvantages of developing alpine terrain which typically consists of a more exposed area, can lead to higher installation and maintenance costs, as well as more intensive winter periods. The risk of icing of wind turbines increases in most cases with the altitude of the site. However, this risk always depends on the local climate conditions, and in the Alpine region, it applies mainly to sites at altitudes 1000 m above sea level [5]. The International Energy Agency (IEA), classifies "cold climate" (CC) sites into low-temperature climate (LTC) and "icing climate" (IC) sites. To be classified as LTC, the site must have an air temperature of < -20 °C on more than nine days per year and an average annual temperature of < 0 °C [6]. IC sites are characterized by having instrumental icing above 1% of the year and meteorological icing above 0.5% of the year. Instrumental icing is the period during which ice formation is visible on the structure or instruments, and meteorological icing is the period during which weather conditions allow ice formation. Regardless of this classification, ice formation is also strongly dependent on the prevailing humidity or liquid water content (LWC), temperature, and wind speed, which are also subject to substantial local and seasonal changes [7]. From a meteorological point of view, the origin of the eventual icing of structures close to the ground lies in the formation of droplets by condensation on dust particles, which leads to a droplet size of > 4 μm [8]. These cloud droplets can grow to a median volume diameter (MVD) of up to 0.5 mm by further condensation. Larger drops can be formed by the formation of ice crystals in the cloud, which grow until they become too heavy and fall into lower air layers, where they either liquefy again (rain), liquefy and cool below 0 °C again (supercooled rain), or continue to arrive frozen as snow [8]. This process is referred to as precipitation icing concerning the icing of ground-level structures and is distinguished from in-cloud icing (Table 1) [9]. In-cloud icing is the presence of suspended supercooled water droplets that are accelerated by the wind and flash freeze on the wind turbine. It is the most common icing process and conditions tiny water droplets with $\text{MVD} < 50$ μm [7].

Depending on the icing conditions, distinguishable ice types can be formed: glaze ice and rime ice [9]. Glaze ice forms during freezing rain or wet in-cloud icing and is characterized by a transparent appearance. It has a higher density than rime ice and adheres very firmly to the surface [10]. Rime ice, on the other hand, forms when wind carries supercooled water droplets against a surface, causing them to freeze abruptly. It is the most common type of ice and can be classified as soft rime or hard rime depending on the droplet size (Table 1) [9]. Soft rime is a fragile formation comparable to snow that adheres weakly to surfaces, whereas hard rime is a much more rigid, needle-like formation that adheres firmly. Ice growth always occurs in the direction of the water-bearing wind and can reach rates of over 70 mm/h [11].

Table 1: Meteorological parameters controlling atmospheric ice accretion and ice properties [8], [9], [12], [13], [14], [15].

Type of ice	Air temperature [°C]	Wind speed [m/s]	Droplet size, MVD [mm]	Liquid water content in air, LWC [g/m ³]	Density [kg/m ³]	Adhesion an cohesion	Color
Precipitation icing							
Glaze (freezing rain or drizzle)	$-10 < t < 0$	any	0.1 - 5	0.05 - 0.5	900	strong	transperent
Wet snow	$0 < t < +3$	any	flakes	lwc_s [16]	300 - 600	weak (forming) strong (frozen)	white
In-cloud icing							
Glaze		0.1 - 0.5	5	900	strong	transperent	
Hard rime		0.1 - 0.5	0.1	600 - 900	strong	opaque	
Soft rime		0.02 - 0.1	0.01 - 0.30	200 - 600	low - medium	white	

1.1 Problem

The risks coupled with the icing of wind turbines can be divided into three categories: Personal safety, operational safety, and economic efficiency. Ice accumulation usually starts at the leading edges of the rotor blade tips (wing tips), where the highest circumferential speed of up to 300 km/h prevails. Introducing a disturbance, such as load-cycle induced oscillation of the flexible fiber composite rotor blades or a natural defrosting process, can lead to the loosening/shearing of ice sections and, thus, to parabolic shedding [16]. Such a fragment typically weighs 100-1000 g and is highly likely to impact within a 300 m radius of the wind turbine, but it depends on the rotor diameter and hub height [17], [18]. Therefore, special ice protection measures must be taken at sites with potential personal hazards.

Furthermore, even slight ice accumulation on the rotor blades leads to disturbed aerodynamics and, thus, to a reduction in lift force and an increase in drag (Fig. 1) [19], [20]. An asymmetric mass distribution can develop as icing progresses, leading to imbalance, rotor blade oscillations, and increased tower vibrations [21]. All this puts additional stress on the structure and mechanics (gearbox) and increases the maintenance effort and consequently the operating costs of the affected turbine [22].

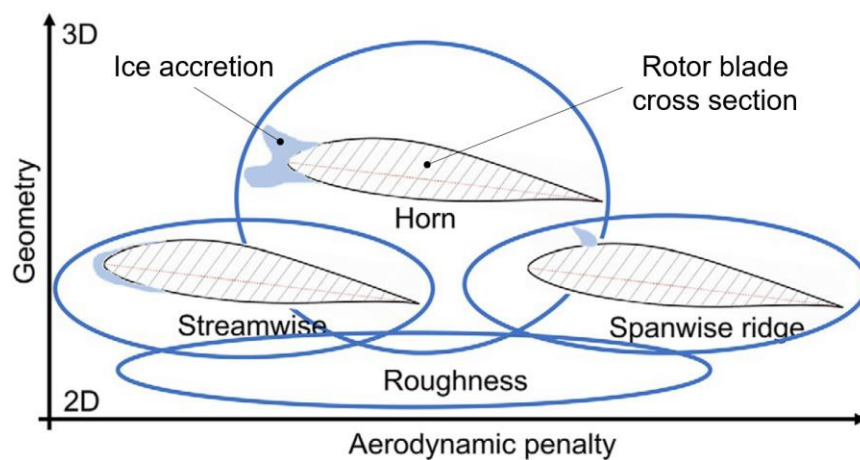


Figure 1: Aerodynamic effects for various airfoil ice shapes [7], [23].

The disturbance of aerodynamics due to icing of the rotor blades has a substantial impact on the efficiency of the wind turbine and leads to significant power losses of 20 - 30% [20], [24], [25], [26]. In weather conditions that are particularly negative for operation, the power losses can also increase further to 80% [27] until the technically necessary shutdown [28]. Depending on the geographical location of the site and meteorological conditions, annual power production can be significantly reduced due to icing:

- Jura, Switzerland: 10%, 2000 kW, without IPS [29].
- Apennines, Italy: 19%, 400 kW, without IPS [30].

To reduce ice accumulation and thus the risks, so-called Ice Protection Systems (IPS) can be used as anti-icing and/or de-icing measures. Anti-ice measures are applied to delay or completely prevent ice formation. De-icing measures aim to reduce ice adhesion to the surface and promote (natural) removal. Both types of measures can be divided into active and passive systems, depending on whether energy is required to function (Table 2) [22].

Table 2: Comparison of different ice protection systems [7], [22].

IPS	Anti-Ice	De-Ice	Working principle	Advantage	Disadvantage
Active					
Thermal	✓		heating resistance or warm air flow	no ice accumulation in moderate icing conditions	energy consuming, risk of overheating
Air layer	✓		hot air flow through holes in leading edge	effective when applied	not verified
Microwave	✓		heating of blade surface via microwaves	effective when applied	not implemented
Heating resistance		✓	electrical heating	effective, efficient, commercially available	failing of one heater causes imbalance
Warm air and radiator		✓	hot air flow through tubes in rotor blades	effective when applied	energy consuming, blades act as insulator
Flexible pneumatic boots		✓	ice shedding, via inflation of flexible boots	low energy consumption	high maintenance
Electro impulse/expulse		✓	electromagnetically induced vibration	efficient, low energy consumption	not implemented, ice expulsion
Active-passive					
Chemicals (TKS)	✓		lowering water freezing temperature	effective when applied	complex system, pollution, high maintenance
Active pitching	✓	✓	orientation of blades into the sun and heating via absorption	low cost, effective in LTC locations	not verified, may damage wind turbines
Passive					
Special coating	✓		anti-adherent, superhydrophobic	low cost	low erosion resistance, not very effective, regular maintenance
Black paint	✓		heating through sunlight absorption	low cost, effective in direct sunlight	potential overheating during summer
Flexible blades		✓	ice shedding via bending	not verified	not verified

Two of these IPS have been implemented commercially in large wind turbines, and both are based on heating [7], [31]. In the electro-thermal IPS, heating elements are laminated in the leading edge region and activated when needed. These can be wire or carbon fiber nets incorporated just below the top fiber composite layer of the rotor blades. The energy requirement of electrical heating systems is about 6 - 12% of the rated power of the wind turbine [31]. In the second commercially available IPS, a hot air stream is circulated inside the rotor blade shell utilizing fans. The fans are usually located in the blade hub, and the heater is in the nacelle. Hot air systems require about 10 - 15% of the rated power of the wind turbine [32].

The use of thermal IPS for ice mitigation requires energy and thus reduces the power output during the IPS usage period but increases the overall annual efficiency of the plant by extending the total usage period or increasing the efficiency during operation in icing conditions. Compared to the above examples of reduction in annual electricity production due to icing, the following examples show the losses using IPS:

- Yukon, Canada: 20%, 150 kW, with IPS [33].
- Jura, Switzerland: 3.5%, 2000 kW, with IPS [29].
- Kvitfjell, Norway: 4.5%, 4200 kW, with IPS [30].

Comparing the experimental plant in Switzerland, it is evident that operation with IPS reduced the annual power losses from 10% to 3.5%. This underscores the functionality and economic viability of the currently used IPS, despite their energy consumption. However, it's important to note that passive IPS, such as coatings, are not yet commercially available but hold significant potential for future energy-saving ice protection of wind turbines. In addition to energy savings during operation, coatings can lead to weight reduction and lower maintenance requirements by eliminating all components of thermal IPS. This potential has sparked intensive research into coatings for wind turbine ice protection.

A categorization of passive anti-icing surfaces, which are caused by a modification of the surface and are commonly grouped under the term "coatings," can be made based on their mechanisms of action [34], [35], [36]:

- Surfaces with low surface energy (PTFE)
- Surfaces with roughness (Cassie-Baxter wetting state, structuring, lithography)
- Surfaces with mechanical properties (stress localization, viscoelastic polymers)
- Surfaces with thermo-physical properties (phase transformation materials)
- Surfaces with chemical properties (freezing point depression, proteins)
- Surfaces with liquid wetting (hydrate shells, SLIPS)

Coatings are designed to enhance anti-icing and de-icing properties, typically using wetting properties to measure anti-icing performance. Superhydrophobic surfaces, which are characterized by a low contact zone and low adhesion between water droplets and the surface (high contact angle, low roll-off angle), play a crucial role in deflecting impinging water droplets before they freeze. This prevention of ice accumulation is a significant aspect of current research [37]. Once the ice has formed, icephobic surfaces should minimize ice adhesion. This property is essential so the ice can be easily removed from the surface, e.g., by wind, vibrations, or gravity. To assess the effectiveness of deicing, various methods can be used to determine ice adhesion [38], allowing conclusions to be drawn about the mechanical interlocking between ice and surface [39]. Beeram [40] compared the wettability and ice adhesion of different materials and coatings using the push-test [41]. Table 3 provides a glimpse of current research results on different materials and modified anti-ice surfaces, underlining the importance of this work.

Superhydrophobic wetting properties can be achieved by various coatings but also by structuring surfaces, an idea that originated in nature (lotus effect). Stochastic or periodic structuring can create the conditions for an incomplete wetting state (Cassie-Baxter wetting state). In this case, air pockets forming in the structure cause a reduced contact zone between the water droplet and the surface, preventing the penetration of the liquid [42]. Nano- and microstructures can be transferred to engineering surfaces by various methods, e.g.:

- Lithography [43], [44]
- Thermal imprinting [45]
- Wet chemical reaction [46]
- Coating [47]
- Laser structuring [48], [49]

A major problem of many coating systems is the limited erosion resistance to the environmental conditions prevailing at wind turbines, such as dust, rain, and hail. Combined with strong winds resulting in high rotor speeds, dust and precipitation already cause major erosion damage to conventionally manufactured rotor blades made of fiber composite materials, especially at the leading edge [50]. This damage causes turbulence and early flow separation, negatively affecting efficiency and reducing annual energy production by up to 25% in extreme cases [51]. For this reason, research is currently being conducted into ice-repellent coatings with high erosion resistance [52].

An alternative to polymer coatings is structuring surfaces to reduce ice adhesion. As already mentioned, structuring can lead to superhydrophobic wetting properties, which, cannot be equated with low ice adhesion, since other mechanisms are essential here [53], [54]. During phase transition, mechanical interlocking between water/ice and surface structure can occur, negatively affecting and increasing ice adhesion [55].

However, the potential of laser structuring is not limited to creating an incomplete wetting state. It offers the possibility of altering the surface chemistry, in addition to creating an incomplete wetting state [56]. This potential has led to the objective of this dissertation, which is to generate laser-structured, superhydrophobic surfaces with advanced ice-repellent properties.

Table 3: Static water contact angle and ice adhesion values for different materials and modifications.

Substrate Material	Surface Modification	Static water contact angle [°]	Ice adhesion		Reference
			Method	Result [kPa]	
Aluminum 6061	-	68	Cuvette-encased ice columns, Push-test	520	[40]
Stainless steel AISI 316	-	75	Cuvette-encased ice columns, Push-test	560	[40]
PMMA (Acrylic)	-	73	Cuvette-encased ice columns, Push-test	330	[40]
PTFE (Teflon)	-	95	Cuvette-encased ice columns, Push-test	420	[40]
PFA	-	101	Cuvette-encased ice columns, Push-test	570	[40]
Stratasys VeroWhite	-	39	Cuvette-encased ice columns, Push-test	390	[40]
Aluminum 6061	Rust-Oleum Enamel	65	Cuvette-encased ice columns, Push-test	1400	[40]
Aluminum 6061	Rust-Oleum NeverWet	153	Cuvette-encased ice columns, Push-test	510	[40]
Aluminum 6061	Rust-Oleum Hydrobead	159	Cuvette-encased ice columns, Push-test	400	[40]
Titanium Ti64	MecaSurf perfluoropolyether compound	51	Cantilever ice adhesion test	53	[48]
Titanium Ti64	Laser-generated structures "DLIP" + MecaSurf perfluoropolyether compound	163	Cantilever ice adhesion test	19	[48]
Titanium Ti64	Laser-generated structures "LIPSS" + MecaSurf perfluoropolyether compound	166	Cantilever ice adhesion test	33	[48]
Titanium Ti64	Laser-generated structures "LOTUS" + MecaSurf perfluoropolyether compound	168	Cantilever ice adhesion test	33	[48]
Titanium Ti64	Laser-generated structures "ROUGH" + MecaSurf perfluoropolyether compound	169	Cantilever ice adhesion test	63	[48]
Titanium Ti64	Laser-generated structures "POROUS" + MecaSurf perfluoropolyether compound	168	Cantilever ice adhesion test	77	[48]
Steel	Cross-linked polymeric bilayer films, pDVB/pPFDA (iCVD)	152	Cuvette-encased ice columns, Push-test	208	[57]
Silicon	Cross-linked polymeric bilayer films, pDVB/pPFDA (iCVD)	149	Cuvette-encased ice columns, Push-test	172	[57]
PDMS	-	52	Cuvette-encased ice columns, Push-test	1210	[58]
PDMS	Silica particles (20 - 30 nm), content: 30%	115	Cuvette-encased ice columns, Push-test	55	[58]
PDMS	SLIPS via application of silicon oil	120	Cuvette-encased ice columns, Push-test	40	[58]
Aluminum 1100	-	46	Ice columns, Push-test	1360	[59]
Aluminum 1100	K100-F13-PPy-Al (SLIPS-Al)	117	Ice columns, Push-test	16	[59]
Glass	Sol-gel coating PFOTES-SiO ₂ + SiO ₂ nanoparticles, weight ratio 1:5	160	Cuvette-encased ice columns, Push-test	490	[53]
Glass	Sol-gel coating PFOTES-SiO ₂ + SiO ₂ nanoparticles, weight ratio 6:0	168	Cuvette-encased ice columns, Push-test	50	[53]
Stainless steel 1.4301	-	68	Cuvette-encased ice columns, Push-test	820	Paper 4
Stainless steel 1.4301	Laser-generated structures "Grid" + petrol treatment	160	Cuvette-encased ice columns, Push-test	410	Paper 4
Stainless steel 1.4301	Laser-generated structures "LIPSS" + vacuum treatment	148	Cuvette-encased ice columns, Push-test	250	Paper 4

1.2 Objectives

The objectives of this work were to research and develop passive, water- and ice-repellent surfaces by laser structuring for application on wind turbines. In terms of time, the objectives were regularly adjusted depending on the interim results achieved, resulting in the following chronology:

- At the beginning of the research, the focus was on generating superhydrophobic surfaces by structuring with the femtosecond laser. By reducing the contact area, an incomplete wetting (Cassie-Baxter wetting state) should be achieved, which favors the roll-off/repellence of applied water droplets. The basic idea was that superhydrophobic surfaces could reduce ice adhesion. For this purpose, different structure types were created by direct laser ablation and by processing in the ablation threshold region of the substrate material. The latter can lead to the formation of laser induced periodic surface structures (LIPSS) [60], the geometric expression of which was part of the initial investigations.

During this work, it was found that the wetting behavior is time-variable, i.e., a chemical conversion from superhydrophilic to hydrophobic occurs after laser processing, with the conversion time depending on the structure type. From this, the following research objectives were derived:

- The investigation of the transformation time from hydrophilic to hydrophobic after laser processing depending on the structure type, which was evaluated periodically by measuring the static water contact angle. In addition, the ice adhesion after the transformation was to be investigated to derive a structure dependence on the one hand and to test the durability of the uppermost surface layers by repeated ice adhesion measurements on the other hand.
- A selection of laser-generated structures was tested for their coefficients of friction, a crucial tribological property.

Based on the experimental results, it was deduced that the following parameters are decisive for the formation of a superhydrophobic surface:

- The structural geometry (incomplete wetting) and
- The chemical change due to laser processing (reduction of surface energy).

It became clear that chemical transformation is a significant contributor to surface modification by laser processing. During a related research, methods for accelerating the chemical transformation and the associated hydrophobization of the surface were found, as well as the underlying process of chemisorption of hydrocarbons on the oxidized metal surface [53], [56], [61]. This information was used for further experimental design and set goals for an alternative process to reduce the conversion time after laser processing:

- Direct exposure of the laser-structured samples to an atmosphere enriched by hydrocarbons and study the effect of different hydrocarbons on the wetting and deicing properties.
- Use of advanced analytical techniques (X-ray photoelectron spectroscopy, XPS) to obtain information about the chemical changes on the surface.

These investigations showed a significant acceleration of the wetting transformation time from hydrophilic to hydrophobic, and a significant reduction of ice adhesion after immersion in gasoline or storage in a high vacuum. Subsequent XPS analysis revealed surface enrichment with non-polar carbon (C-C, C-H components). To assess the potential of the results obtained in the simplified laboratory test with respect to an application on a wind turbine, the focus of further work was determined as follows:

- To perform anti-ice experiments in an icing wind tunnel to validate the performance of laser-structured and post-treated steel samples under more realistic, dynamic icing conditions. To simulate the aerodynamic shape and inflow of a rotor blade, thin, laser-structured metal foils were to be attached to airfoil segments. The tests should be carried out under calibrated glaze-ice conditions and the resulting ice shape at the leading edge should be measured using a 3D laser scanner. From this, insights into the initial icing phase as well as the resulting ice shape in direct comparison to an unstructured reference surface should be derived.
- To test the erosion resistance of various structures generated by femtosecond laser processing on steel under real environmental conditions, a test rig consisting of a small wind turbine and

meteorological measuring equipment was set up at an alpine location. The laser-structured steel foils were attached to the leading edges of the rotor blades by means of adhesives and exposed to operating conditions for an entire winter. In this experiment, the focus was not on the function but exclusively on the durability and was to be evaluated by comparing the structural geometries before and after the long-term test.

1.3 Methodology

The present work was conducted using a range of empirical research methods to illuminate the underlying scientific question. The range of investigation methods extended from basic research to application-oriented experiments in the field. Stainless steel (X5CrNi18-10 / 1.4301 / AISI 304) was used as substrate material due to its broad industrial applicability. The tool used, the Titanium-Sapphire (Ti:Sa) femtosecond laser, was regularly maintained and adjusted during the experiments to ensure reliable and reproducible processing. This is very important because the laser system is a complex laboratory device that is very sensitive to, e.g., thermal changes. It consists of four major components: the oscillator, the stretcher, the amplifier stage, and the compressor (Fig. 2). In the oscillator, ultra-short light pulses (10 fs) are generated by mode locking, exploiting the Kerr lens effect utilizing a soft aperture in the nonlinear titanium (Ti^{3+}) doped sapphire (Al_2O_3) laser medium. The laser pulses generated in the oscillator have a repetition rate (about 78 MHz) that depends on the length of the resonator and a relatively low pulse energy (about 5 nJ). To allow material processing, the pulse energy must be significantly increased – in the case of this system to approx. 0.8 mJ. For this purpose, an amplifier stage was added to the laser system, in which another Ti:Sa laser crystal amplifies the pulses coming from the oscillator. In total, the pulse train passes through the amplifier crystal nine times and is further amplified with each pass. The stretcher is located between the oscillator and the amplifier stage, which uses dispersion (positive group delay dispersion - GDD) to spatially and temporally lengthen the broadband laser pulses ($\Delta\lambda \approx 80$ nm) by a factor of 10^5 , thereby preventing destruction of the amplifier crystal (by self-focusing) as it passes through (chirped pulse amplification - CPA). After four of nine amplification passes through the amplifier crystal, the repetition rate is reduced from 78 MHz to 1 kHz using an electro-optical modulator (Pockels cell) - thus the pulse energy of the remaining pulses can be significantly increased. After another 5 passes through the amplifier crystal, the pulse train enters the prism compressor, where different path lengths for different wavelengths are realized via angular dispersion (negative GDD), resulting in a compression of the previously expanded pulses. The pulse train is then decoupled from the laser system and is ready for processing by the user. After the decoupling, the pulse duration is about 30 fs with a reduced bandwidth of about 40 nm (mostly due to gain narrowing).

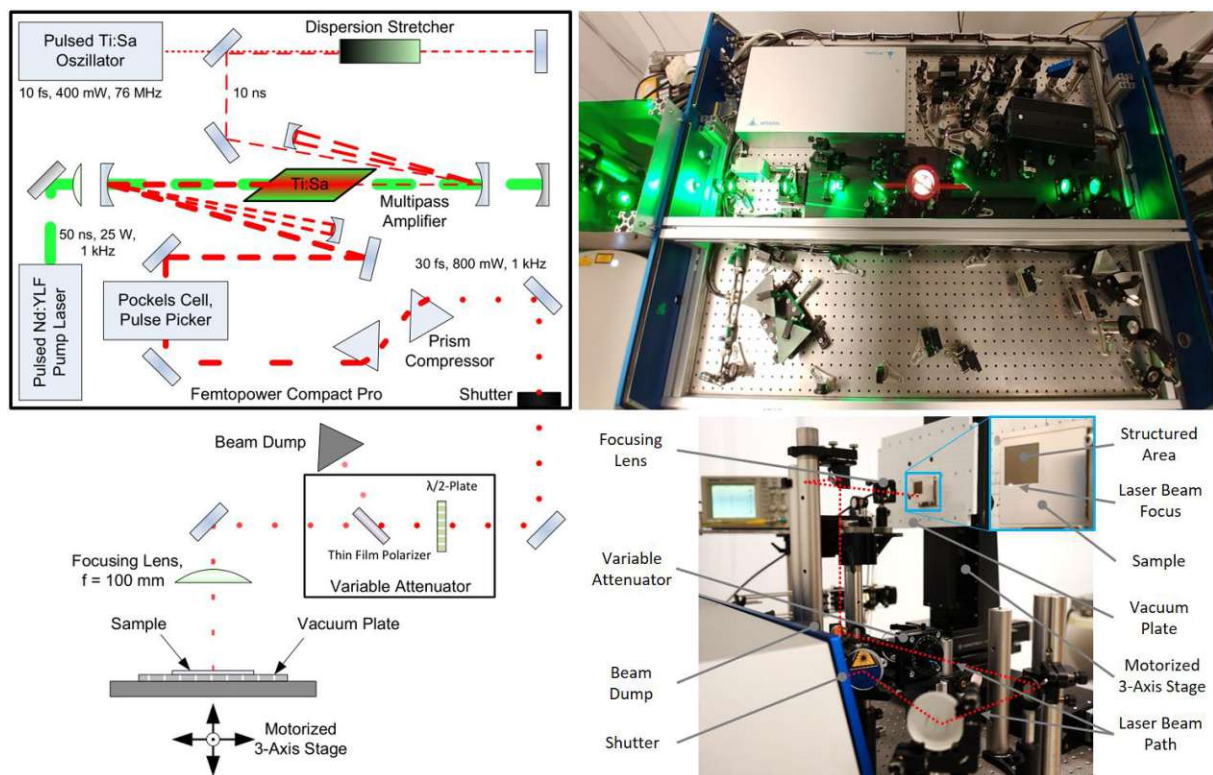


Figure 2: Schematic depiction of the Femtopower Compact Pro Ti:Sa femtosecond laser system (left), real laser system and opto-mechanical setup for nano- and microstructuring (right).

Since the structures generated by direct laser ablation (DLA) are composed of nano- and micro-geometries, a 3D profilometer (Alicona Infinite Focus), and a scanning electron microscope (SEM, Jeol JCM-5000) were utilized to characterize them. To determine the structural depth of the LIPSS, an atomic force microscope (AFM) was used. Another important geometrical parameter of LIPSS is the spatial frequency of the wave-like formations, which was evaluated by frequency analysis of the generated SEM images.

To characterize the wetting properties of the modified surfaces, a commercially available contact angle goniometer (Dataphysics OCA25) was used. The goniometer can be used to determine the contact angle hysteresis and roll-off angle in addition to the static contact angle.

Since the primary goal of this dissertation was determined to be the reduction of ice accumulation on rotor blades or airfoils, methods for quantifying the icing tendency of surfaces had to be found/selected/defined. A literature search led to the so-called push-test, in which a defined column of ice is frozen on the flat sample to be investigated and then sheared off by means of a force probe. The force required is recorded, which, taking into account the iced interface area, yields the shear stress. Since no commercial systems for measuring ice adhesion were available, such a test rig was developed and built.

The load cell (HBM Typ S2 500N) was calibrated using test weights. With this measuring method, it is essential to note that the induced force is ideally applied at the level of the interface, which is not possible in practice. This leads to systematic errors since the actual stress is composed of shear and tension. For this reason, the height of the push force application point was not changed for all experiments performed.

To shorten the transformation time from hydrophilic to (super)hydrophobic, the laser-structured samples were stored in a hydrocarbon atmosphere or directly in the liquid on the one hand and in a vacuum on the other hand. For this purpose, chemical-resistant, tightly sealable (PE-HD) containers and a vacuum chamber of a SEM (Jeol JCM-5000) were used.

Chemical analysis of the modified surfaces was performed by X-ray photoelectron spectroscopy (XPS) utilizing a SPECS instrument with an Al-K α X-ray source (μ Focus 350) and a hemispherical WAL-150 analyzer. This method allows quantifying the chemical components of a surface and is very sensitive in the range of the uppermost nanometers. The measured data was analyzed in CASA XPS software, using reference tables [62] and [63] to fit the peaks.

The performance of the laser-processed and hydrocarbon/vacuum-treated samples under impact icing conditions was tested in the FH JOANNEUM small-scale icing wind tunnel (FHJIWT) [64]. The FHJIWT is a calibrated closed-loop atmospheric wind tunnel of Göttingen configuration and can simulate in-flight icing conditions. Calibrated glaze ice conditions were used for the experiments, where the mean volume diameter (MVD) of the generated water droplets and the liquid water content (LWC) of the air stream were kept in a defined range. 3D laser measurements of the ice shapes were performed to obtain more information on the ice accumulation. The utilized scanning system was a portable 3D laser measurement system consisting of a Hexagon Absolute Arm and an RS6 laser-scanning head with a system accuracy of 48 μ m and a minimum point distance of 11 μ m.

The field test to investigate the erosion resistance of laser-structured stainless steel samples was carried out at an alpine site (Pretul) at 1600 meters above sea level in the Austrian Alps. Over a period of six months, specimens attached to the rotor blades of a small wind turbine were exposed to the dynamic operating and weather conditions typical of this location during winter. Instruments for meteorological measurements were installed on a 10 m high mast to collect weather data. The data was collected by a data logger and transmitted via GSM module. An Ammonit AB 100 sensor was used to measure the air pressure. The wind direction and wind force were measured using an ultrasonic anemometer (Thies 3D Ultrasonic). In addition, an icing sensor from Eologix (CET214) was used, which recorded not only the icing events but also the temperature and humidity of the ambient air.

1.4 Synopsis

The subsequent publications can essentially be described as building on another chronologically and scientifically. This includes numerous experiments to investigate the effect of laser processing itself, as well as the application of various structures on the wetting behavior of steel surfaces and the resulting ice adhesion. Both properties depend on two factors: the geometry or topography of the laser-generated surface, as well as its chemical composition. Table 4 shows an overview of the research work carried out during this dissertation.

Table 4: Scientific focus of the publications that are content of this thesis.

Research subjects	Paper 1 (2.1)*	Paper 2 (2.2)	Paper 3 (2.3)*	Paper 4 (2.4)*	Paper 5 (2.5)*
Laser induced periodic surface structures	✓	✓	✓	✓	✓
Laser surface structuring	✓	✓	✓	✓	✓
Friction		✓			
Wetting			✓	✓	✓
De-Icing			✓	✓	✓
Hydrocarbon treatment				✓	✓
Erosion resistance					✓
Icing wind tunnel performance					✓
Surface roughness (SEM, 3D profile)	✓	✓	✓	✓	✓
Surface chemistry (XPS)				✓	✓

*as lead author

An initial work (Chapter 2.1), investigated the machining parameter window for producing LIPSS [65] on steel 1.4301 using a Ti:Sa femtosecond laser source. The focus was on the variation of the fluence, the number of applied laser pulses and the resulting LIPSS properties. In principle, LIPSS can be differentiated between low spatial frequency LIPSS (LSFL) and high spatial frequency LIPSS (HSFL) based on the resulting spatial frequency [60]. Their characteristics mainly depend on the laser wavelength, polarization, and the applied fluence, but also on the number of applied pulses. A Fast Fourier transform (FFT) of the SEM images was used to examine the change in the HSFL/LSFL ratio and the transition into the ablation regime. It turned out that in the low fluence range, an increase in the number of pulses leads to a spatial frequency shift towards HSFL. The transition to the ablation regime, which is indicated by the formation of grooves and later cones, began at higher fluences with a lower pulse number and showed a very interesting correlation: with increasing fluence and pulse number, the cones showed an increase in structure size when measured at the cone base. These relationships were novel at the time the work was written.

Based on the structures created, two areas of application were of particular interest: changing the wetting properties to create hydrophobic surfaces and reducing the friction coefficient. The latter is of particular interest in the field of tribology because friction directly effects wear mechanisms and a reduction in the coefficient of friction leads to an increase in service life. Tribological tests were carried out in another scientific work to investigate the influence of laser-generated structures on friction behavior (Chapter 2.2). LIPSS nanostructures and grid-like microstructures were tested using a rotation tribometer to determine the friction force. The results showed a reduction of the coefficient of friction by 35% for one of the three laser structures tested. Nevertheless, subsequently taken SEM images showed wear marks on all tested structures after the test duration of 10 seconds. Further investigations are necessary to determine the durability under tribological loads in more detail, especially in combination with lubricants. Such results could also be used to estimate the mechanical erosion resistance of laser-structured surfaces, an essential property in wind power applications.

In further research, it was investigated whether laser structuring could influence the wetting properties of metallic surfaces in the direction of superhydrophobicity and simultaneously make them icephobic. Interestingly, laser-structured metallic surfaces are hydrophilic after processing, i.e., they have a high surface energy, and water wets the surface very well. Subsequent storage in air changes the wetting properties from hydrophilic to hydrophobic, with the duration and final quality depending on various factors. In the course of another scientific article (chapter 2.3), the transformation time of laser-structured stainless steel samples was examined while they were stored in ambient air. A correlation was derived between the structure type and the wetting transformation time. It could be shown that

structures manufactured with lower energy input underwent a transformation shortened by up to 100 days. Deeper structures with a higher energy input showed slower conversion but significantly more hydrophobicity after reaching a saturated contact angle plateau. After the transformation was completed for all structure types (~ 200 days), the surfaces' deicing properties were examined. For this purpose, a test stand was developed and set up to quantify ice adhesion using a push-test. The results showed a direct correlation between surface roughness, which resulted from the laser processing parameters, and the measured ice adhesion. LIPSS nanostructures achieved the lowest ice adhesion, which was approximately the same as that of the unstructured reference sample. Nevertheless, there was a significant increase in the contact angle of approx. 35% and thus an improved overall performance of the LIPSS surface in terms of wetting and de-icing in line with the target values.

Extensive investigations into the causes of the described transformation of the wetting behavior from hydrophilic to hydrophobic led to laser-induced chemical processes. The lasers' energy initiates oxidation increasing the surface energy and polarity [61]. Water molecules from the ambient air can dock on the oxide layer and form hydroxyls, which can then adsorb another passivating water layer through hydrogen bonding [56]. However, hydroxyls on the oxide layer can also chemisorb organic molecules, such as those present in the ambient air as acetic ($C_2H_4O_2$) or formic acid (CH_2O_2). Furthermore, for example, methanol (CH_4O) can be chemisorbed on hydroxylated iron oxide (FeO_3) [66]. Since some of these organic molecules, in which a distinction can be made between polar and non-polar carbon compounds, can lead to hydrophobization by reducing the surface energy, the process of chemisorption of non-polar carbon components, in particular, is of great importance for surface modification. One way to accelerate this "natural" conversion process in ambient air is vacuum treatment, in which the laser-structured samples are stored in a high vacuum for a certain period. In the vacuum chamber, by evacuating most of the atmosphere and thus the water molecules, passivation of the active, hydroxylated iron oxides is prevented, and the chemisorption of organic molecules such as hydrocarbons is facilitated. These hydrocarbons may come from contamination in the vacuum chamber or organic lubricants used in vacuum pumps. When chemisorbed on the sample surface, surface polarity is reduced, which leads to hydrophobization. Another method to speed up the wetting transformation time was developed by Ngo et al. and involves thermal heating of steel samples directly after laser structuring [67]. After four hours of annealing at 100 °C, the samples showed superhydrophobic wetting behavior. The authors attribute the behavior to a decomposition of CO_2 on carbon with an active magnetite Fe_3O_4 activated by the laser.

Based on this literature, an alternative method for accelerating and amplifying the chemical surface transformation initiated by laser structuring using various hydrocarbons was developed and compared with the vacuum method (Chapter 2.4). The laser-structured samples were brought into contact with different hydrocarbons, on the one hand with a saturated gas atmosphere and on the other hand by immersion in the respective liquid. The best results were achieved by Eurosuper 95 gasoline immersion. This reduced the wetting transformation time to approximately one hour and the samples showed superhydrophobic wettability. When ice adhesion was measured in a laboratory experiment via push-test, a significant structure dependence was shown. Surface structures with lower roughness resulted in lower ice adhesion. By combining laser nanostructuring (LIPSS) and storage in gasoline, the ice adhesion could be reduced by about 50%.

Since the primary research objective was achieved by significantly reducing ice adhesion, another experiment should test the performance and durability of the modified surfaces under more realistic conditions. For this purpose, different structures were applied to thin, flexible steel foils and subjected to hydrocarbon (gasoline) and vacuum treatment. The flexibility of the steel foils allowed them to be attached to wing sections (NACA 0012 profile), which were then tested under calibrated icing conditions in a climatic wind tunnel. The laser-structured samples treated with gasoline showed significantly improved initial water runback behavior compared to the untreated stainless steel foils chosen as reference. As the icing progressed over time, ice beads formed on the reference surface in the area of the leading edge - there was a significant delay of approx. 50 seconds on the petrol-treated, laser-structured surfaces.

In addition to the performance experiments, a field test was carried out to evaluate the erosion resistance of laser-structured stainless steel surfaces under real operating conditions. This is important because superhydrophobic and icephobic surfaces in an industrial application are usually subjected to the weather and thus to erosion and there were no long-term studies available at the time of this work. The experimental setup consisted of a small-scale wind turbine, which was installed on an exposed

mountain ridge in the Austrian Alps at 1.600 meters above sea level. Flexible stainless steel foils, which were previously laser-structured, were attached to the leading edges of the rotor blades. The experiment lasted an entire winter and, in addition to detailed weather data for the site, also provided interesting results on the erosion resistance of the tested structures. It was shown that all four structural types examined survived the long exposure, with minor wear. The LIPSS nanostructures showed grooves and slight flattening in the most stressed area of the leading edge. The examined microstructures also experienced a slight smoothing and, thus, a reduction in the surface-related roughness S_a of about 17% compared to the reference samples. To compare these values with real operating conditions, weather data and wear observations from Hasager et al. were used [68]. In their work, the rain erosion load and its effect on the service life of the critical areas of the rotor blade leading edge (a few meters from the blade tip in the direction of the hub) in the North Sea region were examined in more detail. It turned out that the lifespan depends largely on the amount of precipitation and the wind speeds prevailing simultaneously; The locations with heavy rain erosion drastically reduce the lifespan. A heavily affected location was Helgoland (DE), for example, with an annual rainfall of 800 – 1.000 mm and average wind speeds of approx. 7 m/s, which led to a rotor blade service life of 1.4 years. For comparison, the Pretul location chosen for our long-term study at 1.600 meters above sea level has an annual precipitation of 1.600-1.800 mm and an average wind speed of 6.6 m/s and was therefore exposed to similar erosion conditions. If erosion progresses linearly, the lifespan of the microstructures (grid and triangle) can be extrapolated to > 2 years, and that of the dimple structure to > 6 years. After this period, only the base substrate would remain, which could continue to fulfill the function of an erosion shield on the leading edge. Such a substrate could also take on the function of lightning protection [10, 69].

1.5 Scientific contribution

All experiments were performed using a Titanium:Sapphire femtosecond laser. In the course of this dissertation, various aspects of laser/material interaction and the resulting surface properties were investigated in more detail. The scientific findings can be summarized as follows:

Properties of LIPSS nanostructures with variation of the machining parameters and transition towards the ablation threshold:

- The ratio of HSFL to LSFL depends on the laser fluence and the number of applied laser pulses; low fluence leads to a higher proportion of HSFL for the same number of pulses.
- The spatial frequencies of HSFL and LSFL are relatively independent of the fluence and the number of laser pulses applied and are in the range of $\lambda_{LSFL} \approx 655 \text{ nm}$ or $\lambda_{HSFL} \approx 300 \text{ nm}$, which corresponds to approximately 80% and 38% of the laser wavelength used.
- The transition from LIPSS to structures characterized by ablation, so-called grooves, takes place at a threshold fluence of 0.04 J/cm^2 and approx. 900 pulses.
- The transition from LIPSS to larger structures, the so-called cones, occurs at a threshold fluence of 0.28 J/cm^2 and approx. 600 pulses.

Modification of surface properties due to nano- and microstructuring:

- Laser-generated micro-grid structures led to a reduction in the coefficient of friction of 35%.
- The wetting transformation time from hydrophilic to hydrophobic caused by chemical processes on the laser-structured surface depends on the structure type or the accumulated fluence used for structuring.
- The wetting transformation time was lower for LIPSS nanostructures and longer for deep microstructures.
- Surface structures with increased roughness lead to a higher contact angle after the chemical transformation was completed.
- Ice adhesion correlates with the surface roughness of the structure – rougher structures lead to higher ice adhesion and vice versa.
- LIPSS nanostructures lead to a significant increase in the contact angle compared to the unstructured reference while maintaining the same ice adhesion.

Acceleration of the transition from hydrophilic to superhydrophobic after femtosecond laser processing and decreasing ice adhesion to the treated surfaces:

- The hydrophobic hydrocarbon layer on the structured surface could withstand several icing and de-icing cycles.
- Inserting laser-structured steel samples into liquid hydrocarbons significantly accelerates the wetting transformation time from hydrophilic to hydrophobic, for example in the case of the micro-lattice structure in Eurosuper gasoline from 100 days to 1 hour.
- Immersion of laser-structured steel samples in Eurosuper gasoline significantly reduces ice adhesion, for example, the LIPSS nanostructure from 800 kPa to 400 kPa.
- Vacuum treatment of laser-structured steel samples to reduce the wetting transformation time from hydrophilic to hydrophobic leads to a significant reduction in ice adhesion, for example, the LIPSS nanostructures from 800 kPa to 200 kPa.

Chemical analysis of the laser-processed and hydrocarbon/vacuum treated surfaces:

- Both gasoline and vacuum treatment lead to an increase in surface carbon content.
- The ice adhesion of laser-structured steel samples treated with gasoline or vacuum correlates with the proportion of non-polar carbon components. For the same structure type, the higher the concentration of non-polar components (C-C/C-H) on the surface, the lower the resulting ice adhesion.

Icing wind tunnel tests for performance evaluation under calibrated icing conditions:

- Icing wind tunnel test under glaze ice conditions, where laser-structured steel foils were attached to airfoil segments and treated with gasoline revealed, that:
 - Water droplets dissipated to the trailing edge much better than bare reference foils and
 - Caused a delay of 50 seconds in the growth of ice beads on the leading edge.

Durability tests of various laser-generated nano- and microstructures under realistic environmental conditions:

- Laser-generated nano- and microstructures withstood the erosion loads on a wind turbine under alpine operating conditions and exhibited only minor erosion wear over six winter months.

1.6 References

- [1] Worldwide electricity production by source. URL: <https://ourworldindata.org/energy>, accessed on 27.9.2023
- [2] IRENA (2019), Future of wind: Deployment, investment, technology, grid integration and socioeconomic aspects (A global Energy Transformation paper), International Renewable Energy Agency, Abu Dhabi.
- [3] EEA Report No 10/2022 (2022), Trends and projections in Europe 2022, ISBN 978-92-9480-505-8
- [4] Bundesgesetz über den Ausbau von Energie aus erneuerbaren Quellen (Erneuerbaren-Ausbau-Gesetz – EAG), BGBl. I Nr. 233/2022
- [5] Cattin, R. (2008), Alpine Test Site Guetsch – Handbuch und Fachtagung, Schlussbericht. Schweizerische Eidgenossenschaft
- [6] IEA Wind TCP, Task 19 (2018), Available Technologies for Wind Energy in Cold Climates, 2nd Edition
- [7] Hiu, H., Linyue, G., Yang, L. (2022), Wind Turbine Icing Physics and Anti-/De-Icing Technology, ISBN 978-0-12-824532-3
- [8] Malberg, H. (2006), Meteorologie und Klimatologie - Eine Einführung. Springer. ISBN: 3-540-42919-0.
- [9] ISO 12494 (2001), Atmospheric icing of structures.
- [10] Katsaprakakis, D. A., Papadakis, N., & Ntintakis, I. (2021). A Comprehensive Analysis of Wind Turbine Blade Damage. *Energies*, 14, 5974. doi: <https://doi.org/10.3390/en14185974>
- [11] Shu, L., Li, H., Hu, Q., Jiang, X., Qiu, G., McClure, G., & Yang, H. (2018). Study of ice accretion feature and power characteristics of wind turbines at natural icing environment. *Cold Regions Science and Technology*, 147, 45–54. doi: <https://doi.org/10.1016/j.coldregions.2018.01.006>
- [12] Liu, Y., & Hu, H. (2018). An experimental investigation on the unsteady heat transfer process over an ice accreting airfoil surface. *International Journal of Heat and Mass Transfer*, 122, 707–718. doi: <https://doi.org/10.1016/j.ijheatmasstransfer.2018.02.023>
- [13] Cober, S. G., Isaac, G. A., & Strapp, J. W. (November 2001). Characterizations of Aircraft Icing Environments that Include Supercooled Large Drops. *Journal of Applied Meteorology*, 40, 1984–2002. doi: [https://doi.org/10.1175/1520-0450\(2001\)040<1984:coaiet>2.0.co;2](https://doi.org/10.1175/1520-0450(2001)040<1984:coaiet>2.0.co;2)
- [14] Jeck, R., K. (2010), Models and Characteristics of Freezing Rain and Freezing Drizzle for Aircraft Icing Applications, U.S. Department of Transportation, FAA
- [15] Fasani, D., Cernuschi, F., & Colombo, L. P. (October 2023). Calorimetric determination of wet snow liquid water content: The effect of test conditions on the calorimeter constant and its impact on the measurement uncertainty. *Cold Regions Science and Technology*, 214, 103959. doi: <https://doi.org/10.1016/j.coldregions.2023.103959>
- [16] Seifert, H., Westerhellweg, A., & Kröning, J. (January 2003). Risk Analysis of Ice Throw from Wind Turbines. *Boreas*, 6.
- [17] Morgan, C., Bossanyi, E., & Seifert, M. H. (1998). Assessment of safety risks arising from wind turbine icing. BOREAS IV.
- [18] Ducan, T., LeBlanc, M., Morgan, C., Landberg, L. (2008), Understanding Icing Losses and Risk of Ice Throw at Operating Wind Farms, Winterwind
- [19] Prikhod'ko, A. A., Alekseenko, S. V., & Chmovzh, V. V. (March 2019). Experimental Investigation of the Influence of the Shape of Ice Outgrowths on the Aerodynamic Characteristics of the Wing. *Journal of Engineering Physics and Thermophysics*, 92, 486–492. doi: <https://doi.org/10.1007/s10891-019-01955-1>
- [20] Homola, M. C., Virk, M. S., Nicklasson, P. J., & Sundsbø, P. A. (June 2011). Performance losses due to ice accretion for a 5 MW wind turbine. *Wind Energy*, 15, 379–389. doi: <https://doi.org/10.1002/we.477>
- [21] Frohboese, P., & Anders, A. (July 2007). Effects of Icing on Wind Turbine Fatigue Loads. *Journal of Physics: Conference Series*, 75, 012061. doi: <https://doi.org/10.1088/1742-6596/75/1/012061>
- [22] Parent, O., & Ilinca, A. (January 2011). Anti-icing and de-icing techniques for wind turbines: Critical review. *Cold Regions Science and Technology*, 65, 88–96. doi: <https://doi.org/10.1016/j.coldregions.2010.01.005>
- [23] Bragg, M. B., Broeren, A. P., & Blumenthal, L. A. (July 2005). Iced-airfoil aerodynamics. *Progress in Aerospace Sciences*, 41, 323–362. doi: <https://doi.org/10.1016/j.paerosci.2005.07.001>

- [24] Barber, S., Wang, Y., Jafari, S., Chokani, N., & Abhari, R. S. (January 2011). The Impact of Ice Formation on Wind Turbine Performance and Aerodynamics. *Journal of Solar Energy Engineering*, 133. doi: <https://doi.org/10.1115/1.4003187>
- [25] Laakso, T., Baring-Gould, I., Durstewitz, M., Horbaty, R., Lacroix, A., Peltola, E., Wallenius, T. (September 2010). State-of-The-art of wind energy in cold climates. English, 152.
- [26] Shu, L., Li, H., Hu, Q., Jiang, X., Qiu, G., McClure, G., & Yang, H. (March 2018). Study of ice accretion feature and power characteristics of wind turbines at natural icing environment. *Cold Regions Science and Technology*, 147, 45–54. doi: <https://doi.org/10.1016/j.coldregions.2018.01.006>
- [27] Gao, L., Tao, T., Liu, Y., & Hu, H. (April 2021). A field study of ice accretion and its effects on the power production of utility-scale wind turbines. *Renewable Energy*, 167, 917–928. doi: <https://doi.org/10.1016/j.renene.2020.12.014>
- [28] Kjersem, H., A. (2019), Estimation of Production Losses due to Icing on Wind Turbines at Kvitfjell Wind Farm, Norwegian University of Life Sciences
- [29] Dierer, S., Oechslin, R., & Cattin, R. (September 2011). Wind turbines in icing conditions: performance and prediction. *Advances in Science and Research*, 6, 245–250. doi: <https://doi.org/10.5194/asr-6-245-2011>
- [30] Botta, G., Cavaliere, M., & Holttinen, H. (January 1998). Ice Accretion at Acqua Spruzza and Its Effects on Wind Turbine Operation and Loss of Energy Production. *Ice Accretion at Acqua Spruzza and its Effects on Wind Turbine Operation and Loss of Energy Production*, BOREAS IV.
- [31] Laakso, T., & Peltola, E. (January 2005). Review on blade heating technology and future prospects. BOREAS VII FMI Conference.
- [32] Battisti, L., Fedrizzi, R., Brighenti, A., & Laakso, T. (May 2006). Sea ice and icing risk for offshore wind turbines. 20–22.
- [33] Maissan, J. F., “Wind Power Development in Sub-Arctic Conditions with Severe Rime Icing”, TSYE Corporation - Circumpolar Climate Change Summit and Exposition, 2001.
- [34] Huang, X., Tepylo, N., Pommier-Budinger, V., Budinger, M., Bonaccorso, E., Villedieu, P., & Bennani, L. (February 2019). A survey of icephobic coatings and their potential use in a hybrid coating/active ice protection system for aerospace applications. *Progress in Aerospace Sciences*, 105, 74–97. doi: <https://doi.org/10.1016/j.paerosci.2019.01.002>
- [35] Gwak, Y., Park, J.-I., Kim, M., Kim, H. S., Kwon, M. J., Oh, S. J., Jin, E. (July 2015). Creating Anti-icing Surfaces via the Direct Immobilization of Antifreeze Proteins on Aluminum. *Scientific Reports*, 5. doi: <https://doi.org/10.1038/srep12019>
- [36] Menini, R., & Farzaneh, M. (January 2011). Advanced Icephobic Coatings. *Journal of Adhesion Science and Technology*, 25, 971–992. doi: <https://doi.org/10.1163/016942410x533372>
- [37] Momen, G., Jafari, R., & Farzaneh, M. (September 2015). Ice repellency behaviour of superhydrophobic surfaces: Effects of atmospheric icing conditions and surface roughness. *Applied Surface Science*, 349, 211–218. doi: <https://doi.org/10.1016/j.apsusc.2015.04.180>
- [38] Work, A.; Lian, Y. (April 2018). A critical review of the measurement of ice adhesion to solid substrates. *Progress in Aerospace Sciences*, 98, 1-26. doi: <https://doi.org/10.1016/j.paerosci.2018.03.001>
- [39] Irajizad, P., Nazifi, S., & Ghasemi, H. (July 2019). Icephobic surfaces: Definition and figures of merit. *Advances in Colloid and Interface Science*, 269, 203–218. doi: <https://doi.org/10.1016/j.cis.2019.04.005>
- [40] Beeram, P.S.R. (2017). Characterization of ice adhesion strength over different surfaces pertinent to aircraft anti-/de-icing. Graduate theses and dissertations. 16073. <https://lib.dr.iastate.edu/etd/16073>
- [41] Meuler, A. J., Smith, J. D., Varanasi, K. K., Mabry, J. M., McKinley, G. H., & Cohen, R. E. (November 2010). Relationships between Water Wettability and Ice Adhesion. *ACS Applied Materials & Interfaces*, 2, 3100–3110. doi: <https://doi.org/10.1021/am1006035>
- [42] Milne, A. J., & Amirfazli, A. (January 2012). The Cassie equation: How it is meant to be used. *Advances in Colloid and Interface Science*, 170, 48–55. doi: <https://doi.org/10.1016/j.cis.2011.12.001>

- [43] Yao, C.-W., Alvarado, J. L., Marsh, C. P., Jones, B. G., & Collins, M. K. (January 2014). Wetting behavior on hybrid surfaces with hydrophobic and hydrophilic properties. *Applied Surface Science*, 290, 59–65. doi: <https://doi.org/10.1016/j.apsusc.2013.10.188>
- [44] Stankevicius, E., Balciunas, E., Malinauskas, M., Raciukaitis, G., Baltriukiene, D., & Bukelskiene, V. (June 2012). Holographic lithography for biomedical applications. In T. Graf, J. I. Mackenzie, H. Jelínková, & J. Powell (Hrsg.), *SPIE Proceedings*. SPIE. doi: <https://doi.org/10.1117/12.922793>
- [45] Kim, M.-K., Yao, W., & Cho, Y.-R. (February 2022). Fabrication of superhydrophobic surface with hierarchical structure by thermal imprinting and spraying. *Colloids and Surfaces A: Physicochemical and Engineering Aspects*, 634, 127973. doi: <https://doi.org/10.1016/j.colsurfa.2021.127973>
- [46] Guo, Z., Fang, J., Wang, L., & Liu, W. (June 2007). Fabrication of superhydrophobic copper by wet chemical reaction. *Thin Solid Films*, 515, 7190–7194. doi: <https://doi.org/10.1016/j.tsf.2007.02.100>
- [47] Zhu, B., Ou, R., Liu, J., Yang, Y., Chen, S., Wei, G., & Zhang, Z. (February 2022). Fabrication of superhydrophobic surfaces with hierarchical structure and their corrosion resistance and self-cleaning properties. *Surfaces and Interfaces*, 28, 101608. doi: <https://doi.org/10.1016/j.surfin.2021.101608>
- [48] Vercillo, V., Tonnichia, S., Romano, J.-M., García-Girón, A., Aguilar-Morales, A. I., Alamri, S., Bonaccorso, E. (February 2020). Design Rules for Laser-Treated Icephobic Metallic Surfaces for Aeronautic Applications. *Advanced Functional Materials*, 30, 1910268. doi: <https://doi.org/10.1002/adfm.201910268>
- [49] Martínez-Calderon, M., Rodríguez, A., Dias-Ponte, A., Morant-Miñana, M. C., Gómez-Aranzadi, M., & Olaizola, S. M. (June 2016). Femtosecond laser fabrication of highly hydrophobic stainless steel surface with hierarchical structures fabricated by combining ordered microstructures and LIPSS. *Applied Surface Science*, 374, 81–89. doi: <https://doi.org/10.1016/j.apsusc.2015.09.261>
- [50] Han, W., Kim, J., & Kim, B. (January 2018). Effects of contamination and erosion at the leading edge of blade tip airfoils on the annual energy production of wind turbines. *Renewable Energy*, 115, 817–823. doi: <https://doi.org/10.1016/j.renene.2017.09.002>
- [51] Sareen, A., Sapre, C. A., & Selig, M. S. (July 2013). Effects of leading edge erosion on wind turbine blade performance. *Wind Energy*, 17, 1531–1542. doi: <https://doi.org/10.1002/we.1649>
- [52] Zeng, D., Li, Y., Huan, D., Liu, H., Luo, H., Cui, Y., Wang, J. (November 2021). Robust epoxy-modified superhydrophobic coating for aircraft anti-icing systems. *Colloids and Surfaces A: Physicochemical and Engineering Aspects*, 628, 127377. doi: <https://doi.org/10.1016/j.colsurfa.2021.127377>
- [53] Wu, X., Silberschmidt, V. V., Hu, Z.-T., & Chen, Z. (January 2019). When superhydrophobic coatings are icephobic: Role of surface topology. *Surface and Coatings Technology*, 358, 207–214. doi: <https://doi.org/10.1016/j.surfcoat.2018.11.039>
- [54] Jung, Y. S., & Baeder, J. (January 2020). Simulations for Effect of Surface Roughness on Wind Turbine Aerodynamic Performance. *Journal of Physics: Conference Series*, 1452, 012055. doi: <https://doi.org/10.1088/1742-6596/1452/1/012055>
- [55] Fortin, G., Ilinca, A., Laforte, J.-L., & Brandi, V. (January 2004). New Roughness Computation Method and Geometric Accretion Model for Airfoil Icing. *Journal of Aircraft*, 41, 119–127. doi: <https://doi.org/10.2514/1.173>
- [56] Jagdheesh, R., Diaz, M., Marimuthu, S., & Ocana, J. L. (2017). Robust fabrication of μ -patterns with tunable and durable wetting properties: hydrophilic to ultrahydrophobic via a vacuum process. *Journal of Materials Chemistry A*, 5, 7125–7136. doi: <https://doi.org/10.1039/c7ta01385j>
- [57] Sojoudi, H.; McKinley, G.H.; Gleason, K.K. (October 2014). Linker-free grafting of fluorinated polymeric cross-linked network bilayers for durable reduction of ice adhesion. *Materials Horizons*, 2, 91. doi: <https://doi.org/10.1039/c4mh00162a>
- [58] Zhu, L.; Xue, J.; Wang, Y.; Chen, Q.; Ding, J.; Wang, Q. (April 2013). Ice-phobic coatings based on silicon-oil-infused polydimethylsiloxane. *ACS Applied Materials & Interfaces*, 5, 4053–4062. doi: <https://doi.org/10.1021/am400704z>

- [59] Kim, P.; Wong, T-S.; Alvarenga, J.; Kreder, M.J.; Adorno-Martinez, W.E.; Aizenberg, J. (June, 2012). Liquid-infused nanostructured surfaces with extreme anti-ice and anti-frost performance. *ACS Nano*, 6, 8, 6569-6577. doi: <https://doi.org/10.1021/nn302310q>
- [60] Bonse, J., Hohm, S., Kirner, S. V., Rosenfeld, A., & Kruger, J. (May 2017). Laser-Induced Periodic Surface Structures— A Scientific Evergreen. *IEEE Journal of Selected Topics in Quantum Electronics*, 23. doi: <https://doi.org/10.1109/jstqe.2016.2614183>
- [61] Hauschwitz, P., Jagdheesh, R., Rostohar, D., Brajer, J., Kopeček, J., Jiříček, P., Mocek, T. (March 2020). Hydrophilic to ultrahydrophobic transition of Al 7075 by affordable ns fiber laser and vacuum processing. *Applied Surface Science*, 505, 144523. doi: <https://doi.org/10.1016/j.apsusc.2019.144523>
- [62] ThermoFischer XPS Table of Elements, URL: <https://www.thermofisher.com/at/en/home/materials-science/learning-center/periodic-table.html>, accessed on 28.9.2023
- [63] XPS Reference Pages, <http://www.xpsfitting.com/>, accessed on 28.9.2023
- [64] Puffing, R. F., Peciar, M., & Hassler, W. (January 2013). Instrumentation of an icing wind tunnel based on SAE standards. *Scientific Proceedings Faculty of Mechanical Engineering STU in Bratislava*, 21. doi: <https://doi.org/10.2478/stu-2013-0007>
- [65] Otto, A. (August 1968). Excitation of nonradiative surface plasma waves in silver by the method of frustrated total reflection. *Zeitschrift für Physik A Hadrons and Nuclei*, 216, 398–410. doi: <https://doi.org/10.1007/bf01391532>
- [66] Micale, F. J., Kiernan, D., & Zettlemoyer, A. C. (June 1985). Characterization of the surface properties of iron oxides. *Journal of Colloid and Interface Science*, 105, 570–576. doi: [https://doi.org/10.1016/0021-9797\(85\)90332-7](https://doi.org/10.1016/0021-9797(85)90332-7)
- [67] Ngo, C.-V., & Chun, D.-M. (July 2017). Fast wettability transition from hydrophilic to superhydrophobic laser-textured stainless steel surfaces under low-temperature annealing. *Applied Surface Science*, 409, 232–240. doi: <https://doi.org/10.1016/j.apsusc.2017.03.038>
- [68] Hasager, C. B., Vejen, F., Skrzyński, W. R., & Tilg, A.-M. (April 2021). Rain Erosion Load and Its Effect on Leading-Edge Lifetime and Potential of Erosion-Safe Mode at Wind Turbines in the North Sea and Baltic Sea. *Energies*, 14, 1959. doi: <https://doi.org/10.3390/en14071959>
- [69] Lewke, B., Kindersberger, J., Krämer, S., & Hernández, Y. (June 2007). *Conductive Surface Layer on Wind Turbine Blade as Lightning Protection System*. Los Angeles, 2007

2 Publications

2.1. Experimental Study of Spatial Frequency Transition of Laser Induced Periodic Surface Structures

Presented at: ITNT 2020, Samara, Russia

Published by: IOP Publishing (2021)

Journal: Journal of Physics: Conference Series

DOI: <http://dx.doi.org/10.1088/1742-6596/1745/1/012017>

R. Fuerbacher¹, G. Liedl¹, S. Murzin^{1 2}

¹Vienna University of Technology, Institute of Production Engineering and Photonic Technologies, Vienna, Austria

²Samara National Research University, Moskovskoe Shosse 34A, Samara, Russia, 443086

Abstract. This study shows the influence of laser fluence and pulse number on the spatial frequency distribution of laser induced periodic surface structures (LIPSS) on a stainless steel surface. Also the transition of LIPSS to larger self organized, periodic, cone-like structures has been investigated. The experiments were carried out using a Ti:Sapphire femtosecond laser system with 800 nm centre wavelength, a pulse duration of 30 fs and a repetition rate of 1 kHz. Experiments have been carried out on flat, cold-rolled stainless steel surfaces (1.4301) by variation of the laser output power and feed rate. It could be shown, that the transition of low spatial frequency LIPSS (LSFL) to high spatial frequency LIPSS (HSFL) is a continuous process, strongly depending on the laser single pulse fluence and the pulse number. At higher accumulated fluences the transition of LIPSS to larger self organized structures could be observed. As a result, hierarchical structures were created with micrometer-sized cones at the bottom and nanometer-sized LIPSS on top. By further increasing the accumulated fluence, the grooves between the micro structures are widened until the ablation threshold of the alloy is reached. These hierarchical structures could be of considerable value in improving wetting properties of technical surfaces.

1. Introduction

Laser induced periodic surface structures (LIPSS) are self organized nano structures that occur, when laser radiation interacts with the surface of a material near its ablation threshold for a single laser pulse [1]. They were first observed in the 1960ies after illumination of semiconductor surfaces by a pulsed ruby laser and high peak powers [2]. Since then, the initial formation mechanisms of LIPSS have been investigated using a variety of laser sources and substrate materials, but they are still subject of international research [3]. They have been applied on metals [4], semiconductors [2] as well as on dielectrics [5] and can be categorized according to their spatial period Λ or period ratio Λ/λ , with λ being the incident laser wavelength. There have been reports of various period ratios, ranging from so called supra wavelength sized LIPSS $\Lambda/\lambda > 1$ which were observed on fused silica [6] over low spatial frequency $1 > \Lambda/\lambda > 0.5$ to high spatial frequency LIPSS $\Lambda/\lambda < 0.5$ [3]. The most commonly used model associates the formation of LIPSS with a coupling mechanism between the incident laser light and the surface plasmons, which results in the excitation of so called surface plasmon polaritons (SPP) [7]. Surface plasmons can be described as oscillations of free electrons (or as electron plasma). Once excited, SPPs are evanescent, longitudinal TM-waves that travel in the interface of a metal and a dielectric [7]. But because SPPs are evanescent waves, according to the model, they cannot be excited directly by a laser beam with an incident angle of $\alpha = 0^\circ$, since the momentum of the incident light wave is orientated perpendicular to the surface plane [8]. Nevertheless and despite of this theoretical limitations, it could be shown experimentally, that LIPSS can be generated under this condition [9].

Theoretically, the excitation of SPPs is possible, if either the phase velocities of the incident light and the propagating plasmon polariton waves are matched [10] or by coupling via the surface roughness [11]. Since the dielectric prism configuration is not used in most setups for generation of LIPSS, the coupling via the surface roughness is the current theory to explain their formation. Gurevich et al. investigated the influence of initial surface conditions (pre-patterned metal samples) on the resulting LIPSS period [8]. According to the plasmonic theory, after the first laser pulse hits the surface and thereby initiates the formation of LIPSS, further applied laser pulses should decrease the LIPSS period. They were not able to verify the plasmonic theory experimentally.

In the paper presented here, we describe experiments to investigate LIPSS formation and ablation thresholds for stainless steel and a wide range of applied fluences and pulse numbers. We observed not only the formation of LIPSS with different spatial periods, but also the transition of low spatial frequency LIPSS (LSFL) to high spatial frequency LIPSS (HSFL) by splitting until a certain threshold is reached and the ablation regime is initiated. By further increasing the applied fluence, larger self-organized structures in the micro-meter-regime appear, initially with LIPSS on top, thereby forming hierarchical structures. The size and spatial separation of those larger cone structures is strongly influenced by the applied accumulated fluence. Once in the ablation regime, a higher pulse number leads to increased surface roughness due to more internal reflections and causes the micro structures to grow [12].

2. Experimental Setup

In this study we used cold rolled stainless steel samples (1.4301) with a thickness of 0.05 mm without any post production surface modification. Measurements showed an arithmetical mean height of $S_a = 141.3$ nm and a maximum height of $S_z = 2.29$ μm (acc. to ISO 25178). The surface properties were obtained by an Alicona Infinite Focus G5 measurement system. A Ti:Sapphire (Ti:Al₂O₃) solid state laser (Femtopower Compact Pro) was used to initiate LIPSS generation. The system operates at a repetition rate of 1 kHz, emitting 30 fs pulses at a central wavelength of $\lambda = 800$ nm and a bandwidth of ± 50 nm. The laser delivers radiation with an average output power of 800 mW which leads to a single pulse energy of 0.8 mJ. Due to its internal setup, the output radiation is linearly polarized. To adjust the laser fluence on the specimens' surface, a variable attenuator was used. Leaving the attenuator, the laser beam is then focused on the specimen by an off-axis parabolic mirror with a protected silver coating. To exclude the influence of astigmatism effects caused by the convex focusing mirror, the workpiece was not moved in direction of the incident laser beam during the experiments (angle of incidence = 0°). The experiments have been conducted in a controlled environment at 21 °C in air. To study the effects of fluence and the number of pulses on the formation of LIPSS, the workpiece was mounted on a motor driven linear stage and moved with various feed rates along the horizontal axis. Since the maximum feed rate was limited to 8 mm/s, the beam diameter was adjusted to $d = 295$ μm to achieve the desired fluence range on the specimen. After inducing nano structures on the surfaces, the samples were cleaned with demineralized water in an ultrasonic bath and examined by a scanning electron microscope (Jeol JCM-5000, FEI Quanta 250 FEG). To investigate the initiation of the LIPSS generation, we concentrated the analysis on those areas, where the Gaussian intensity distribution of the laser beam has its maximum. The SEM pictures were then analysed using Fast Fourier Transformation (Matlab) perpendicular to the LIPSS orientation. By using the Matlab Signal Analyser Tool, the FFTs were further investigated by searching for peaks in the frequency spectrum. Those peaks can be interpreted as the favorable spatial LIPSS periods and the amplitude gives an indication on their characteristics. To investigate the transition of LSFL to HSFL the ratio of the amplitude peak values is of interest. A raising ratio indicates that the HSFL are more favorable, which was also validated visually on the SEM images. The applied fluence was varied from $\phi = 0.02$ J/cm² to 0.90 J/cm², the number of pulses from $n = 37$ to $n = 1030$. For analysis of the formed grooves and cone structures at higher pulse energies, the area fraction of the grooves and the average base diameter of the cones have been evaluated. This was done by examination of 50 μm x 50 μm SEM images of the relevant surface areas using ImageJ Software.

3. Results

According to the plasmonic theory, the spatial period of the laser induced surface structures depends on the wavelength λ of the applied laser beam and the material properties of the interface [13]:

$$\Lambda_{\text{LIPSS}} = \frac{\lambda}{\eta \pm \sin \Theta} \quad (1)$$

where Θ is the lasers angle of incidence and η is the real part of the effective index of the surface plasmon mode. For an air/metal interface, η is typically about 1 [13]. This implicates that only one spatial period $\Lambda \approx \lambda$ will be induced by the laser source. Ref. [3] describes, that due to the increasing structure depth and other effects like the multi-pulse feedback phenomena, equation (1) is only valid for a small number of pulses. Our experimental results show a LSFL period which varies around $\Lambda_{\text{LSFL}} = 655$ nm for a wide range of pulse numbers $37 \leq n \leq 1030$, which is significantly lower than the center laser wavelength $\lambda = 800$ nm. The LIPSS orientation on our steel samples was found to be perpendicular to the polarization direction of our linearly polarized laser source, which is in agreement with observations of other authors for different metals [3], [12], [14]. We could observe the initialization of LIPSS formation with a spatial period of 650 nm at a single pulse fluence of $\phi = 0.04$ J/cm² and $n = 37$ pulses respectively (figure 1). Experiments were also conducted with a lower fluence of $\phi = 0.02$ J/cm², which turned out to be below the LIPSS formation threshold of steel 1.4301.

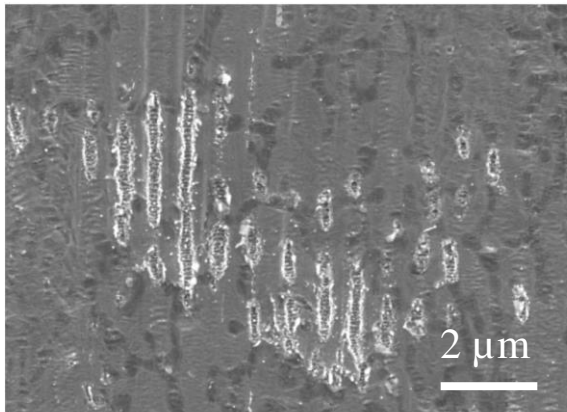


Figure 1. Initialization phase of LIPSS formation: $\phi = 0.04$ J/cm², $n = 37$.

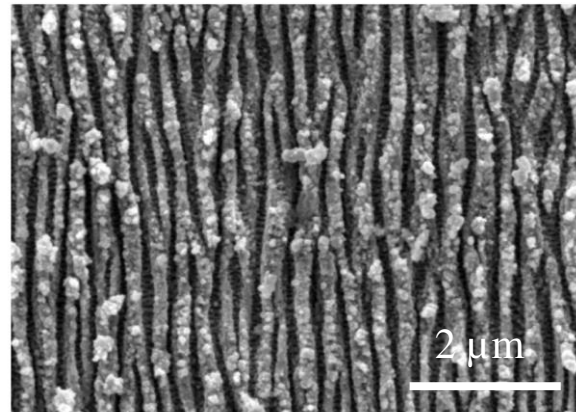


Figure 2. Splitting of LSFL into HSFL: $\phi = 0.04$ J/cm², $n = 462$.

An increased pulse number of $n = 178$ while keeping the fluence level constant at $\phi = 0.04$ J/cm² resulted in a larger structured area, showing only LSFL. By further increasing the number of applied pulses, splitting of LSFL occurs (Figure 2), which leads to a simultaneous formation of HSFL with a spatial period of $\Lambda/\lambda < 0.5$. This splitting process and its dependency on fluence and pulse number has already been described by multiple authors [15], [16]. The ratio between LSFL and HSFL can be adjusted by varying the number of pulses (Figure 3).

The maximum HSFL/LSFL amplitude ratio of 78% is reached at $\phi = 0.04$ J/cm² and $n = 462$ pulses. By further increasing the applied pulse number, the ratio decreases below 60%. At a higher fluence level of $\phi = 0.10$ J/cm² the splitting process is not as distinct, but the dependency on the pulse number is evident, reaching a maximum of 55 % at $n = 178$ pulses. Figure 3 shows that for a fluence of $\phi = 0.28$ J/cm² and low pulse numbers, the HSFL/LSFL ratio drops below 15 %, showing the start of the LIPSS/cone transition for $n > 321$. Under even higher fluences and pulse numbers $n < 321$, HSFL will not form at all, leaving only LSFL on the sample. Looking at the influence of the pulse number on the spatial LIPSS periods, for lower fluences ($\phi = 0.04$ to 0.28 J/cm²) the results show little fluctuations around the mean value of $\Lambda_{\text{LSFL}} = 655$ nm with a tendency to higher spatial periods for higher pulse numbers (Figure 6). This finding does not support the theory of grating assisted surface plasmon coupling, for which the LIPSS period should decrease for higher pulse numbers [3], [17].

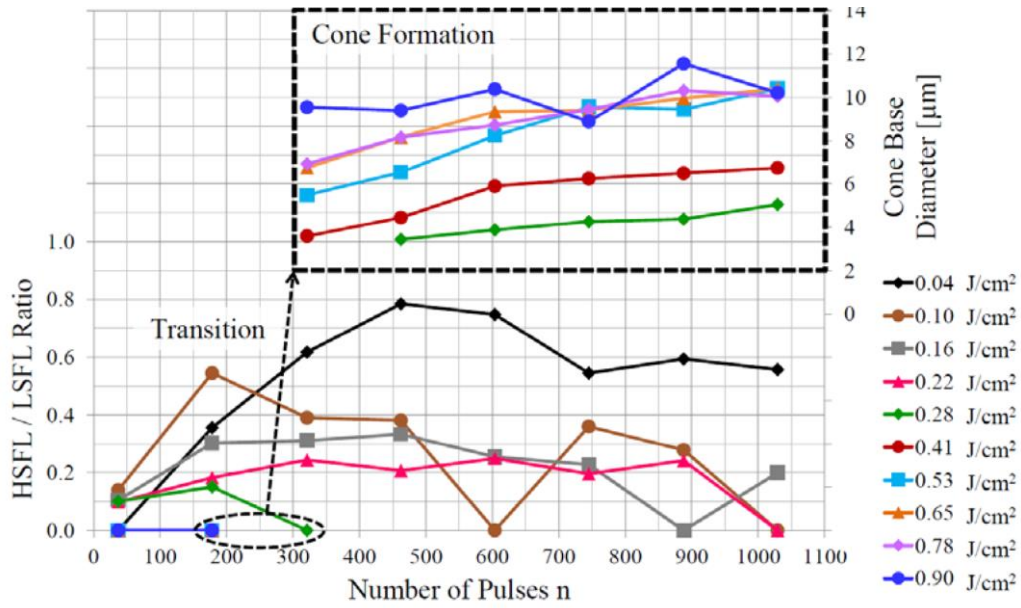


Figure 3. Top: Transition from LIPSS to cone structures; Bottom: HSFL/LSFL ratio dependence on the laser pulse fluence and the pulse number.

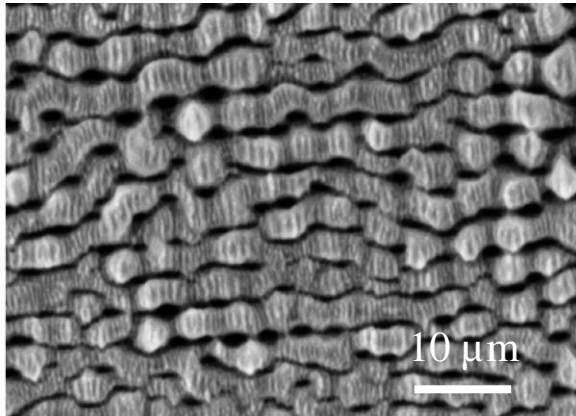


Figure 4. Grooves are formed: $\phi = 0.78 \text{ J/cm}^2$, $n=178$.

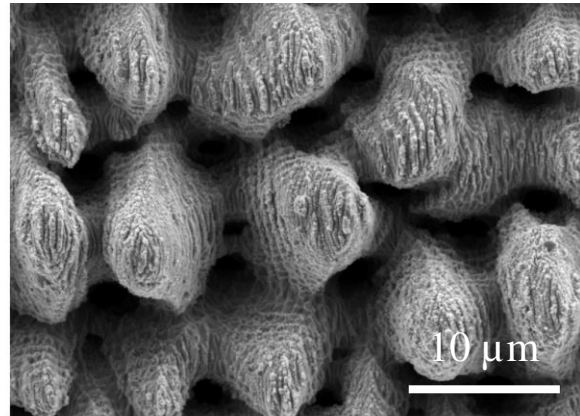


Figure 5. Hierarchical Structures: Cones with LIPSS on top: $\phi = 0.53 \text{ J/cm}^2$, $n = 321$.

The results shown in Figure 6, do not indicate any significant deviation from the mean HSFL period of $\Lambda_{\text{HSFL}} = 300 \text{ nm}$ ($\sigma = 21 \text{ nm}$) over a wide range of pulse numbers, but for higher pulse numbers the peaks in the FFT spectra are not as concise. Besides the formation of LSFL and HSFL the SEM images reveal the initialization and constant growth of so called grooves [18], which are ablated areas in between the LIPSS, orientated parallel to the polarization of the laser light (figure 4). Their growth is directly linked to the applied fluence and pulse number and results in the formation of cones (Figure 7). Our experimental results show, that at fluences above $\varphi = 0.28 \text{ J/cm}^2$ and pulse numbers $n > 178$, the formation of cones is initiated (Figure 3). As the transition from grooves to cones continues, LIPSS are still visible. By further increasing the fluence and pulse number, the LIPSS fade and the frequency amplitudes in the FFT spectrum are attenuated until they cannot be separated from noise. The average grain size or base diameter of the cones is not only related to the single pulse fluence or the pulse number, but proportional to their product - the accumulated fluence (Figure 7). It can be seen, that the correlation is not linear and the grain size saturates at about $11 \mu\text{m}$ for accumulated fluences above $\varphi_{\text{Acc}} = 600 \text{ J/cm}^2$. The formation or self organization of the observed structures could be a consequence of higher ablation rates at grain boundaries of the laser treated 1.4301 alloy [19]. At a critical accumulated fluence of $\varphi_{\text{Acc,crit}} \approx 1400 \text{ J/cm}^2$ ablation is dominant and erases all surface structures leaving only a clean cut in the metal sheet. It is possible to continue investigations using diffractive optical elements [20, 21].

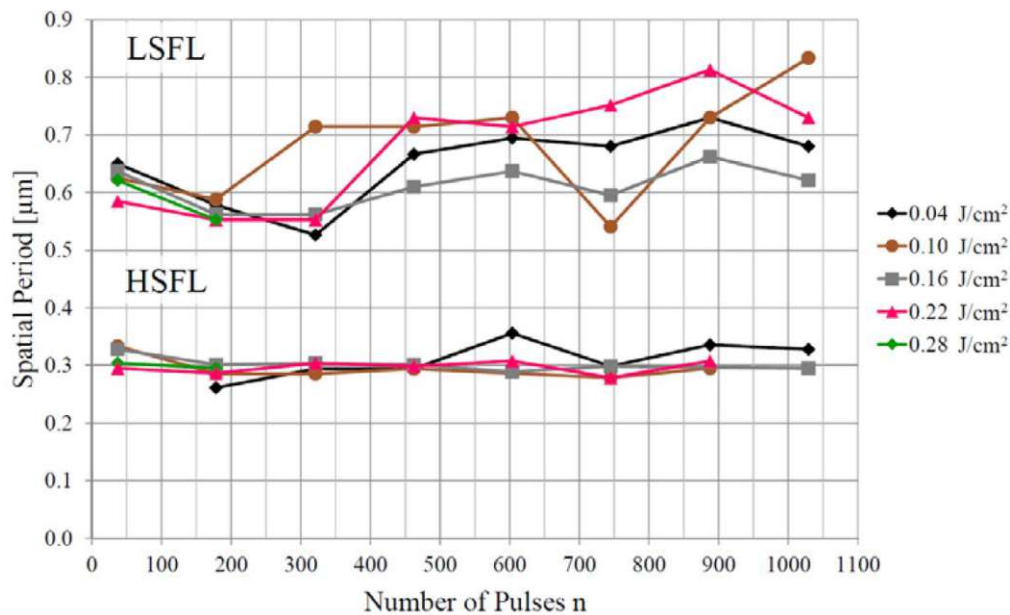


Figure 6. Spatial LIPSS period over a variety of laser fluences and pulse numbers.

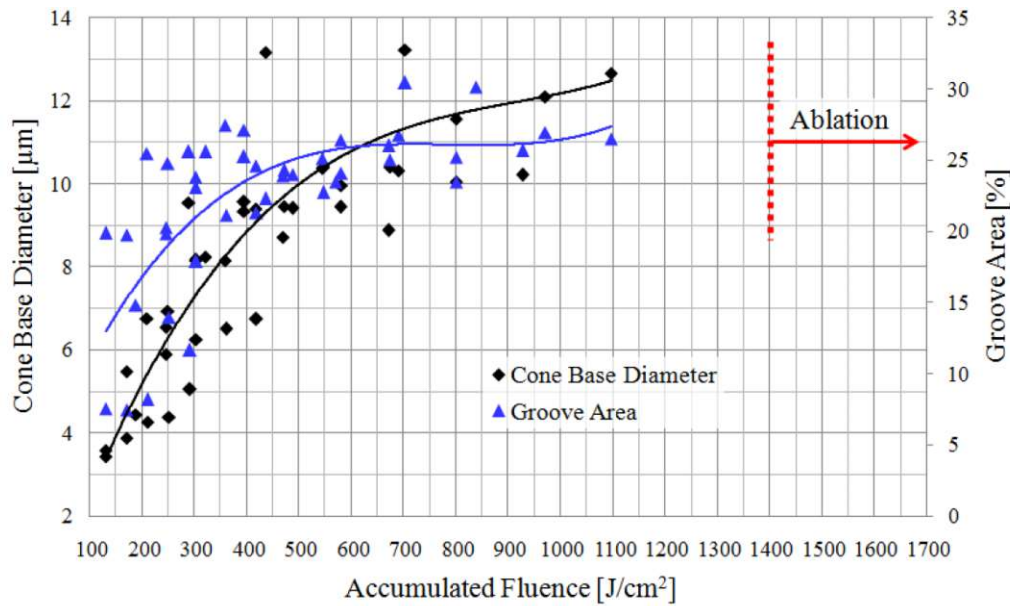


Figure 7. Correlation between groove area, cone size and the accumulated laser fluence.

4. Conclusions

In this study, we have experimentally investigated the processes, which lead to the formation of LSFL, HSFL, grooves and cone structures and found that continuous transitions between the observed structures occur and no abrupt changes could be detected. Nevertheless we were able to determine certain threshold levels for fluences and pulse numbers, at which the transitions are initiated (Table 1).

Table 1. Threshold levels for structure transitions on stainless steel 1.4301

Transition	Fluence threshold ϕ [J/cm^2]	Pulse number threshold n
Initialization of LIPSS formation	0.04	37
HSFL formation	0.04	178
Peak HSFL/LSFL ratio	0.04	462
Formation of small grooves	0.04	888
Ablation leads to cone formation	0.28	604
Ablation leads to cut	0.94	1500

The analysis of the obtained data shows that low and high spatial frequency LIPSS can be induced in parallel by a splitting process. The LSFL/HSFL ratio is influenced by the laser parameters and can thereby be tuned in a certain range. At low fluence levels, only small areas of the specimens' surface are covered by LIPSS, which is caused by the Gaussian intensity distribution of the used laser beam. The application of higher fluences will increase the area covered by LIPSS, but at the same time the HSFL/LSFL ratio declines. Considering this effect, the structuring of large areas with HSFL will result in long processing times, unless it would be compensated for by modifying the laser intensity distribution from Gaussian to a top head.

A spatial frequency inversion of LIPSS could not be observed in this work. Further investigations might show a certain parameter range, where LSFL splitting occurs at a high efficiency and only HSFL are formed. Considering the growth of grooves and cones, the structure depth could be a suitable indicator to study the ablation process in more detail. Also the grain boundaries of the material should be taken into account. The topology of the induced structures could be of great use to improve the wetting properties of technical surfaces. Because of their high surface to area ratio, the rough and deep cone-shaped structures show similarities to Lotus leaves and are therefore likely to cause hydrophobic behaviour. The continuation of studies with the use of diffractive optical elements is promising.

5. Acknowledgment

The authors would like to thank M. Nirtl for providing access to the necessary surface metrology equipment. We further acknowledge the University Service Centre for Transmission Electron Microscopy (USTEM) at TU Wien for their support on scanning electron microscopy. The authors are **grateful for the support of the project by the Climate and Energy Fond with FFG Project No. 871733.**

6. References

- [1] Nürnberg P, Reinhardt H, Kim H C, Yang F, Peppler K, Janek J and Hampp N 2015 J. Appl. Phys. 118(13) 134306 DOI: 10.1063/1.4932215.
- [2] Birnbaum M 1965 J. Appl. Phys. 36(11) 3688-3689 DOI: 10.1063/1.1703071.
- [3] Bonse J, Höhm S, Kirner S V, Rosenfeld A and Krüger J 2017 IEEE J. Sel. Top. Quantum Electron 23(3) 7581030 DOI: 10.1109/JSTQE.2016.2614183.
- [4] Giannuzzi G, Gaudio C, Di Franco C, Scamarcio G, Lugara P M and Ancona A 2019 Opt. Lasers Eng. 114 15-21 DOI: 10.1016/j.optlaseng.2018.10.006.
- [5] Schwarz S, Rung S, Esen C and Hellmann R 2018 Appl. Sci. 8(9) 1624 DOI: 10.3390/app8091624.
- [6] Tsibidis G D, Skoulas E, Papadopoulos A and Stratakis E 2016 Phys. Rev. B 94(8) 081305 DOI: 10.1103/PhysRevB.94.081305.
- [7] Martsinovskii G A, Shandybina G D, Smirnov D S, Zobotnov S V, Golovan L A, Timoshenko V Yu and Kashkarov P K 2008 Opt. Spectrosc+ 105(1) 67-72 DOI: 10.1134/S0030400X08070114.
- [8] Gurevich E L and Gurevich S V 2014 Appl. Surf. Sci. 302 118-123 DOI: 10.1016/j.apsusc.2013.10.141.
- [9] Liedl G, Pospichal R and Murzin S P 2017 Features of changes in the nanostructure and colorizing of copper during scanning with a femtosecond laser beam Computer Optics 41(4) 504-509 DOI: 10.18287/2412-6179-2017-41-4-504-509.
- [10] Otto A 1968 Zeitschrift für Physik 216(4) 398-410 DOI: 10.1007/BF01391532.
- [11] Zhou K, Jia X, Jia T, Cheng K, Cao K, Zhang S, Feng D and Sun Z 2017 J. Appl. Phys. 121(10) 104301 DOI: 10.1063/1.4978375.
- [12] Raillard B, Mücklich F 2015 Ablation effects of femtosecond laser functionalization on surfaces *Laser Surface Engineering* ed. Lawrence J, Waugh D G (Woodhead Publishing) chapter 24 pp 565-581
- [13] Garrelie F, Colombier J P, Pigeon F, Tonchev S, Faure N, Bounhalli M, Reynaud S and Parriaux O 2011 Opt. Express 19(10) 9035-9043 DOI: 10.1364/OE.19.009035.
- [14] Gräf S and Müller F A 2015 Appl. Surf. Sci. 331 150-155 DOI: 10.1016/j.apsusc.2015.01.056.
- [15] Zhang W, Cheng G, Feng Q, Cao L, Wange F and Hui R 2011 Appl. Surf. Sci. 257(9) 4321-4324 DOI: 10.1016/j.apsusc.2010.12.050.
- [16] Hou S, Huo Y, Xiong P, Zhang Y, Zhang S, Jia T, Sun Z, Qiu J and Xu Z 2011 Phys. D: Appl. Phys. 44(50) 505401 DOI: 10.1088/0022-3727/44/50/505401.
- [17] Huang M, Zhao F, Cheng Y, Xu N and Xu Z 2009 ACS Nano 3(12) 4062-4070 DOI: 10.1021/nn900654v.
- [18] Nivas J J, He S, Rubano A, Vecchione A, Paparo D, Marrucci L, Bruzzese R and Amoroso S 2015 Sci. Rep. 5 17929 DOI: 10.1038/srep17929.
- [19] Ribeiro R M, Ramos M M D, Stoneham A M and Pires J M C 1997 Appl. Surf. Sci. 109-110 158-161 DOI: 10.1016/S0169-4332(96)00747-7.
- [20] Kazanskiy N L, Kharitonov S I, Kozlova I N and Moiseev M A 2018 The connection between the phase problem in optics, focusing of radiation, and the Monge–Kantorovich problem Computer Optics 42(4) 574-587 DOI: 10.18287/2412-6179-2018-42-4-574-587.
- [21] Kharitonov S I, Doskolovich L L and Kazanskiy N L 2016 Solving the inverse problem offocusing laser radiation in a plane region using geometrical optics Computer Optics 40(4) 439-450 DOI: 10.18287/2412-6179-2016-40-4-439-450.

2.2. Improving Tribological Properties of Stainless Steel Surfaces by Femtosecond Laser Irradiation

Published by: MDPI

Journal: Coatings (2020)

DOI: <https://doi.org/10.1088/1742-6596/1745/1/012017>

Serguei P. Murzin^{1,2*}, **Valeriy B. Balyakin**¹, **Gerhard Liedl**², **Alexey A. Melnikov**¹ and **Roland Fürbacher**²

¹ Samara National Research University, Moskovskoe Shosse 34A, Samara, Russian Federation, 443086

² Vienna University of Technology, Institute of Production Engineering and Photonic Technologies, Vienna, Austria

Austria; gerhard.liedl@tuwien.ac.at (G.L.); roland.fuerbacher@tuwien.ac.at (R.F.)

* Correspondence: murzin@ssau.ru

Abstract: A possibility of improving tribological properties by femtosecond laser irradiation on an example of a steel surface by creating regularly arranged micro-grooved textures that contain self-organized microstructures and nano laser-induced periodic surface structures (LIPSS) was determined. The friction coefficient of the treated surface of a sample of cold-rolled 1.4301 stainless steel was evaluated using a CSM Instruments SA tribometer according to a Pin-on-disk test scheme at a specific pressure of 1 MPa. It was found that the coefficient of friction was reduced by 35% compared to the initial ground surface. Such laser treatment can find application for using parts in conditions of dry or boundary friction, mainly in units, in which the use of lubricant is unacceptable or extremely undesirable.

Keywords: tribological properties; sliding friction coefficient; stainless steel; treated surface; femtosecond laser irradiation; self-organized microstructures; nano LIPSS

1. Introduction

Laser treatment, depending on the applied methods, schemes, and processing modes, has a multifactorial effect on the surface condition of the processed materials which has been the subject of numerous studies. To improve tribological properties of materials, along with laser modification methods [1–4], a surface texturing was effectively applied using various laser treatment schemes [5,6]. This method has been successfully applied to structural materials, including metals and alloys as well as ceramics, and provides a decrease in the friction coefficient and an increase in the operational characteristics of machine parts and mechanisms [7–9]. Laser texturing is widely used in a variety of applications for the improvement of tribological properties of surfaces [10]. With the aim of industrial application, the texturing was performed on surfaces of mechanical components, such as piston rings [11,12], thrust and rolling bearings [13–15], injection cams [16], facing seals [17], and cutting tools [18]. It was shown that textured surfaces demonstrated a lowered friction coefficient compared to the untreated analogue under dry friction conditions without lubricant as well as boundary and hydrodynamic lubricating conditions. The use of the laser surface treatment of silicon carbide seal rings to reduce the friction coefficient is known in the practice of producing mechanical gas-dynamic seals [19]. In addition to applications for mechanical components, laser texturing was used to improve tribological properties of bio-implant surfaces, such as dental implants and artificial joints, providing better tribological properties of bio-implant materials [20,21]. This process was also used to improve tribological properties of drive tapes for electronic devices and showed progressive results [22].

Methods of surface structuring by ultrashort laser pulses are also used to improve tribological properties of materials [23–25]. A treatment by a laser beam with a pulse duration in the femtosecond range was performed, implementing an ablation process of the material with transition to the plasma and the gaseous phase, bypassing the liquid melt. In addition to the synthesis of a low-

dimensional periodic structure as a result of self-organization processes initiated by femtosecond laser irradiation [26], a direct microrelief formation by laser treatment was applied [27].

Bonse et al. [28] showed that one of the approaches for an application of femtosecond laser texturing to improve the tribological performance of surfaces can be a creation of ripples or laser-induced periodic surface structures (LIPSS) with spatial periods in the sub-micrometer range, which are formed in a “self-ordered” way during the laser-scan processing of surfaces. In Ref. [29], tribological characteristics of periodic surface structures on metallic materials induced by femtosecond laser irradiation were evaluated, including technologically relevant materials such as titanium-containing materials, stainless steels, and steels. In Ref. [30], an influence on the tribological properties of surfaces of metallic materials by self-ordered nano LIPSS as well as by microstructures was shown that also includes so-called grooves and cones morphologies, which often form in a self-organized way. Schille et al. [31] showed that the high potential of laser textured surface features can be demonstrated for an advanced tribological functionality in a real application.

Wang et al. [32] reported on improving tribological properties of a stainless steel by surface microstructuring with patterning using a femtosecond laser. Regularly arranged micro-grooved textures with a different spacing were produced on stainless steel surfaces by a femtosecond laser. It was shown that the femtosecond laser texturing of the surface is an effective technology to improve tribological properties of steels under dry friction. In addition, as shown by Gachot et al. [33] and Zhang et al. [34], such microreliefs may have properties that are able to retain viscous substances, which, for example, makes it possible to create a system of grooves for lubricant accumulation.

Of interest are studies of the functional response of textured surfaces with various designs, including arrays of nanoripples, micro-irregularities, and grooves [9,30]. The aim of this paper is to determine the possibility of improving tribological properties by femtosecond laser irradiation on an example of a steel surface by creating regularly arranged micro-grooved textures containing self-organized microstructures and nano LIPSS.

2. Materials and Methods

In this study, 1.4301 stainless steel samples were used with a thickness of 2 mm and a ground surface finish. Steel 1.4301 find application in friction assemblies in chemical equipment when functioning in most medium-aggressive environments of chemical industries, including diluted acids and alkalis and organic acids as well as in most salt solutions of organic and inorganic acids at various temperatures and concentrations. In the presence of aggressive environments, parts made of such steel are used at temperatures of up to 350 °C. The chemical composition of X5CrNi18-10-1.4301 steel is presented in Table 1.

Table 1. Chemical composition of X5CrNi18-10-1.4301 steel, weight %.

N	Ni	Cr	S	P	Mn	Si	C	Fe
<0.11	8.0–10.5	17.0–19.5	<0.015	<0.045	<2.0	<1.0	<0.07	basis

The profile measurements of untreated samples showed an arithmetical mean deviation of $R_a = 1.3 \mu\text{m}$ and a maximum height of $S_z = 9 \mu\text{m}$ (according to DIN EN ISO 4287:2010). The surface properties were defined using a roughness measuring instrument, Mahr Marsurf PS 10 (Mahr GmbH, Göttingen, Germany). A Ti:Sapphire (Ti:Al₂O₃) solid state laser (Femtopower Compact Pro, Femtolasers Produktions GmbH, Vienna, Austria) was used to initiate the LIPSS formation and material removal. The system operates at a frequency of 1 kHz, emitting 30 fs pulses at a central wavelength of $\lambda = 800 \text{ nm}$ and a bandwidth of $\pm 50 \text{ nm}$. The laser delivers radiation with an average output power of 800 mW, which leads to a single pulse energy of 0.8 mJ. Due to its internal setup, the output radiation is linearly polarized. To adjust the laser fluence on the samples' surface, a variable attenuator was used. Leaving the attenuator, the laser beam is then focused on the specimen by an off-axis parabolic mirror with a protected silver coating and a focal length of 50.8 mm (angle of incidence 0°). The processing has been conducted in air at 21 °C. The sample surfaces were cleaned in an ultrasonic bath with demineralized water for 20 minutes after structuring and then examined by a scanning electron microscope (SEM), VEGA TESCAN (Brno, Czech Republic).

Changes in the friction coefficients of treated samples were evaluated using a CSM Instruments SA tribometer (Pesieux, Switzerland, Figure 1). The device, designed to measure the coefficient of sliding friction during the contact interaction of two mutually moving surfaces, is a desktop installation consisting of a friction machine with a measuring device and a computer. The method is based on the measurement by a strain gauge of the friction force that occurs from the mutual movement of the test samples pressed against each other with a predefined force in air or in the environment of various lubricants, both consistent and liquid. A Pin-on-disk test scheme was used, in which a flat surface of a fixed cylindrical pin is pressed against a flat sample surface [35]. The friction coefficient is equal to the ratio of the measured friction force to the clamping force.

In the measurement mode, the samples from cold-rolled 1.4301 stainless steel with an applied micro- and/or nanorelief were sequentially installed on the platform. A counterbody (indenter) made of 12H18N10T steel (an analogue of X10CrNiTi18-10 steel) in the form of a pin fixed motionless in the rod holder was mounted on top of the sample at a predefined distance from the rotation axis of the platform. Before each measurement, a balancing of the holder and the counterbody was performed.

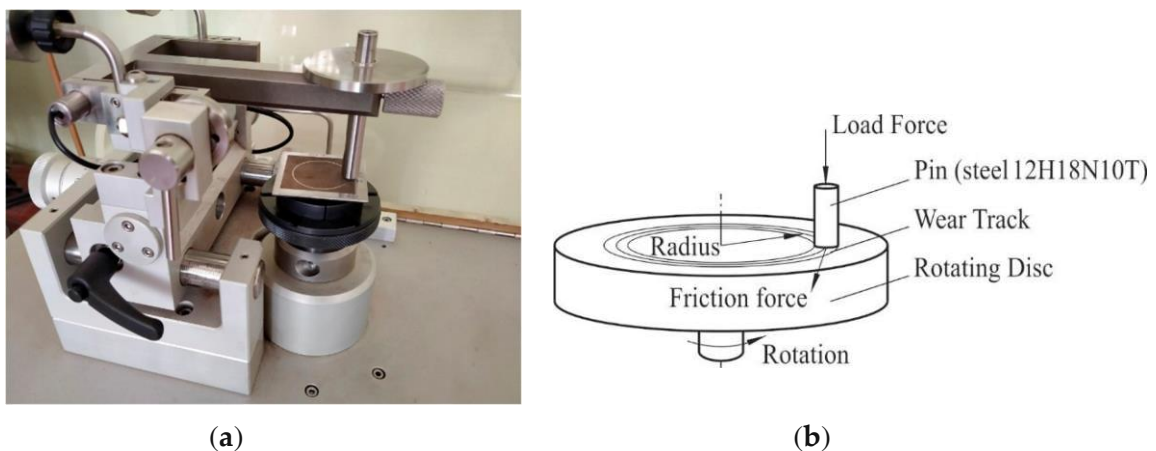


Figure 1. Determination of friction coefficient: (a) photo of CSM Instruments SA tribometer with a test sample and (b) the test scheme.

3. Results and Discussions

3.1. Femtosecond Laser Treatment

The samples of steel were mounted on a positioning system that allows a well-defined translational movement in the x, y, and z directions. The movement in the z-direction was used to modify the distance of the sample surface to the parabolic focusing mirror. The fluence was adjusted by means of a variable attenuator. The samples' movements along the x-axis and stepwise movements between the scanning lines along the y-axis were used to form LIPSS or cone-shaped microstructures. The distances between the scanning lines were chosen to allow the overlapping of the formable LIPSS on the 162-I sample surface as well as the periodic cone-shaped microstructures on the 164-I sample surface. This was made to implement a comparison of the tribological properties of nanostructures (LIPSS) that were created near the ablation threshold with properties of coneshaped microstructures. Since LIPSS can only be generated below the ablation threshold of the selected material, the fluence was adjusted by moving the sample out of focus along the z-axis.

Treatment in the x-direction followed by another in the y-direction were used to generate a gridshaped microstructure for the 163-I sample. Regularly arranged micro-grooved textures containing self-organized hierarchical structures micro/LIPSS were produced with different distances between the grooves. The gridwise pattern and distances were chosen on the condition that grooves with selforganized hierarchical micro/LIPSS structures will occupy at least 2/3 of the sample area. At the same time, an equal area ratio of more than 10% for the raw ground initial surface and formed nano LIPSS was maintained. The used sets of parameters are summarized in Table 2.

Table 2. Sets of parameters for the laser structuring of 1.4301 stainless steel.

Sample ID	Structure Description	Fluence φ [J/cm ²]	Feed Rate f [mm/s]	Gap Width a [μm]
162-I	Nano, line	0.44	8.33	160
163-I	Micro, grid	2.74	1.67	100
164-I	Micro, grid	2.74	0.42	50

Accordingly, the samples were prepared in such a way that different ablation modes were established. For fluences below the ablation threshold, only nanosized LIPSS have been generated. The second sample has been prepared at higher fluences, which caused the formation of a certain microstructure, together with nanosized LIPSS. The third sample was prepared with different parameters, where no LIPSS at all were formed. As a consequence, only microstructures and no LIPSS were present in that sample.

The SEM images of 162-I sample were analyzed perpendicular to the LIPSS orientation using Fast Fourier Transformation (FFT), a fast Fourier transform is an algorithm that computes the discrete Fourier transform, with the MATLAB software (version R2018b) to determine the LIPSS periodicity. Therefore, each pixel row of the image was transformed into a frequency domain, and an average frequency distribution over all the rows was calculated. The resulting spectrum was further investigated to reveal distinct peaks. Those peaks can be interpreted as the favorable spatial LIPSS periods, and the amplitude gives an indication of their characteristics. The FFT analysis of the 162-I sample showed a frequency peak at $1.71 \mu\text{m}^{-1}$, which corresponds to the main spatial period of $0.58 \mu\text{m}$. A local transition to higher spatial frequencies, which was also identified by FFT analysis, can be seen in Figure 2. These local LIPSS frequency transitions are caused by laser intensity variations due to the sample's surface roughness, and this led to local spatial periods of $0.36 \mu\text{m}$.

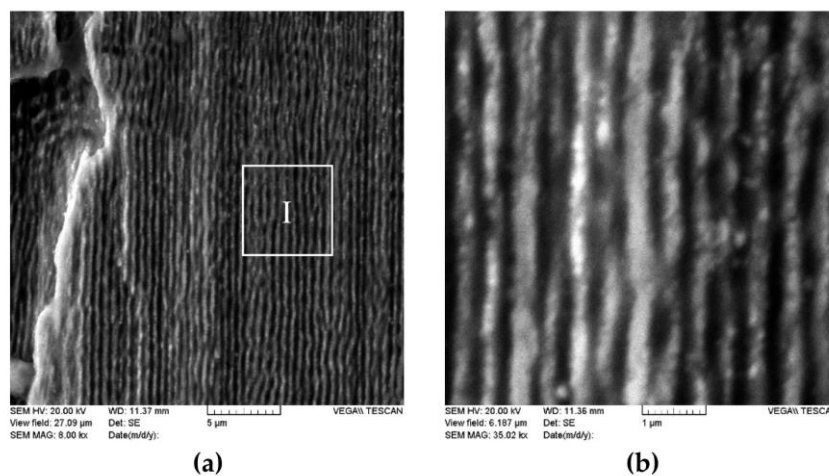


Figure 2. SEM images: (a) surface nano laser-induced periodic surface structures (LIPSS) formed using a femtosecond laser irradiation on a grinded steel surface; (b) enlargement of the marked area I.

The SEM images of the micro-structured 163-I sample revealed not only regions where the material was removed through ablation caused by a high fluence but also the formation of LIPSS near the fringes of the ablated zones (Figures 3 and 4). These hierarchical structures with micrometer-sized structures at the bottom and nanometer-sized structures on the top can lead to a change in the behavior of the surface. On the 164-I sample surface LIPSS were absent, but periodic cone-shaped microstructures were present (Figure 5).

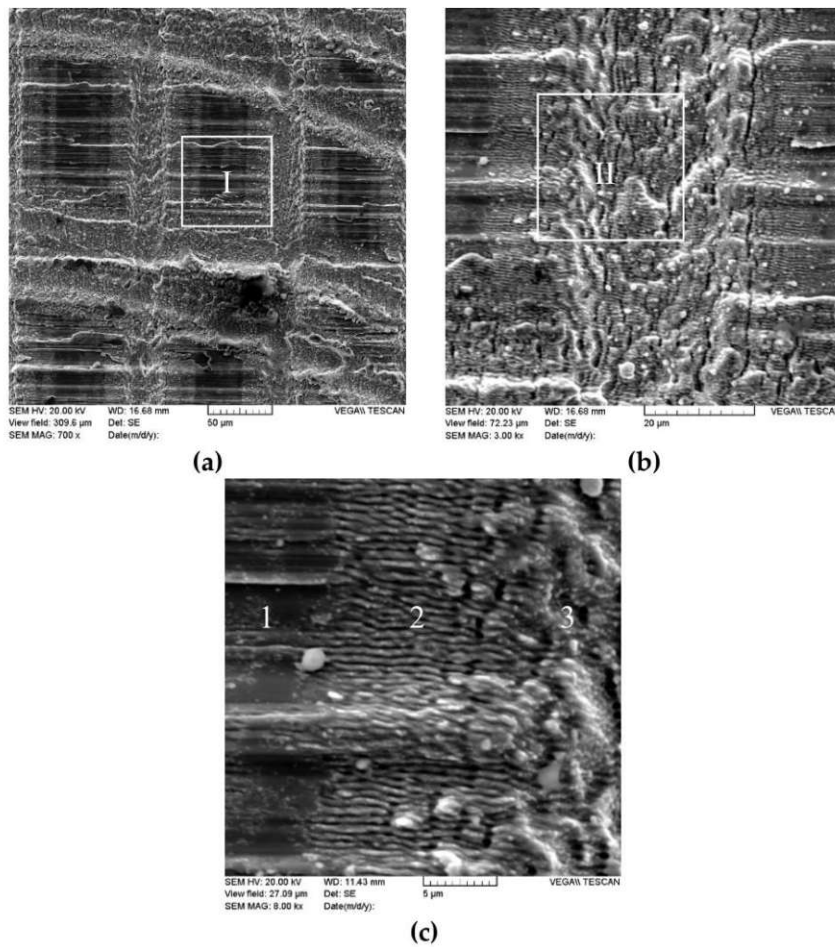


Figure 3. SEM images: (a) regularly arranged micro-grooved textures containing self-organized hierarchical structures micro/LIPSS; (b) enlargement of the marked area I. (c) Enlargement of the marked area II: 1—initial grinded surface; 2—nano LIPSS; 3—groove with self-organized hierarchical micro/LIPSS structures.

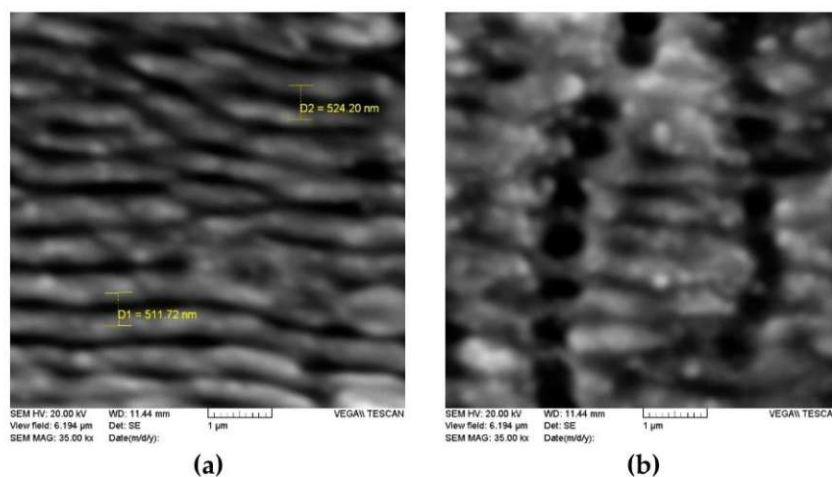


Figure 4. SEM images: (a) nano LIPSS and (b) self-organized hierarchical structures of micro/LIPSS in the groove.

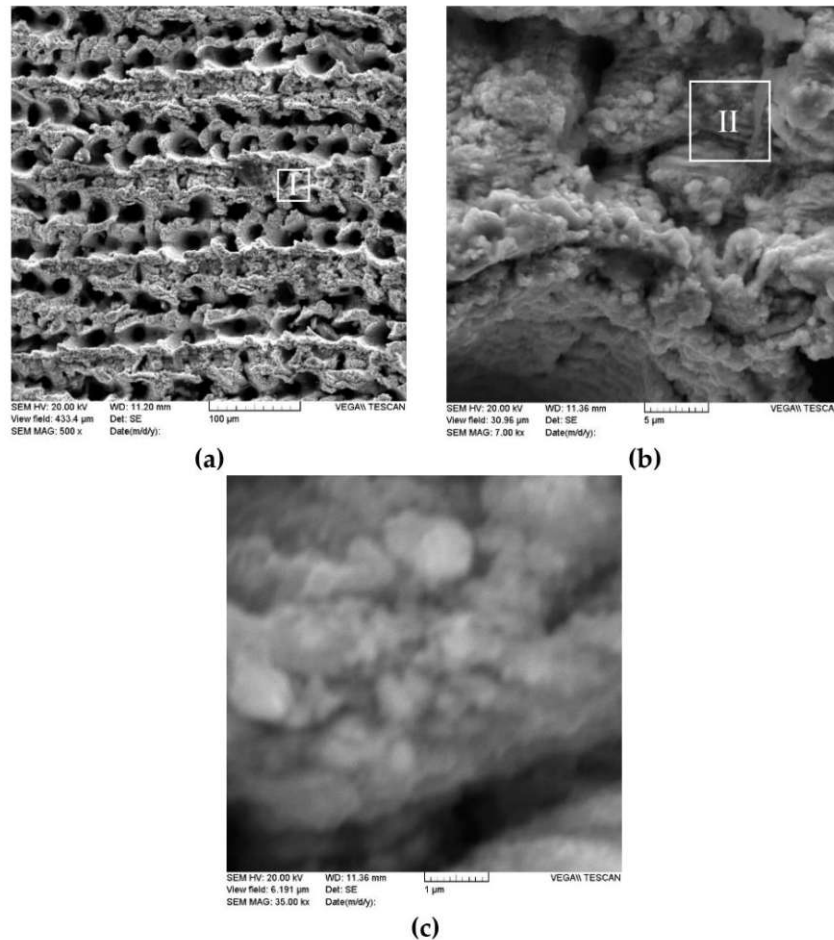


Figure 5. SEM images: (a) periodic cone-shaped microstructures on the sample surface; (b) enlargement of the marked area I; (c) enlargement of the marked area II.

3.2. Determination of Sliding Friction Coefficient

The sliding friction coefficient was determined without lubrication at an ambient temperature of 25 °C and a relative humidity of 63%. The pressing force was created by placing a weight holder with a known mass on the stand. A specific pressure of 1 MPa was realized at a load force of 1 N, while the linear sliding speed was 0.5 m/s and the length of sliding was 50 m, with a test radius of 15 mm. In the device, friction force sensors are connected to the counterbody holder. The friction coefficient was measured during the rotational movement of the sample relative to the counterbody, while the wear groove on the sample had a circle shape. During the tests, the friction coefficient was measured with a frequency of 1000 measurements per minute; these values were statistically processed by the CSM tribometer software package, which determined the maximum, minimum, and average values, as well as the standard deviation. The arithmetic mean values obtained after processing the statistical matrix of more than 1650 measurements for each series of tests were determined. This number of measurements for each series of tests provides a measurement reliability of 0.997.

The standard deviation of the average value of the friction coefficient was determined by software for experimental equipment for each point and was in the range of 0.002–0.04. However, a comparison of the friction coefficient before and after the laser surface treatment was performed using an average value. The systematic error was eliminated by calibrating the experimental setup before each series of measurements.

As a result of experimental studies, it was found that for the initial surface of the samples, the average value of the friction coefficient in contact with a specific pressure of 1 MPa was 0.149, with a mean square deviation of 0.002. Figure 6 shows the dependence of the friction coefficient on the length of sliding for the laser-untreated sample surface. The average value of the friction coefficient for the 162-I sample, on the surface of which a LIPSS nanostructure was formed using femtosecond laser

irradiation, was in the range of 0.14–0.15. Moreover, the maximum value was recorded when the movement started. In the initial 6–7 s, a decrease in the friction coefficient to the minimum value was observed, and afterwards an almost monotonous increase up to the value of 0.145 with a mean square deviation of 0.0025 (Figure 7) was registered.

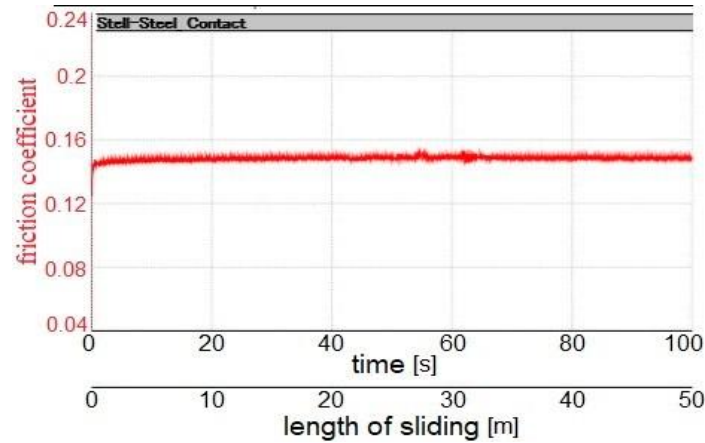


Figure 6. Dependence of the friction coefficient on the length of sliding for the laser-untreated sample surface.

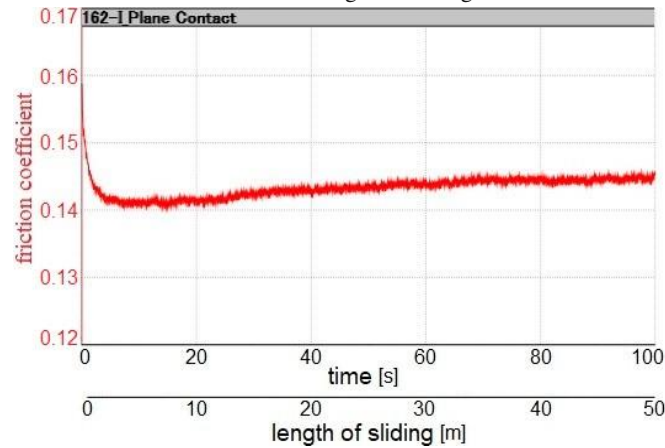


Figure 7. Dependence of the friction coefficient on the length of sliding for the 162-I sample surface.

The friction coefficient for the 163-I sample surface was studied, with its surface showing a hierarchical structure with cones in the micrometer range from the bottom and nanoscaled LIPSS at the top, formed at higher accumulated energy densities. The friction coefficient of the surface, which was a hierarchical structure of micro/LIPSS, was 0.12 at the time when the movement started, and in less than 10 seconds it decreased to 0.1 (Figure 8). Further in the course of the study, a decrease in the coefficient of the sliding friction of the sample to an arithmetic mean value of 0.096 with a mean square deviation of 0.0035 was observed. Thus, it was found that the coefficient of friction was reduced by 35%. For the 164-I sample, the surface of which was characterized by the absence of LIPSS and the presence of larger self-organizing periodic cone-shaped structures that were formed at a further increase in the accumulated energy density after laser treatment, the friction coefficient during the studies increased in the range of 0.1 (at the initial moment) to 0.2 (Figure 9). The average value in this test interval was 0.147, with a mean square deviation of 0.04. SEM images of the wear areas of sample surfaces are shown in Figure 10.

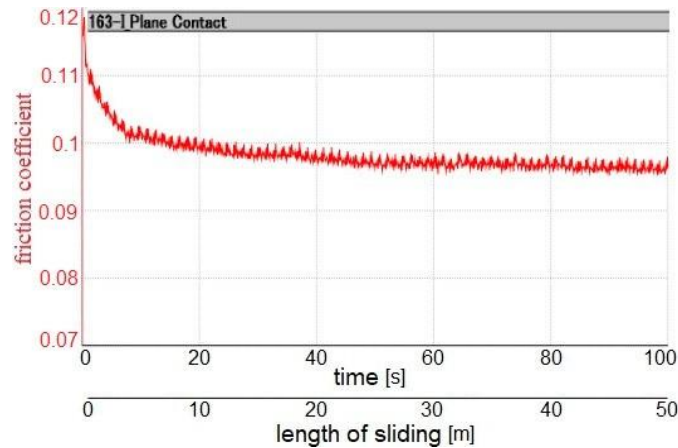


Figure 8. Dependence of the friction coefficient on the length of sliding for the 163-I sample surface.

The change in the friction coefficient during tests is explained by the surface wear of samples. An analysis of the graph from Figure 8 shows that during the tests, the friction coefficient decreased slightly, which is explained by a decrease in the surface roughness due to polishing. A shiny polished surface was observed visually, whose SEM image is shown in Figure 10. Surface wear was measured using an indicator-type micrometer. The wear value of the 163-I sample surface was less than the division interval of the scale, which was $1\ \mu\text{m}$. As shown in Figure 7, the friction coefficient of the 162-I sample first decreased and then began to increase slightly, which can be explained by the beginning of the surface wear. The measurement of the depth of the groove showed a wear of $1\text{--}2\ \mu\text{m}$. The wear during testing of the 164-I sample was $15\text{--}17\ \mu\text{m}$, which is by an order greater (Figure 9). In this case, the indenter, which has the shape of a rectangular prism, cut deep into the sample, as a result of which additional resistance appeared and the friction coefficient began to increase linearly. Therefore, it can be claimed that the laser processing of 1.4301 steel by irradiation with a femtosecond laser with the creation of a hierarchical structure with cones in the micrometer range from the bottom side and LIPSS in the nanometer range on the top reduces the friction values for pairs of stainless steel. Thus, the feasibility of creating a hierarchical micro/LIPSS structure to reduce the friction coefficient of steel was determined.

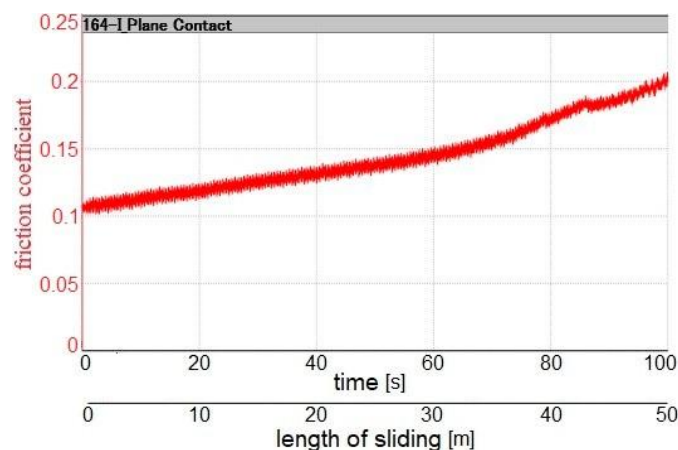


Figure 9. Dependence of the friction coefficient on the length of sliding for the 164-I sample surface.

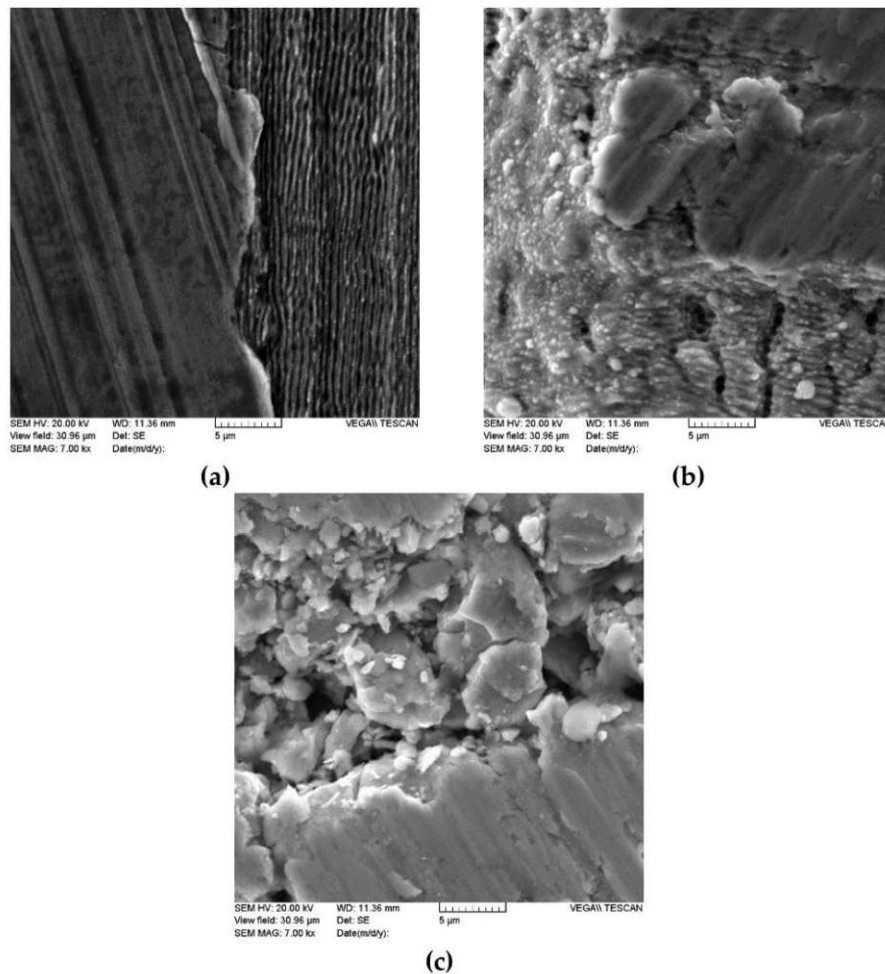


Figure 10. SEM images of the wear areas of samples surfaces: (a) 162-I, (b) 163-I, (c) and 164-I in the study of the friction coefficient.

3.3. Application Possibilities in Friction Units

Such processing can find application when using parts made of 1.4301 steel in friction units of many types of equipment in which the use of lubricants is unacceptable or extremely undesirable. For example, production technology often excludes lubrication in machines used for food, textiles, and paper, as well as chemical industries. In this case, components function in conditions of dry friction, which occurs in the absence of lubrication and contamination between the surfaces. Stainless steel textured surfaces with arrays of nanoripples, micro-irregularities, and grooves can be used in conditions of boundary friction, in which the surfaces are separated by a lubricant layer so thin that it has special properties different from the bulk properties of the lubricant and depending on the nature and condition of the rubbing surfaces.

The main factors that should be taken into account primarily when choosing materials and processing methods are load characteristics (contact pressure, sliding speed), specified technical lifetime (total lifetime of the friction unit), temperature at operating conditions, lubrication conditions (presence and type of lubricant), the kind of environment (atmospheric air or inert gas and their humidity, or vacuum), and requirements for the friction coefficient. Laser processing with surface texturing on a hierarchical scale could prove to be helpful for parts experiencing sliding friction, such as components of centrifuge rotors; sieves; centrifuge screws; mechanical seal ring, e.g., of axial sealing devices; and many more.

4. Conclusions

A possibility of improving tribological properties by femtosecond laser irradiation on the example of a steel surface by creating regular arranged micro-grooved textures containing selforganized microstructures and nano LIPSS was determined. The friction coefficient of the treated surface of samples of cold-rolled 1.4301 stainless steel was studied. This surface had a hierarchical structure with micrometer-sized cones at the bottom and nanoscaled LIPSS at the top. Changes in the friction coefficients of the treated samples were evaluated using a CSM Instruments SA tribometer according to the Pin-on-disk test scheme at a specific pressure of 1 MPa.

The measured friction coefficient of the surface, with its regularly arranged micro-grooved texture containing self-organized hierarchical structures of microstructures/LIPSS, was 0.12 at the beginning of the measurement, when the movement started. In less than 10 seconds, the friction coefficient decreased to 0.1. Subsequently, the sliding coefficient of the sample decreased to a value of 0.096 during the study. Thus, it was found that the coefficient of friction was reduced by 35% compared to the initial ground surface.

Such processing could be applied to components made of 1.4301 steel used under the conditions of dry or boundary friction, mainly in friction assemblies of machine types in food, textile, paper, and chemical industries, where the use of lubricants is unacceptable or extremely undesirable. Laser treatment with surface texturing can be recommended for parts of sliding friction units—for example, components of centrifuge rotors, sieves, centrifuge screws, mechanical seal rings of axial sealing devices, etc.

Author Contributions: Conceptualization, S.P.M. and G.L.; Methodology, S.P.M., V.B.B., and G.L.; Software, A.A.M. and R.F.; Validation, V.B.B. and G.L.; Formal analysis, G.L.; Investigation, V.B.B., A.A.M., and R.F.; Resources, S.P.M. and G.L.; Data curation, S.P.M., V.B.B. and G.L.; Writing—original draft preparation, S.P.M. and R.F.; Writing—review and editing, S.P.M. and G.L.; Visualization, V.B.B. and A.A.M.; Supervision, S.P.M.; Project administration, S.P.M.; Funding acquisition, S.P.M. and G.L. All authors have read and agreed to the published version of the manuscript.

Funding: This research received no external funding.

Conflicts of Interest: The authors declare no conflict of interest.

References

1. Wagh, Y.R.; Paul, S.; Gupta, N.; Singh, R.K. Metallurgical and tribological investigation of micro-scale fibre laser-based surface hardening. *Int. J. Mechatron. Manuf. Syst.* **2018**, *11*, 120–134.
2. Siddaiah, A.; Mao, B.; Liao, Y.; Menezes, P.L. Surface characterization and tribological performance of laser shock peened steel surfaces. *Surf. Coat. Technol.* **2018**, *351*, 188–197.
3. Sidashov, A.V.; Kozakov, A.T.; Yares'ko, S.I.; Kakovkina, N.G.; Manturov, D.S. Study of the phase composition and tribological properties of carbon tool steels after laser surface hardening by quasi - CW fiber laser. *Surf. Coat. Technol.* **2020**, *385*, 125427.
4. Garcia-Giron, A.; Romano, J.M.; Liang, Y.; Dashtbozorg, B.; Dong, H.; Penchev, P.; Dimov, S.S. Combined surface hardening and laser patterning approach for functionalising stainless steel surfaces. *Appl. Surf. Sci.* **2018**, *439*, 516–524.
5. He, Y.; Zou, P.; Zhu, Z.; Zhu, W.-L.; Yang, X.; Cao, J.; Ehmman, K.F. Design and application of a flexurebased oscillation mechanism for surface texturing. *J. Manuf. Process.* **2018**, *32*, 298–306.
6. Zhan, X.; Yi, P.; Liu, Y.; Xiao, P.; Zhu, X.; Ma, J. Effects of single- and multi-shape laser-textured surfaces on tribological properties under dry friction. *Proc. Inst. Mech. Eng. C: J. Mech. Eng. Sci.* **2020**, *234*, 1382–1392.
7. Grützmacher, P.G.; Profito, F.J.; Rosenkranz, A. Multi-scale surface texturing in tribology - current knowledge and future perspectives. *Lubricants.* **2019**, *7*, 95.
8. Zhang, W.; Yamashita, S.; Kumazawa, T.; Ozeki, F.; Hyuga, H.; Kita, H. Effect of nanorelief structure formed in situ on tribological properties of ceramics in dry sliding. *Ceram. Int.* **2019**, *45*, 13818–13824.
9. Bhaduri, D.; Batal, A.; Dimov, S.S.; Zhang, Z.; Dong, H.; Fallqvist, M.; M'Saoubi, R. On design and tribological behaviour of laser textured surfaces. *Procedia. CIRP.* **2017**, *60*, 20–25.

10. Mao, B.; Siddaiah, A.; Liao, Y.; Menezes, P.L. Laser surface texturing and related techniques for enhancing tribological performance of engineering materials: A review. *J. Manuf. Process.* **2020**, *53*, 153–173.
11. Ryk, G.; Etsion I. Testing piston rings with partial laser surface texturing for friction reduction. *Wear.* **2006**, *261*, 792–796.
12. Ezhilmaran, V.; Vijayaraghavan, L.; Vasa N. Investigation of Nd³⁺: YAG laser aided surface texturing to improve tribological characteristics of piston ring. *J Laser Micro NanoEng.* **2017**, *12*, 195–202.
13. Etsion, I.; Halperin, G.; Brizmer, V.; Kligerman, Y. Experimental investigation of laser surface textured parallel thrust bearings. *Tribol Lett.* **2004**, *17*, 295–300.
14. Murzin, S.P.; Balyakin, V.B. Microstructuring the surface of silicon carbide ceramic by laser action for reducing friction losses in rolling bearings. *Opt. Laser. Technol.* **2017**, *88*, 96–98.
15. Houdková, Š.; Šperka, P.; Repka, M.; Martan, J.; Moskal, D. Shifted laser surface texturing for bearings applications. *J Phys. Conf. Ser.* **2017**, *843*, 012076.
16. Kang, Z.; Fu, Y.; Ji, J.; Puoza, J.C. Effect of local laser surface texturing on tribological performance of injection cam. *Int J Adv Manuf Technol.* **2017**, *92*, 1751–1760.
17. Wan, Y.; Xiong, D.-S. The effect of laser surface texturing on frictional performance of face seal. *J Mater Process Technol.* **2008**, *197*, 96–100.
18. Xing, Y.; Deng, J.; Zhao, J.; Zhang, G.; Zhang, K. Cutting performance and wear mechanism of nanoscale and microscale textured Al₂O₃/TiC ceramic tools in dry cutting of hardened steel. *Int. J. Refract. Met. Hard. Mater.* **2014**, *43*, 46–58.
19. Murzin, S.P.; Balyakin, V.B.; Melnikov, A.A.; Vasiliev, N.N.; Lichtner, P.I. Determining ways of improving the tribological properties of the silicon carbide ceramic using a pulse-periodic laser treatment. *Comput. Opt.* **2015**, *39*, 64–69.
20. Hu, T.; Hu, L.; Ding, Q. Effective solution for the tribological problems of Ti-6Al-4V: combination of laser surface texturing and solid lubricant film. *Surf Coat Technol.* **2012**, *206*, 5060–5066.
21. Pflöging, W.; Kumari, R.; Besser, H.; Scharnweber, T.; Majumdar, J.D. Laser surface textured titanium alloy (Ti-6Al-4V): part 1—surface characterization. *Appl Surf. Sci.* **2015**, *355*, 104–111.
22. Raeymaekers, B.; Etsion, I.; Talke, F.E. Enhancing tribological performance of the magnetic tape/guide interface by laser surface texturing. *Tribol. Lett.* **2007**, *27*, 89–95.
23. Voyer, J.; Ausserer, F.; Klien, S.; Ristow, A.; Velkavrh, I.; Diem, A.; Zehetner, J.; Stroj, S.; Heidegger, S.; Bertschler, C.; Edlinger, J. Sub-micro laser modifications of tribological surfaces. *Mater. Perform. Charact.* **2017**, *6*, 42–57.
24. Bathe, R.; Sai Krishna, V.; Nikumb, S.K.; Padmanabham, G. Laser surface texturing of gray cast iron for improving tribological behavior. *Appl. Phys. A.* **2014**, *117*, 117–123.
25. Yang, L.; Ding, Y.; Cheng, B.; He, J.; Wang, G.; Wang, Y. Investigations on femtosecond laser modified micro-textured surface with anti-friction property on bearing steel GCr15. *Appl. Surf. Sci.* **2018**, *434*, 831–842.
26. Nayak, B.K.; Gupta, M.C. Self-organized micro/nano structures in metal surfaces by ultrafast laser irradiation. *Opt. Lasers Eng.* **2010**, *48*, 940–949.
27. Lehr, J.; Kietzig, A.-M. Production of homogenous micro-structures by femtosecond laser micro-machining. *Opt. Lasers Eng.* **2014**, *57*, 121–129.
28. Bonse, J.; Koter, R.; Hartelt, M.; Spaltmann, D.; Pentzien, S.; Höhm, S.; Rosenfeld, A.; Krüger, J. Femtosecond laser-induced periodic surface structures on steel and titanium alloy for tribological applications. *Appl. Phys. A.* **2014**, *117*, 103–110.
29. Bonse, J.; Koter, R.; Hartelt, M.; Spaltmann, D.; Pentzien, S.; Höhm, S.; Rosenfeld, A.; Krüger, J. Tribological performance of femtosecond laser-induced periodic surface structures on titanium and a high toughness bearing steel. *Appl. Surf. Sci.* **2015**, *336*, 21–27.
30. Bonse, J.; Kirner, S.V.; Griepentrog, M.; Spaltmann, D.; Krüger, J. Femtosecond laser texturing of surfaces for tribological applications. *Material.* **2018**, *11*, 801.
31. Schille, J.; Schneider, L.; Mauersberger, S.; Szokup, S.; Höhm, S.; Pötschke, J.; Reiß, F.; Leidich, E.; Löschner, U. High-Rate laser surface texturing for advanced tribological functionality. *Lubricants.* **2020**, *8*, 33.
32. Wang, Z.; Zhao, Q.; Wang, C.; Zhang, Y. Modulation of dry tribological property of stainless steel by femtosecond laser surface texturing. *Appl. Phys. A.* **2015**, *119*, 1155–1163.
33. Gachot, C.; Rosenkranz, A.; Hsu, S.M.; Costa, H.L. A critical assessment of surface texturing for friction and wear improvement. *Wear.* **2017**, *372–373*, 21–41.

34. Zhang, J.; Yang, D.; Rosenkranz, A.; Zhang, J.; Zhao, L.; Song, C.; Yan, Y.; Sun, T. Laser surface texturing of stainless steel - effect of pulse duration on texture's morphology and frictional response. *Adv. Eng. Mater.* **2019**, *21*, 1801016.
35. Stachowiak, G.W.; Batchelor, A.W. *Experimental Methods in Tribology*; Elsevier Science: Amsterdam, The Netherlands, 2004; p. 363.

2.3. Investigations on the Wetting and Deicing Behavior of Laser Treated Hydrophobic Steel Surfaces

Presented at: SPIE LASE 2021
Published by: SPIE (2021)
Journal: Proceedings of SPIE
DOI: <https://doi.org/10.1117/12.2578138>

Roland Fürbacher*^a, Gerhard Liedl^a

^aInstitute of Production Engineering and Photonic Technologies, TU Wien, Getreidemarkt 9, Vienna, Austria 1060

ABSTRACT

Biomimetic technical surfaces are very interesting for a wide field of possible applications in material science and engineering. For example, changing the wetting and deicing properties of components used in cold environmental conditions can help to reduce ice or snow aggregation, and thereby improve functionality and operational stability. In this study we investigate the correlation between wetting and deicing behavior of micro- and nanostructured stainless steel samples (1.4301). The samples were modified using a Ti:Sapphire femtosecond laser system with 800 nm central wavelength, a pulse duration of 30 fs and a repetition rate of 1 kHz. We generated two fundamentally different types of hydrophobic and superhydrophobic structures by varying the laser fluence and the number of applied pulses, thereby creating hierarchical structures in the micrometer regime and laser induced periodic surface structures (LIPSS) in the nanometer regime. The static water contact angle has been measured to quantify wetting properties of laser treated samples. To determine the ice adhesion shear stresses at the ice/steel-interface, cuvette encased ice columns were frozen onto the structured samples and sheared off by a push rod, while recording the forces. Several icing/deicing cycles have been carried out to investigate a possible decline in wetting behavior due to wear or other mechanisms. We could show, that surfaces with hierarchical microstructures and superhydrophobic wetting behavior will lose its ability to repel the applied water while freezing. Larger structures with higher surface roughness lead to increased ice adhesion shear stresses compared to the initial unstructured surface. LIPSS on the other hand might be not as hydrophobic, but showed lower ice adhesion in the range of the reference sample.

Keywords: Surface modification, laser structuring, laser induced periodic surface structures (LIPSS), icephobic, hydrophobic, ice adhesion, deicing

2.4. Fast Transition from Hydrophilic to Superhydrophobic, Icephobic Properties of Stainless Steel Samples after Femtosecond Laser Processing and Exposure to Hydrocarbons

Presented at: LANE 2022

Published by: Elsevier (2022)

Journal: Procedia CIRP 111

DOI: <https://doi.org/10.1016/j.procir.2022.08.016>

Roland Fürbacher*^a, Gerhard Liedl^a, Andreas Otto^a

^aInstitute of Production Engineering and Photonic Technologies, TU Wien, Getreidemarkt 9, Vienna 1060, Austria

Abstract

Femtosecond laser processing is a key technology for surface modification and can be used to trigger superhydrophobic behavior through a combination of topographical and chemical effects. Nevertheless, immediately after laser processing, steel samples appear superhydrophilic and evolve into a hydrophobic state over a period of several days to weeks. To reduce the wetting transformation time down to hours, the sample can be stored in a vacuum chamber. In the chamber, the absence of atmosphere and thereby water vapor leads to an increased adsorption of hydrocarbons by the surface. In this study, we investigate an alternative and less demanding approach for shortening the wetting transformation time significantly by exposing the laser treated samples to a hydrocarbon liquid/atmosphere. This not only leads to a faster transformation, but also to an improved deicing performance. Both effects are analyzed for various hydrocarbon liquids and different laser patterns with respect to the surface chemistry.

Keywords: Femtosecond laser; surface modification; hydrocarbon exposure; superhydrophobic; icephobic

1. Introduction

Superhydrophobic surfaces which are also icephobic are of great importance for various scientific and industrial applications. Laser processing has been proven as a reliable method for surface modification in order to change the wettability properties of materials to superhydrophobic and also decrease ice adhesion [1, 2, 3]. Nevertheless, immediately after laser processing, metal surfaces appear hydrophilic and evolve into a hydrophobic state over a period of several days to weeks [4, 5]. It is assumed that this effect is due to a chemical reaction that is triggered by the incident laser energy which initially causes the oxidation of the top surface layer. Over time, organic hydrocarbons from the ambient air will be adsorbed and cause the wettability to change [4]. Since this period is dependent on the applied laser energy, the structure topography and the storage condition, ways to accelerate the transformation have been studied. Heat treatment after laser processing is one method for shortening the wetting transformation time [6]. Ngo et al. treated laser structured stainless steel samples in a conventional oven at a temperature of 100 °C. After 4 hours, the samples turned superhydrophobic (contact angles > 150°) and showed low roll-off-angles < 25°. The chemical reaction is described as a decomposition of CO₂ and the formation of Fe₃C on the surface.

Another method to shorten the wetting transformation time is vacuum processing. Hauschwitz et al. showed, that the storage of a freshly laser treated aluminum sample in a high vacuum (10⁻⁸ mbar) over a period of 4 hours resulted in a superhydrophobic surface [7]. They traced it back to a formation of an oxide layer (polar) due to the laser irradiation, which attracts water molecules from the ambient air to form a hydroxylated layer. Hydroxyl groups can lead to chemisorption of organic molecules (e.g. hydrocarbons) and formation of a non-polar, hydrophobic layer. Under ambient air storage conditions, this process of chemisorption is decelerated by water vapor. In the vacuum chamber, water vapor residues are removed and hydrocarbons from inside the chamber are adsorbed by the surface. These hydrocarbons are likely to originate from contaminations due to insufficiently cleaned samples or from oil lubricated vacuum pumps [8].

Unfortunately, superhydrophobic surfaces are not necessarily icephobic [9]. Depending on the resulting surface topography and chemistry, laser structures can influence the anti-icing-performance in either way [3, 5]. Very rough structures in the micro-meter regime may lead to mechanical locking in the ice/substrate interface, if the Cassie-Baxter wetting state cannot be maintained during the phase change which results in a significant increase in ice adhesion [10].





This work focuses on the wetting transformation time of laser structured stainless steel samples, exposed to hydrocarbon liquids or hydrocarbon atmospheres to accelerate the chemical transition described above. The results include the effect of surface topography and have been compared to the method of vacuum processing. We further investigated the impact of these treatments on the deicing performance by determining the ice adhesion shear stress. The ice adhesion measurements were repeated to analyze the durability of the created surface layers and potential mechanical wear of the surface structures.

2. Experimental section

2.1. Femtosecond laser processing

For the experiments we used a femtosecond laser system (Femtopower Compact Pro) consisting of a Ti:Sapphire oscillator and a multi-pass Ti:Sapphire amplifier (CPA scheme). It emits broadband 30 fs laser pulses at a rate of 1 kHz, a central wavelength of 800 nm and a maximum pulse energy of 0.8 mJ. Due to its internal setup, the output radiation is linearly polarized, which is a requirement for the formation of laser induced periodic surface structures (LIPSS). To adjust the laser fluence on the specimens' surface, a variable attenuator was used (Fig. 1). For laser structuring, the laser beam was focused by a plano-convex spherical lens with a focal length of 100 mm. In this experiment, we worked with a Gaussian intensity distribution. Structure 1 (LIPSS) was generated with a spot diameter of 200 μm and by horizontal line scanning, structure 2 & 4 with a spot diameter of 50 μm by intersecting line scanning and structure 3 with a spot diameter of 50 μm by repetitive static laser ablation of material to create a micro dimple array. The experiments have been conducted perpendicular to the sample surface (angle of incidence 0°) in a controlled environment at $21 \text{ }^\circ\text{C} \pm 0.5 \text{ }^\circ\text{C}$ and a humidity of $45\% \pm 5\%$ in air without the use of an inert shielding gas.

Table 1. Laser machining parameters.

Structure ID	Pattern type	Fluence [J/cm^2]	Hatch distance [μm]	Number of pulses
1	LIPSS 	0.6	150	25
2	Grid 	15	100	25
3	Dimple 	20	50	80
4	Triangle 	10	100	25

The pulse overlap and thereby the number of laser pulses applied on the same surface area was adjusted via the feed rate of the 3-axis motorized translation stage (Aerotech), except for structure 3. We used cold rolled stainless steel samples (1.4301) with a thickness of 2 mm. Before laser processing, the samples were cleaned with acetone, air-dried and placed onto a vacuum plate. The laser machining parameters used in this experiment are summarized in table 1.

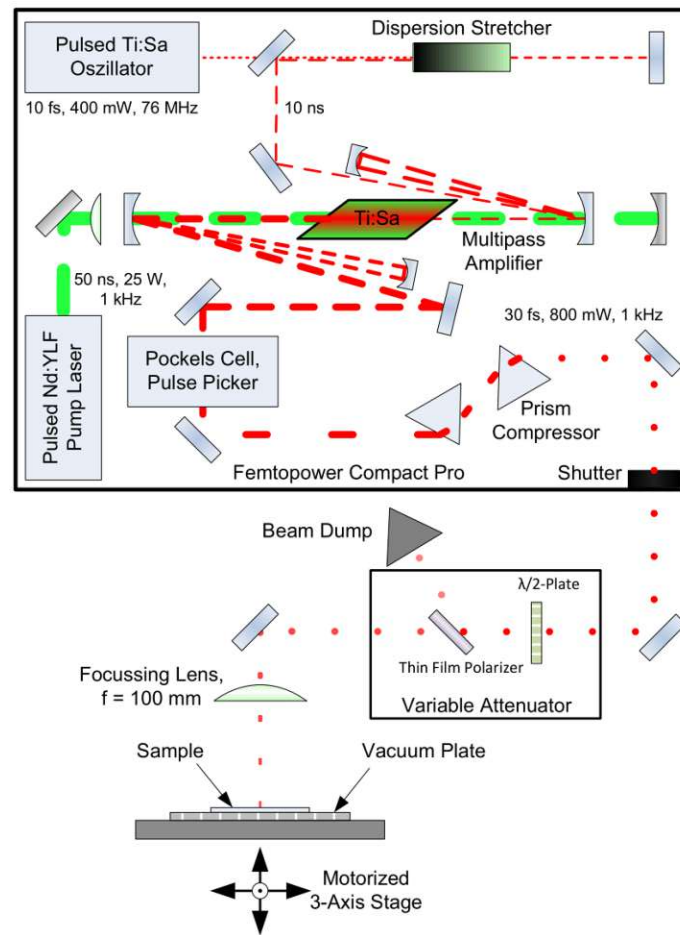


Fig. 1. Schematic depiction of the femtosecond laser system and the experimental setup.

2.2. Surface structures and characterization

In order to investigate the effect of the surface topography on the wetting transformation time, the final wettability and the resulting ice adhesion, we prepared sample surfaces with different structures. By modifying laser parameters, structures from nano-scale LIPSS to relatively rough micro-structures have been generated (Fig. 2). Due to the known influence of vacuum exposure on the results, SEM images have been taken at the end of the experiment using a Jeol JCM-5000 instrument.

Table 2. Surface topography after laser processing; Sa – arithmetic mean deviation, Sz – maximum height, Sdr – developed interfacial area ratio.

Structure ID	Pattern type	Sa [μm]	Sz [μm]	Sdr [%]
1	LIPSS	0.25	4.80	1.2
2	Grid	1.90	19.17	14.1
3	Dimple	8.26	58.11	437.5
4	Triangle	2.02	24.17	26.2

The surface topography parameters were obtained with an Alicona Infinite Focus 3D measurement system (table 2). The Sdr-parameter (developed interfacial area ratio) describes the increase of surface area due to roughness and micro structures compared to the planar area, but does not include the contribution of LIPSS due to limited resolution of the measurement system. The results show a significant increase in surface area of structure 3 due to deep ablation and ejected, resolidified material which formed on the dimple edges. The dimple structures had a mean depth of 50 μm and a diameter of 30 μm . For analysis of the LIPSS spatial frequency, a Fast Fourier Transformation (FFT) of the SEM

images perpendicular to the LIPSS orientation was performed. It showed a mean spatial period of 560 nm, which is consistent with previous findings [11].

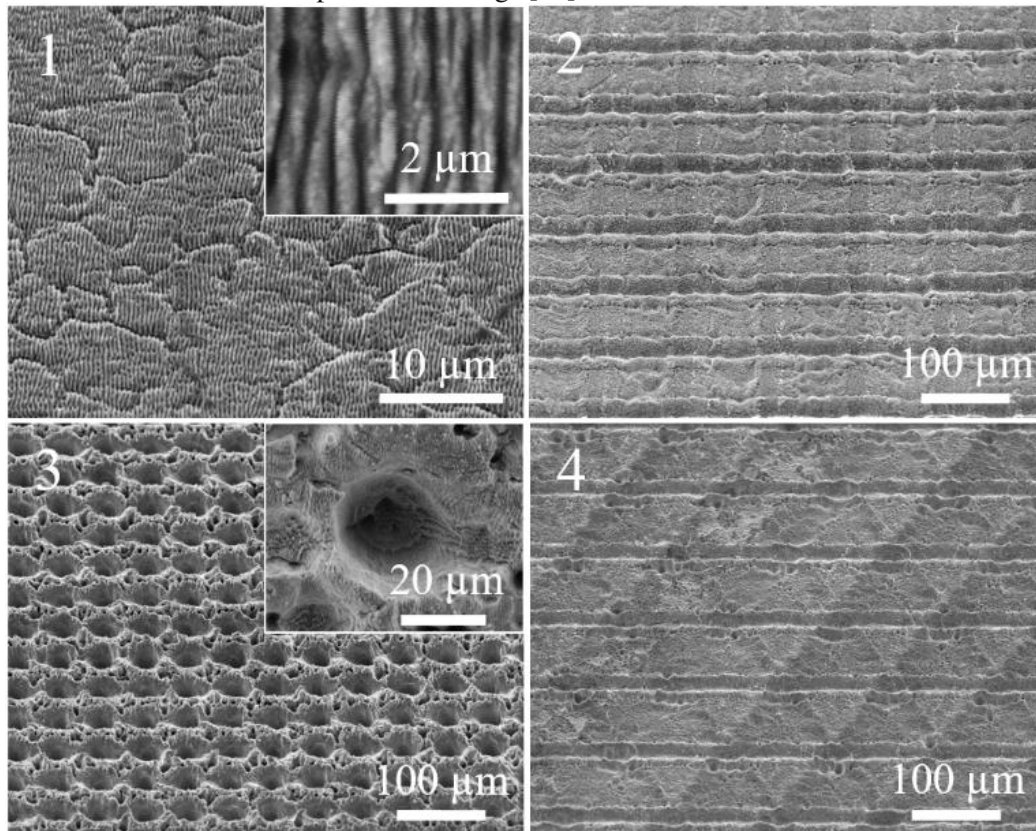


Fig. 2. SEM images: laser structures 1 – 4, taken at a 45° tilt angle (close-ups have been taken without tilt).

Wettability properties and de-icing performance

After laser processing, the samples were cleaned with filtered, de-oiled pressured air (5 μm PE-filter → 0.01 μm borosilicate aluminum filter → activated carbon filter) at 5 bar to remove residues of the laser ablation process and avoid hydrocarbon contamination. Distilled, demineralized and deionized water was used as a probe liquid for all measurements. Before and after each measurement, the samples were carefully dried with the aforementioned cleaned pressured air. To determine the wettability properties, a DataPhysics OCA25 goniometer was used. The static contact angle (SCA) measurements have been performed using 10 μl water droplets. Contact angle hysteresis (CAH) was measured with an initial drop volume of 5 μl and a maximum drop volume of 50 μl [12]. Additionally, the roll-off-angle (RoA) was determined for structures with static contact angles > 90°. After two weeks of hydrocarbon or vacuum treatment, five consecutive ice adhesion measurements have been performed, following the schedule shown in Fig. 3. We used the cuvette encased ice column method to measure the shear stress at a temperature of -30 °C [13].

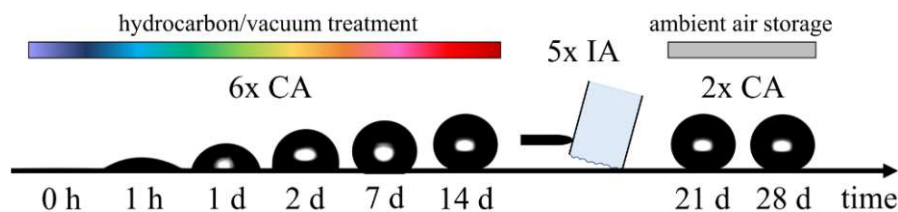


Fig. 3. Experiment schedule after laser processing; SCA – static contact angle measurement, IA – ice adhesion measurement

2.3. Hydrocarbon and vacuum treatment

Immediately after laser treatment, the samples were stored in HDPE barrels, filled with 500 ml of liquid (table 3). The barrels were sealed air-tight and reopened for each measurement cycle to take out the samples. For the

vacuum treatment we placed our sample in the vacuum chamber of a Jeol JCM-5000 scanning electron microscope, which is pumped by a turbomolecular pump, providing a pressure of better than 10^{-4} mbar in the specimen chamber.

Table 3. Tested hydrocarbon liquids and storage conditions.

Sample ID	Treatment	Storage condition
1	EuroSuper petrol RON 95	atmosphere
2	EuroSuper petrol RON 95	immersed
3	Petroleum benzine 60-95	atmosphere
4	Petroleum benzine 60-95	immersed
5	n-Hexane	atmosphere
6	n-Hexane	immersed
7	Toluene	atmosphere
8	Toluene	immersed
9	2-Propanol	atmosphere
10	2-Propanol	immersed
11	Vacuum	-
12	Air, reference	T: 20–22 °C, RH: 40–50%

3. Results and discussion

3.1. Static contact angle

Immediately after laser processing, all samples and structures showed superhydrophilic wettability. The sample immersed in EuroSuper petrol experienced a very rapid transformation to hydrophobic after only one hour of exposure. Depending on the structure type, the SCA increased to 127° for LIPSS and 161° for the micro dimple array with an average SCA of 143.9° (Fig. 4 & 5). This is an even faster transition than the sample stored in vacuum experienced, which resulted in an average SCA of 120.2° after one hour. The other samples did not show a comparable transformation (Fig. 4). Interestingly, after five consecutive ice adhesion shear test cycles, the wettability stayed on an almost constant level, which indicates a certain binding strength of the newly established surface layers.

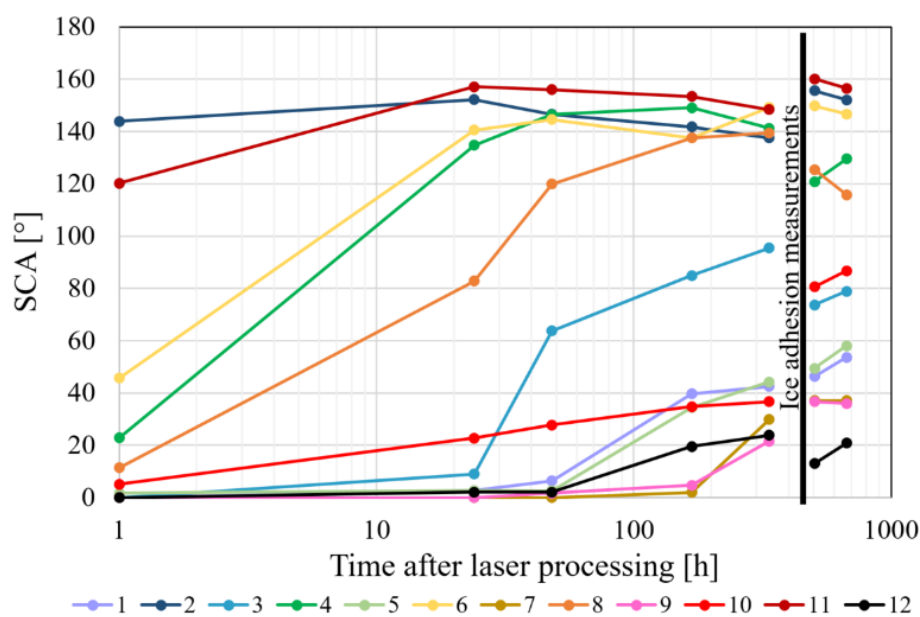


Fig. 4. Development of the static contact angle as mean values for each sample after laser processing, hydrocarbon or vacuum treatment and before/after 5 ice adhesion measurements.

The micro dimple array experienced the most significant and fastest transformation of all laser structures investigated in this study. Sample 2 and 11 both showed superhydrophobic behavior with contact angles above 160° after one hour of treatment (Fig. 5).

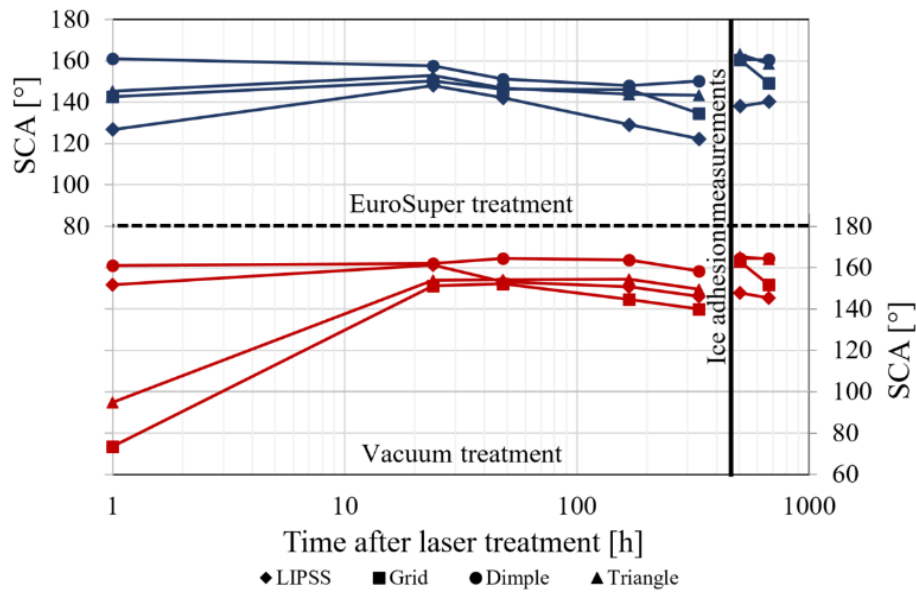


Fig. 5. Development of the static contact angle (SCA) for different surface structures after laser processing and EuroSuper petrol (above, blue) or vacuum treatment (below, red).

The reason for this accelerated reaction with the offered hydrocarbons could be connected to the surface topography – the surface area of structure 3 is about 4.4x larger than the initial planar surface (Sdr, table 2). In comparison, storage in ambient air did not trigger a change of the wetting behavior in the examined time period. The unstructured and untreated reference sample showed a SCA of $68.6 \pm 7.3^\circ$.

3.2. Contact angle hysteresis and roll-of-angle

Only a few treatments and structure types led to a measureable RoA. In most cases, the deposited 30 μl water droplet stayed pinned to the surface during the tilting movement of the sample. Both Eurosuper petrol immersion and vacuum treatment resulted in very low RoA in the range of 5° or below and showed a corresponding low contact angle hysteresis of about 10° (table 4).

Table 4. RoA and CAH of laser processed samples after 2 weeks of hydrocarbon or vacuum treatment and after 5 ice adhesion measurements.

Sample ID	Pattern type	RoA [°]	CAH [°]
2	Dimple	5.5	12.5
6	Triangle	56.1	87.4
11	Dimple	1.9	7.1

3.3. Ice adhesion

The ice adhesion shear strength of untreated stainless steel depends on the surface roughness due to the production or post-production process, e.g. 700 kPa with $R_q = 0.2 - 0.9 \mu\text{m}$ [5, 13]. In our case, the cold rolled stainless steel samples showed an ice adhesion of $820 \pm 20 \text{ kPa}$ with $R_q = 0.3 \mu\text{m}$. The hydrocarbon treatment did influence the ice adhesion very significantly but only for the immersed samples 2 and 6. Overall, LIPSS led to the lowest measured ice adhesion of $247 \pm 21 \text{ kPa}$ on the vacuum treated sample 11. Eurosuper petrol immersion could lower the ice adhesion to $409 \pm 91 \text{ kPa}$ on the grid structure of sample 2. Figure 6 shows the mean results of 5 consecutive measurements as a ratio to the laser structured reference sample 12.

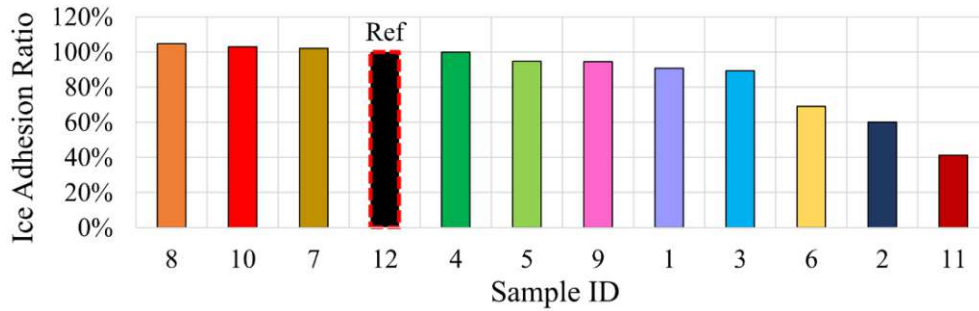


Fig. 6. Ice adhesion of laser processed, hydrocarbon or vacuum treated samples as ratio to the laser structured reference sample stored in ambient air.

The results of all ice adhesion measurements performed in this study, are presented in Fig. 7 as mean values of 5 consecutive measurements per structure and sample.

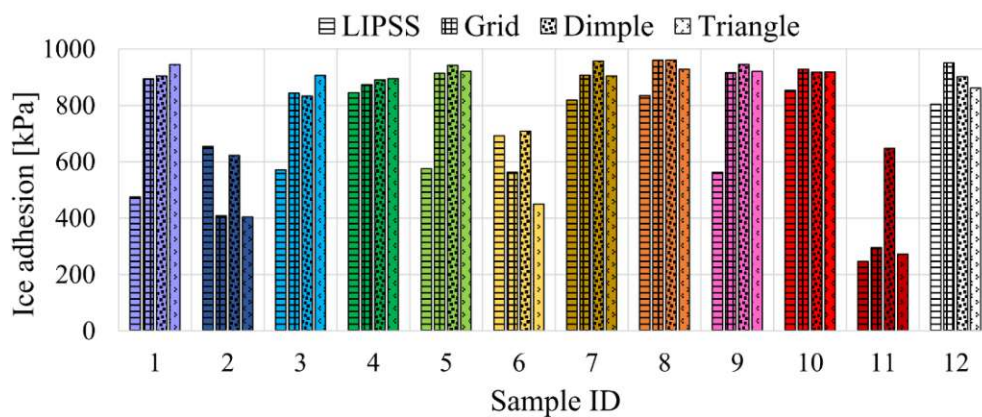


Fig. 7. Mean ice adhesion shear stresses for laser processed and hydrocarbon or vacuum treated samples and reference sample 12 for each structure type.

3.4. XPS analysis

All measurements were carried out on a SPECS XP-spectrometer equipped with a monochromatic Al-K α X-ray source (μ Focus 350) and a hemispherical WAL-150 analyzer. LIPSS and dimples together with an unstructured reference spot on sample 2, 6, 11 and 12 have been analyzed (table 5). Sample 11 showed the largest amount of C and lowest amounts of Fe, Cr and O, while samples 2 and 6 also showed an increase in C and decrease in Fe, Cr, and O when compared to the reference sample 12. The results correlate with the observed changes of the wetting and deicing behavior.

Table 5. Results of the XPS measurements; relative atomic concentrations of carbon and iron, Fe/C change when compared to the respective structure or unstructured reference area on sample 12.

Sample ID	Pattern type	C [at%]	Fe [at%]	Fe/C change [%]
2	LIPSS	44.2	9.6	-45
2	Dimple	41.1	10.2	-43
2	Reference	45.8	6.3	17
6	LIPSS	40.2	10.4	-38
6	Dimple	40.8	11.3	-38
6	Reference	50.5	5.8	8
11	LIPSS	50.0	9.1	-52
11	Dimple	49.7	8.9	-55
11	Reference	50.0	6.0	10
12	LIPSS	25.5	14.7	-
12	Dimple	24.5	15.2	-
12	Reference	55.5	5.4	-

The C1s signal can be deconvoluted into four distinct components: C-C/C-H (285.0 eV), C-O (286.3 eV), C=O (287.9 eV) and O-C=O (288.9 eV). The last three components can be described as polar while C-C/C-H can be seen as non-polar. All samples showed an increase of the non-polar component when compared to sample 12, where the increase is largest for sample 11 (Fig. 8).

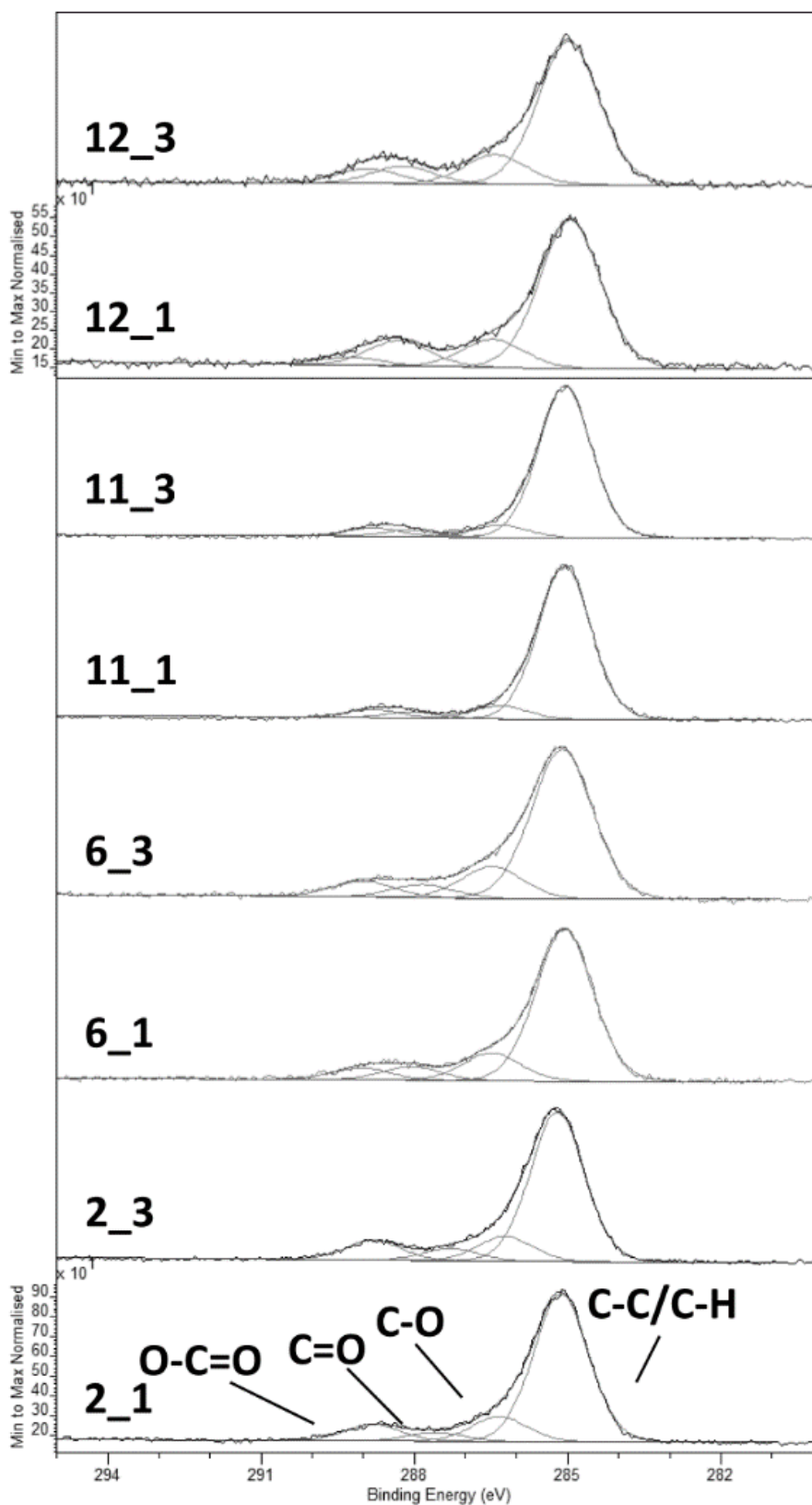


Fig. 8. C1s XPS detail spectra of samples 2, 6, 11 and 12 (structures 1 and 3). All spectra have been normalized to their strongest signals.

4. Conclusions

Hydrocarbon treatment with Eurosuper petrol provides the necessary conditions for a fast wetting state transformation from superhydrophilic to superhydrophobic after femtosecond laser processing. It also improves the de-icing performance significantly by a reduction of ice adhesion of more than 57%. To our understanding, vacuum treatment could lead to various transformation times depending on the contamination inside the vacuum chamber and the pressure. In our experiment, it led to a slower transformation but in the end slightly better water-repellent properties and lower ice adhesion than hydrocarbon treatment. Further analysis must be performed to acquire information on the mechanisms behind the observed behavior as well as the stability of the formed surface layers.

Acknowledgements

This project has received funding from the Austrian climate and energy funds with FFG project number 871733. The authors acknowledge the Analytical Instrumentation Center (TU Wien) for their contribution to XPS analysis.

References

- [1] Sciancalepore C, Gemini L, Romoli L, Bondioli F. Study of the wettability behavior of stainless steel surfaces after ultrafast laser texturing. *Surface and Coatings Technology*, Bd. 352, p. 370–377, 2018.
- [2] Jagdheesh R, Pathiraj B, Karatay E, Römer GRBE, in't Veld AJH. Laser-Induced Nanoscale Superhydrophobic Structures on Metal Surfaces. *Langmuir*, Bd. 27, p. 8464–8469, 2011.
- [3] Vercillo V, Tonnicchia S, Romano JM, García-Girón A, Aguilar-Morales AI, Alamri S, Dimov SS, Kunze T, Lasagni AF, Bonaccorso E. Design Rules for Laser-Treated Icephobic Metallic Surfaces for Aeronautic Applications. *Adv. Funct. Mater.*, Bd. 30, p. 1910268, 2020.
- [4] Yang Z, Liu X, Tian Y. Insights into the wettability transition of nanosecond laser ablated surface under ambient air exposure. *J. Colloid Interface Sci.*, Bd. 533, p. 268–277, 2019.
- [5] Fürbacher R, Liedl G. Investigations on the wetting and deicing behavior of laser treated hydrophobic steel surfaces. *Laser-based Micro- and Nanoprocessing XV*, 2021.
- [6] Ngo CV, Chun DM. Fast wettability transition from hydrophilic to superhydrophobic laser-textured stainless steel surfaces under low-temperature annealing. *Appl. Surf. Sci.*, Bd. 409, p. 232–240, 2017.
- [7] Hauschwitz P, Jagdheesh R, Rostohar D, Brajer J, Kopeček J, Jiříček P, Houdková J, Mocek T. Hydrophilic to ultrahydrophobic transition of Al 7075 by affordable ns fiber laser and vacuum processing. *Appl. Surf. Sci.*, Bd. 505, p. 144523, 2020.
- [8] Wanzenboeck HD, Roediger P, Hochleitner G, Bertagnolli E, Buehler W. Novel method for cleaning a vacuum chamber from hydrocarbon contamination. *J. Vac. Sci. Technol. A: Vacuum, Surfaces, and Films*, Bd. 28, p. 1413–1420, 2010.
- [9] Chen J, Liu J, He M, Li K, Cui D, Zhang Q, Zeng X, Zhang Y, Wang J, Song Y. Superhydrophobic surfaces cannot reduce ice adhesion. *Appl. Phys. Lett.*, Bd. 101, p. 111603, 2012.
- [10] Fortin G, Perron J. Ice Adhesion Models to Predict Shear Stress at Shedding. *J. Adhes. Sci. Technol.*, Bd. 26, p. 523–553, 2012.
- [11] Fuerbacher R, Liedl G, Murzin S. P. Experimental study of spatial frequency transition of laser induced periodic surface structures. *J. Phys. Conf. Ser.*, 1745, 012017, 2021.
- [12] Korhonen JT, Huhtamäki T, Ikkala O, Ras RHA. Reliable Measurement of the Receding Contact Angle. *Langmuir*, Bd. 29, p. 3858–3863, 2013.
- [13] Meuler AJ, Smith JD, Varanasi KK, Mabry JM, McKinley GH, Cohen RE. Relationships between Water Wettability and Ice Adhesion. *ACS Appl. Mater. Interfaces*, Bd. 2, p. 3100–3110, 2010.

2.5. Icing Wind Tunnel and Erosion Field Tests of Superhydrophobic Surfaces Caused by Femtosecond Laser Processing

Published by: MDPI (2024)

Journal: Wind 2024, 4, 155-171

DOI: <https://doi.org/10.3390/wind4020008>

Roland Fürbacher*, Gerhard Liedl, Gabriel Grünsteidl, Andreas Otto

Institute of Production Engineering and Photonic Technologies, TU Wien,
Getreidemarkt 9, Vienna 1060, Austria

* Correspondence: roland.fuerbacher@tuwien.ac.at

Abstract: Ice accumulation on lift-generating surfaces, such as rotor blades or wings, degrades aerodynamic performance and increases various risks. Active measures to counteract surface icing are energy-consuming and should be replaced by passive anti-icing surfaces. Two major categories of surface treatments—coating and structuring—already show promising results in the laboratory, but none fulfill the current industry requirements for performance and durability. In this paper, we show how femtosecond laser structuring of stainless steel (1.4301) combined with a hydrocarbon surface treatment or a vacuum treatment leads to superhydrophobic properties. The anti-ice performance was investigated in an icing wind tunnel under glaze ice conditions. Therefore, flexible steel foils were laser-structured, wettability treated and attached to NACA 0012 air foil sections. In the icing wind tunnel, hydrocarbon treated surfaces showed a 50 s ice build-up delay on the leading edge as well as a smoother ice surface compared to the reference. To demonstrate the erosion resistance of these surfaces, long-term field tests on a small-scale wind turbine were performed under alpine operating conditions. The results showed only minor erosion wear of micro- and nano-structures after a period of six winter months.

Keywords: wind turbine icing; airfoil icing; surface modification; femtosecond laser structuring; superhydrophobic surface; icephobic surface; hydrocarbon treatment; vacuum treatment; erosion resistance

1. Introduction

Surface icing is crucial in various technical applications, particularly when surfaces are exposed/subjected to humid and cold air conditions [1–4]. Depending on the type of application and the accompanied risks, different strategies have been developed to address the problem of icing. Modern commercial airplanes have ice protection systems (IPS) that allow an all-weather flying capability. Nevertheless, active measures like thermal, electro-magnetic or pneumatic deicing systems require a lot of energy and are therefore restricted to cyclic operation [5,6]. In general aviation, the TKS-System (Tecalemit-Kilfrost-Sheepbridge Stokes) can prevent icing by pumping a fluid mixture through holes in the leading edge, creating a thin film. Like the fluid, which is used to deice commercial aircraft on the ground, it consists mainly of glycol alcohol [7]. Even though glycol ethers are not found to be persistent in the environment, not bio-accumulative and non-toxic, extensive use (e.g., on an airport in winter) could lead to problematic local concentrations [8,9]. In most cases, anti-icing and deicing chemicals contain 10–20% additives, including corrosion and rust inhibitors, thickening agents and surfactants which have a significant chronic toxicity [10]. Furthermore, the use of such chemicals is an additional cost factor for the industry.

Regarding wind power plants, icing of wind turbine rotor blades leads to a reduction in lift force and an increased drag force which causes a loss of production efficiency of up to 30% due to disturbed aerodynamics [11,12]. Furthermore, ice accumulation represents an increased health and safety risk due to ice shedding and ice throw in the turbines' vicinity [13,14]. Experiments conducted on a 300 kW wind turbine demonstrated that icing rates of > 80 mm/h are possible and that the ice thickness increases towards the blade tip [15]. As countermeasures, thermal IPS are currently used almost exclusively,

which are based on the heating of relevant rotor blade zones by electrically operated heating elements or a warm airflow circulating in the blade. The power requirement of electrical systems is 6–12% of the wind turbine output [16], and that of systems working with warm airflow is 10–15% [17]. In weather conditions that are particularly negative for operation, the power losses can also increase further to 80% [18] until it comes to the technically necessary shutdown [19]. Besides the efficiency loss, active heating of the rotor blades has to be monitored to not weaken the composite material over time [6].

Both aviation and wind energy would profit from passive icephobic surfaces, which reduce or delay ice accumulation and stimulate deicing by modification of surface topography and chemistry. Special coatings can be used as passive IPS, which are based on a reduction of the surface energy to achieve superhydrophobic and icephobic behavior [20]. Most polymer coatings are prone to erosion, which limits service life and thus prevents industrial use [6,21]. Metallic coatings show the potential to be erosion resistant but need further development to be strongly icephobic [22]. Laser structuring of surfaces is an alternative method to achieve superhydrophobic wetting behavior, triggered by creating air pockets in the solid/water interface and thereby forcing an incomplete wetting state (Cassie–Baxter), and/or through chemical modification of the material induced by the laser process itself [23]. Vercillo et al. [24] investigated the correlation between laser patterns, the resulting wettability and ice adhesion but used a chemical fluorinated solvent as a superhydrophobic and anti-ice coating. The results showed a direct correlation between the surface roughness and the ice adhesion, although all samples were superhydrophobic after dip coating. These findings are consistent with the results of our previous work, where shallow laser induced periodic surface structures (LIPSS) led to the lowest mechanical locking of the ice at the interface [25].

Under ambient air conditions, femtosecond laser processing induces a chemical reaction due to the laser's energy deposition [25,26]. This leads to a material-dependent oxidation process of the top surface layer, which adsorbs organic hydrocarbons from the air and thereby changes the overall chemical polarity from polar (hydrophilic) to non-polar (hydrophobic) [27]. This process is strongly dependent on the storage conditions (e.g., the chemical composition of the sample surrounding air) and can take from days to months [28]. Ways to shorten the wetting transformation time include heating [29] and vacuum treatment [30]. Our previous work presented a novel approach to significantly shorten the wetting transformation time by a hydrocarbon chemical treatment and compared it to vacuum treatment [31]. The best results were achieved by storing the laser-processed samples immersed in petrol. Depending on the laser-generated micro- or nano-structure, the ice adhesion could be reduced by 50% with petrol immersion and by 70% with vacuum treatment.

Nevertheless, it has to be considered that surface structures increase the roughness and could thereby alter the aerodynamics of a lift-generating body. The surface roughness is often characterized by the sand-grain roughness k , corresponding to the height of spherical particles attached to a surface like on a sandpaper [32]. Since real rough surfaces are more complex, the equivalent sand-grain roughness k_s can be estimated using different approaches. One widely used method for calculating k_s was developed by Flack et al. for $s_k > 0$ [33]:

$$k_s \approx 4.43 \cdot k_{RMS} \cdot (1 + s_k)^{1.37} \quad (1)$$

and for $s_k < 0$ [34]:

$$k_s \approx 2.73 \cdot k_{RMS} \cdot (2 + s_k)^{-0.45} \quad (2)$$

where k_{RMS} is the root-mean-square roughness height, and s_k is the skewness. A positive skewness indicates that the height distribution of the roughness is shifted below the mean plane (e.g., a turned surface), while a negative skewness indicates a shift above the mean plane (e.g., a pitted bearing surface) [35].

To quantify the effect of a rough surface on aerodynamics, Prikhod'ko et al. [36] tested a standard NACA 0012 airfoil with a modified rough surface ($k_s = 200 \mu\text{m}$) and measured a 7% decrease in maximum lift force and a twofold increase in drag when compared to a conventional smooth surface. Jung et al. [37] investigated the effect of wind turbine rotor blade roughness on its aerodynamic performance by simulating different wind speed scenarios. They applied an equivalent sand grain roughness height chord ratio k_s/c of 1.9×10^{-3} , where c is the chord length of the airfoil, to an S809 airfoil, which resulted in a performance decrease at 7 m/s but an increase at 10 m/s with a minor effect at higher wind speeds, which contradicts previous findings by Bouhelal et al. [38]. Based on 3D computational fluid dynamics (CFD) simulations, Bouhelal et al. concluded that roughness heights $k_s > 0.5 \mu\text{m}$ decreased the performance by up to 35% at wind speeds $> 10 \text{ m/s}$, but also found a wind speed dependence of the critical roughness value. It is commonly assumed that structured surfaces

increase the friction and heat flux on the surface of an airfoil, thereby promoting ice growth which causes a further increase in surface roughness. Tagawa et al. [39] performed CFD airflow simulations for NACA 0012 airfoils considering the surface roughness due to ice accretion. The results showed that roughness effects become significant for equivalent sand-grain roughness heights $k_s/c > 1 \times 10^{-4}$, rapidly decreasing the maximum lift coefficient [39]. Prikhod'ko et al. [36] performed experiments with different leading edge shapes to simulate ice accretion and found that the formation of horn-like ice outgrowths causes a severe deterioration in the aerodynamic characteristics of the wing and thereby decreases the maximum lift force (down to 50%) and increases aerodynamic drag (by several times).

Besides the performance, a high erosion resistance is another critical property for future industrial applications of superhydrophobic and icephobic surfaces. In wind energy, contamination and erosion of blades (coatings) reduces the annual energy output of a turbine by 2–3.7% [40]. Sand, water and hail impacting the blades at high velocities cause the formation of pits, removal of coating and delamination of the underlying fiber-reinforced material. Most commercial anti-ice surfaces comprise thin polymer films which are prone to erosion. To address this limitation, both the scientific community and industry are actively developing erosion-resistant superhydrophobic and icephobic surfaces [41].

In this work, we expand our previous investigations on femtosecond laser surface processing and look at the performance and durability of superhydrophobic and icephobic surface layers formed by hydrocarbon and vacuum treatment. This study compares treatments and the influence of the laser-generated structure type on the wettability and the anti-ice performance. The generated surfaces were tested in the laboratory and the field. Wind tunnel tests were carried out to investigate the impact of these measures on the ice-accumulation process. The durability of the structures was evaluated during a six-month test campaign, where samples were placed on the rotor blades of a small-scale wind turbine located at an exposed mountain ridge.

2. Materials and Methods

2.1. Material

Cold-rolled stainless steel (1.4301/AISI 304) (Fixmetall Brunn am Gebirge, Austria) was used as substrate material for all experiments. The substrates were not polished before laser processing to keep their initial roughness from the cold rolling process. The thickness was 0.05 mm for wind tunnel and field tests, where flexible sheets were needed to fit the airfoil shapes. Before undergoing laser processing, the substrates were cleaned with acetone and air-dried.

2.2. Laser Processing

The samples were structured using a femtosecond laser system Femtopower Compact Pro (Spectra-Physics, Vienna, Austria) consisting of a Ti:Sapphire oscillator and a multi-pass Ti:Sapphire amplifier, which emits broadband 30 fs laser pulses at a rate of 1 kHz (Figure 1). Laser pulses can carry a maximum pulse energy of 0.8 mJ at 800 nm central wavelength and a bandwidth of 40 nm. Due to its internal setup, the output radiation is linearly polarized, which is required to form channel-like LIPSS. A variable attenuator was used to adjust the laser fluence on the specimens' surface. The laser beam was focused by a plano-convex spherical lens with a focal length of 100 mm. During all experiments, we worked with a Gaussian intensity distribution. Based on our previous experiments, we selected the same four different laser structure types for further testing (Figure 2). LIPSS were generated off-focus by overlapping linear tracks, grid and triangle structures were created by intersecting tracks at 90° or 60°, respectively. Micro dimple arrays were generated by repetitive static laser ablation.

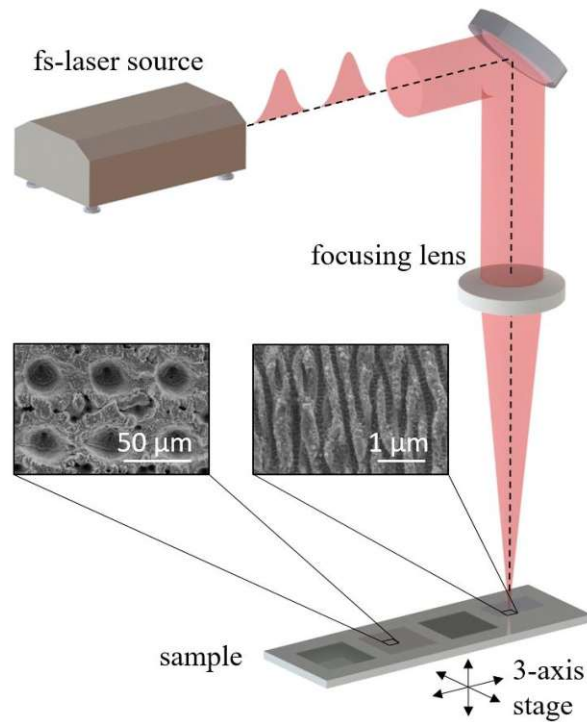


Figure 1. Schematic depiction of the femtosecond laser machining setup.

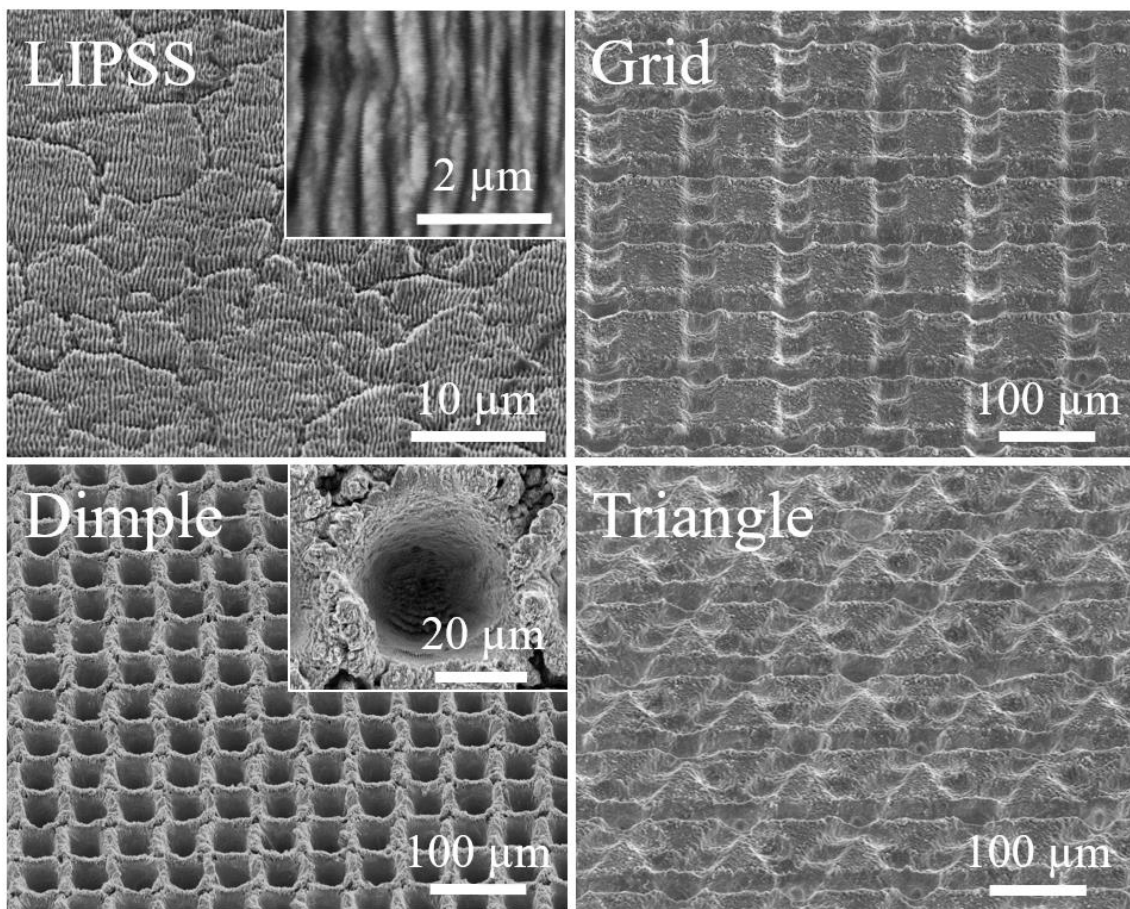


Figure 2. SEM images: laser-generated structure types, taken at a 45° tilt angle (close-ups were taken without tilt).

Samples were irradiated perpendicular to the surface (angle of incidence 0°) in a controlled environment at $21 \text{ °C} \pm 0.5 \text{ °C}$ and a humidity of $45 \pm 5\%$ in air without the use of inert shielding gas. With the constant pulse repetition rate of 1 kHz, the number of laser pulses applied on the same surface

area was adjusted by the feed rate of the 3-axis motorized translation stage. The machining parameters are summarized in Table 1.

Table 1. Laser machining parameters and post-laser-treatments of the samples which were tested in the icing wind tunnel (IWT—Icing Wind Tunnel; E—Erosion).

Sample ID	Structure Type	Wettability Treatment	Treatment Duration (h)	Laser Fluence (J/cm ²)	Spot Diameter (μm)	Hatch (μm)	Number of Laser Pulses
IWT#1	LIPSS	Vacuum	4	0.6	200	150	25
IWT#2	Grid	Vacuum	4	15	50	100	25
IWT#3	Dimple	Vacuum	4	20	50	50	40
IWT#4	Triangle	Vacuum	4	10	50	100	25
IWT#5	LIPSS	Petrol, immersion	4	0.6	200	150	25
IWT#6	Grid	Petrol, immersion	4	15	50	100	25
IWT#7	Dimple	Petrol, immersion	4	20	50	50	40
IWT#8	Triangle	Petrol, immersion	4	10	50	100	25
E#1	LIPSS	-	-	0.6	200	150	25
E#2	Grid	-	-	15	50	100	25
E#3	Dimple	-	-	20	50	50	20
E#4	Triangle	-	-	15	50	100	25

2.3. Surface Structures

The geometric surface properties of the laser-processed samples were obtained with a Bruker Alicona Infinite Focus 3D surface measurement system, which uses the method of focus variation to retrieve surface topography information. For scanning electron microscopy (SEM) imaging, a JCM-5000 instrument (Jeol, Akishima, Japan) was used. Figure 2 shows the four structure types tested in the following experiments.

2.4. Wettability Acceleration Treatment

A contact angle goniometer OCA25 (DataPhysics, Filderstadt, Germany) with a 0.4 mm blunt tip cannula was used to evaluate the wettability properties of the laser treated samples. We used the sessile drop method with a polynomial fitting to obtain the static contact angles (SCA) utilizing a water drop volume of 10 μ L.

Immediately after femtosecond laser processing, metal surfaces tend to be superhydrophilic and evolve to a hydrophobic state over a period of several days to weeks. To accelerate the wetting transformation time, the samples were placed in either a vacuum chamber or immersed in EuroSuper Petrol (RON 95) (OMV, Vienna, Austria) inside a sealed HDPE barrel (Table 1). We used the same SEM instrument (Jeol JCM-5000) for imaging and vacuum treatment, but we turned off the electron beam during the latter. Its turbomolecular pump provided a pressure of less than 10^{-4} mbar in the specimen chamber. The duration of the treatment was chosen based on our previous work, where the focus was on the wetting transformation time of laser-structured samples stored in different media. For this reason, the samples were treated for 2 weeks (336 h), even though, vacuum and petrol treatment showed a faster transformation. However, considering that only short transformation times are relevant for industrial applications, we reduced the treatment duration to 4 h in this work. The field tests were primarily focused on examining the mechanical erosion of the laser-generated structures in harsh environmental conditions, so no wettability treatment was applied.

2.5. Icing Wind Tunnel

The performance of the laser-processed and hydrocarbon/vacuum-treated samples under dynamic icing conditions was tested in the FH JOANNEUM small-scale icing wind tunnel (FHJIWT) (FH JOANNEUM, Graz, Austria) [42]. The FHJIWT is a calibrated closed-loop atmospheric wind tunnel of Göttingen configuration and can simulate in-flight icing conditions. For the experiments, laser-processed stainless steel foils were taped onto NACA 0012 airfoil segments (downscaled to 20%) with a nominal chord length of $c = 200$ mm made of extruded polystyrene (XPS) covered with a ply of fiberglass (Figure 3). As the investigation was focused on the icing of the leading edge, the air foil sections were truncated. The influence of possible vibrations caused by a turbulent wake of the blunt tip trailing edge was assumed to be neglectable based on the low wind speed and neutral angle of attack [43,44].

The 1.4301 metal sheets had a length of 150 mm and a width of 50 mm of which 120×45 mm were structured by the femtosecond laser with the machining parameters summarized in Table 1. Each sample consisted of one laser processed stainless steel foil placed side by side with an untreated reference foil (Figure 3). No spanwise or chordwise parting strip was used during the experiments. The icing tests were conducted in a representative glaze ice condition with a neutral angle of attack, $\text{AoA} = 0^\circ$ (Table 2).

Table 2. Icing conditions used in the wind tunnel experiments.

Ice Type	Temperature ($^\circ\text{C}$)	Air Speed (m/s)	MVD* (μm)	LWC** (gm^{-3}) @ -10°C , 15 m/s	Icing Cycle (s)
Glaze	-10	25	42	5.1	180

* MVD - median volume diameter. ** LWC - liquid water content.

The initial wetting and ice growth were monitored and recorded by a camera for 180 s, positioned vertically on top of the test section. This view from above allowed us to assess both the initial wetting process as well as the ability of the surfaces to repel impinging water droplets and support runback along the upper airfoil surface. Prior to each run, the airfoils were mounted in the test section and acclimatized for 10 min.

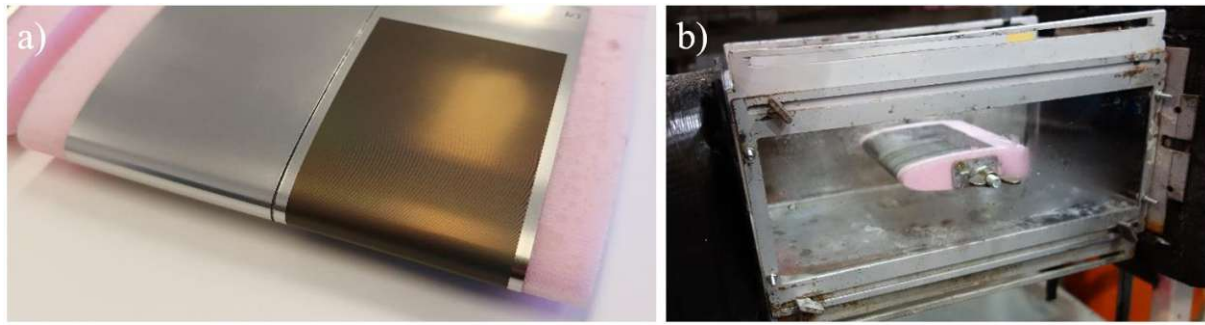


Figure 3. Airfoil section: (a) prepared sample IWT#1 with taped laser processed (right) and reference steel foil (left), (b) test section in the FHJIWT.

To obtain more information on the ice accumulation after 180 s, the airfoil sections were removed from the test chamber and scanned with a portable 3D laser measurement system consisting of a Hexagon Absolute Arm and a RS6 laser-scanning head with a system accuracy of 48 μm . Therefore, a thin film of titanium-dioxide powder was applied to the accumulated ice to enhance the reflection of the laser light on the ice shape.

2.6. Field Tests

The erosion resistance of the laser-generated structures was tested using a small-scale wind turbine stationed on the Pretul mountain ridge in the Austrian Alps at an elevation of 1600 m. The wind turbine (superwind 1250) (superwind, Brühl, Germany) had a diameter of 2.4 m and a maximum wingtip speed of 75 m/s at 600 rpm. On each of the three wings, a small laser-structured stainless steel foil (1.4301) with a thickness of 50 μm was attached with an adhesive (Figure 4).

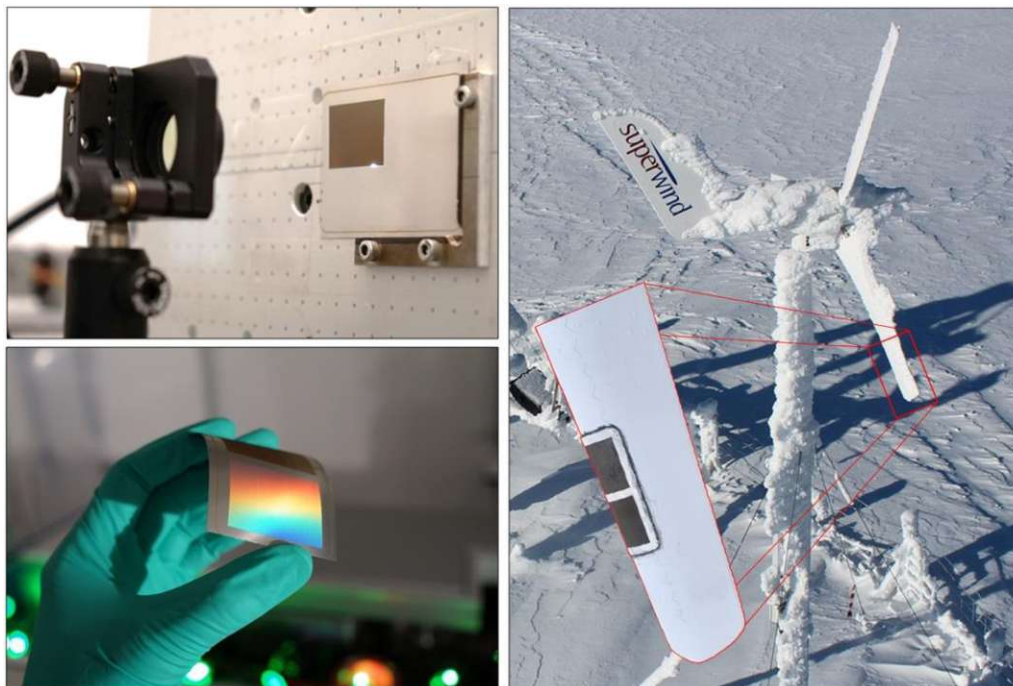


Figure 4. Femtosecond laser structuring process (top left), structured metal foil (bottom left); dynamic erosion field test setup with laser-structured stainless steel foils attached to rotor blades of a small-scale wind turbine (right).

The samples were prepared with laser machining parameters summarized in Table 1 (E#1–E#4). Environmental conditions were continuously measured and recorded over the experimental period of 6 months using an Eologix sensor (eologix sensor technology, Graz, Austria) (Figure 5). For further observation, a camera was installed to monitor the general state of the wind turbine (Figure 4). After the experiment, the wind turbine was dismantled and the relevant rotor blade sections were cut out for 3D surface characterization.

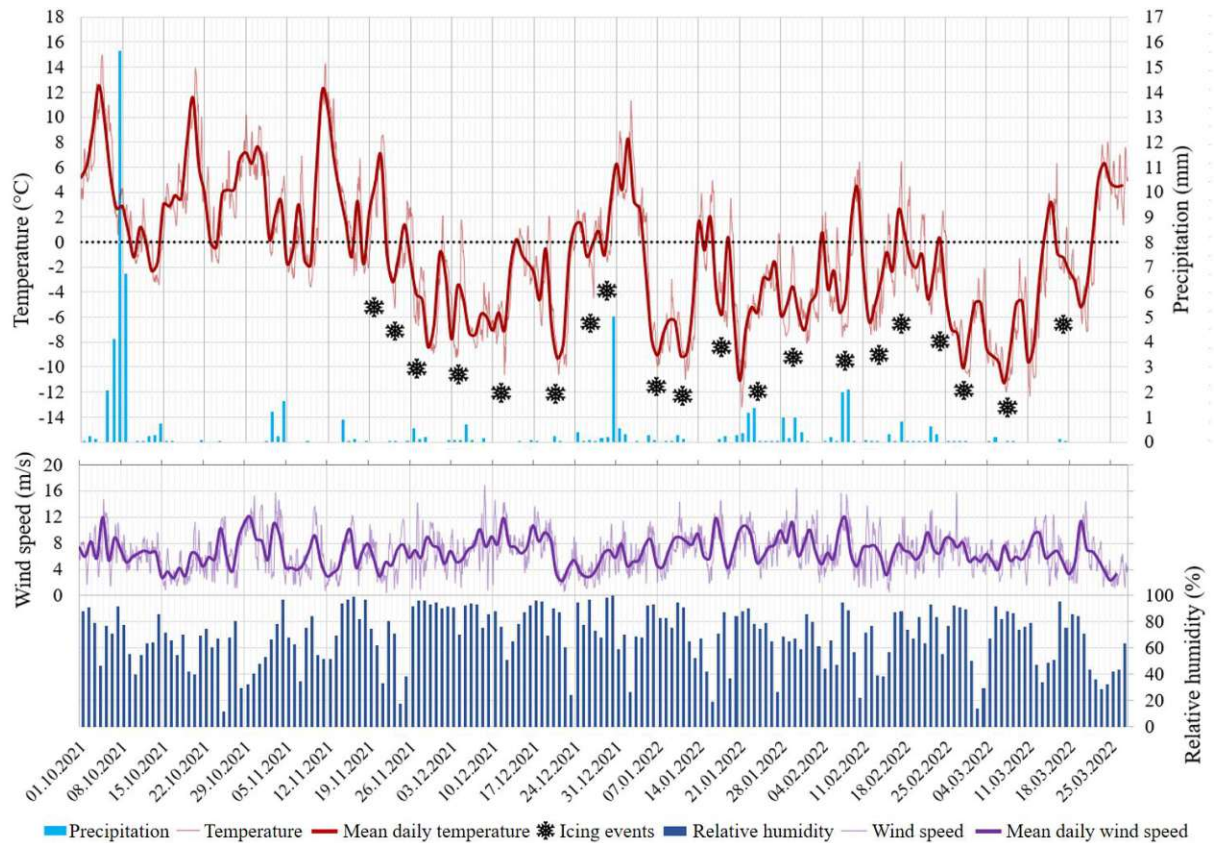


Figure 5. Environmental conditions during the dynamic erosion field test; Pretul mountain ridge at 1600 m elevation.

3. Results and Discussion

3.1. Icing Wind Tunnel

After the hydrocarbon/vacuum-treatment, all laser-structured flexible stainless steel samples showed superhydrophobic behavior (Table 3). By creating a rough surface, we tried to favor the Cassie–Baxter wetting mode, where vapor is “trapped” beneath the water fraction in the interface, over the Wenzel wetting mode, where the whole surface beneath the liquid is wetted, and thereby increase the hydrophobicity. Milne et al. [23] describe how the Cassie–Baxter equation is used to calculate the contact angle of a liquid on a rough surface and how to handle dual-scale rough surfaces, as produced by the laser ablation process. The icing wind tunnel performance (IWT performance) was evaluated visually by examining the wetting/icing videos taken during the experiment. Since the aerodynamic effect of the different laser structures applied to the surfaces could not be measured in this configuration, we focused our examination on the surfaces’ ability to repel incoming water droplets and support runback. Furthermore, we visually evaluated the initial icing process, the resulting ice shape and the ice roughness on the leading edge.

Table 3. Wetting behavior of the stainless steel samples, before/after wind tunnel tests and anti-ice performance; delay time until ice beads occur on the leading edge; “+”: more effective than reference surface; “~”: similar to the reference surface; “-”: less effective than reference sample.

Sample ID	Structure Type	Wettability Treatment	SCA before IWT Tests (°)	SCA after IWT Tests (°)	IWT Performance		
					Initial Water Runback	Delay Time (s)	Ice Accumulation after 180 s
IWT#1	LIPSS	Vacuum	151.3 ± 0.9	101.9 ± 16.8	~	0	-
IWT#2	Grid	Vacuum	157.0 ± 2.5	78.2 ± 6.3	~	0	-
IWT#3	Dimple	Vacuum	142.7 ± 4.7	61.9 ± 6.1	~	0	-
IWT#4	Triangle	Vacuum	158.7 ± 1.6	109.8 ± 7.9	~	0	-
IWT#5	LIPSS	Petrol immersion	131.9 ± 4.2	132.4 ± 14.3	+	0	-
IWT#6	Grid	Petrol immersion	148.5 ± 6.3	93.2 ± 2.3	+	50	-
IWT#7	Dimple	Petrol immersion	153.9 ± 2.3	84.0 ± 17.7	+	50	-
IWT#8	Triangle	Petrol immersion	144.2 ± 3.6	72.1 ± 20.2	+	50	-
Reference	-	-	94.2 ± 5.1	83.3 ± 12.6			

To highlight critical events like water runback after droplet impingement and the ice accretion phase, selected image sections of the recorded videos have been arranged, shown in Figure 6. The full videos are available as Supplementary Materials to this publication (Video S1–Video S8).

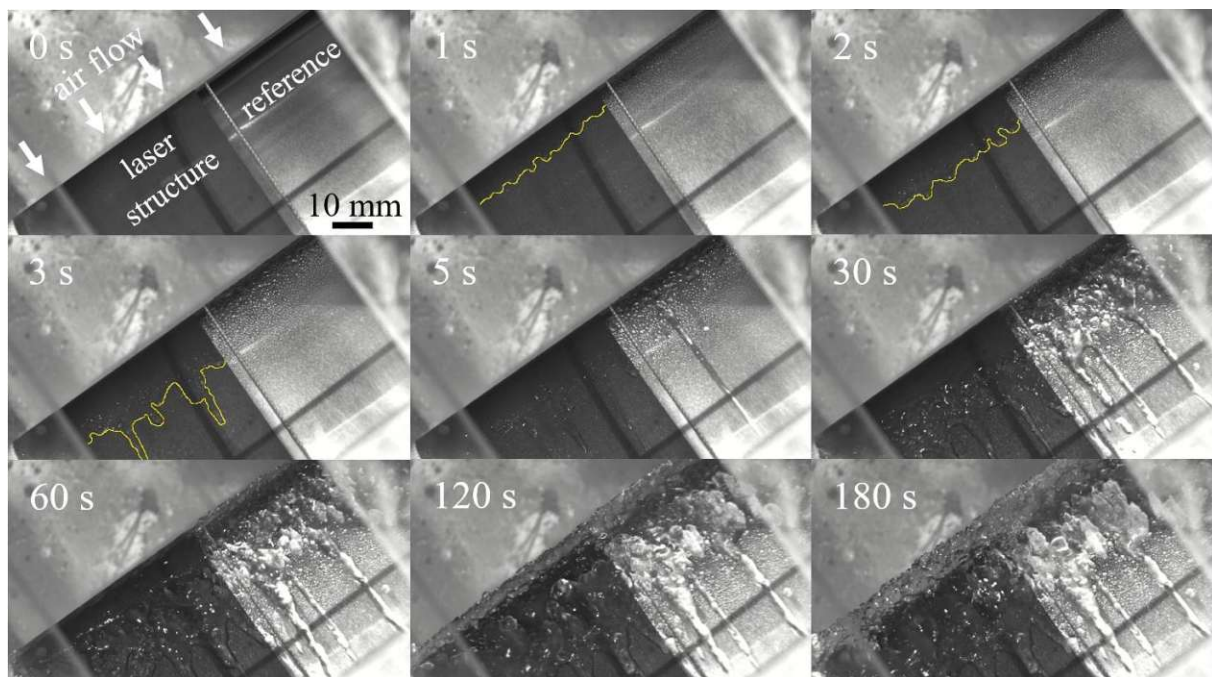


Figure 6. Top view of sample IWT#6—laser-generated grid structure with Eurosuper Petrol treatment (airfoil position: **left**), reference foil (airfoil position: **right**). Runback of arriving water droplets, waterfront highlighted by the yellow line (1 s–3 s), delayed ice bead buildup on the structured sample (30 s, 60 s).

Until the first ice layer formed on the surface, water was repelled more efficiently off the laser-structured and petrol-treated surfaces than vacuum-treated and reference surfaces. Samples IWT#6, IWT#7 and IWT#8 showed a smoother initial ice shape than the references (Figure 7). As the ice formation advanced, the growth of ice beads was initiated on the reference sections, starting at the airfoils upper surface and evolving towards the leading edge. In contrast, the leading edge sections of the structured samples remained smooth and showed less ice thickness.

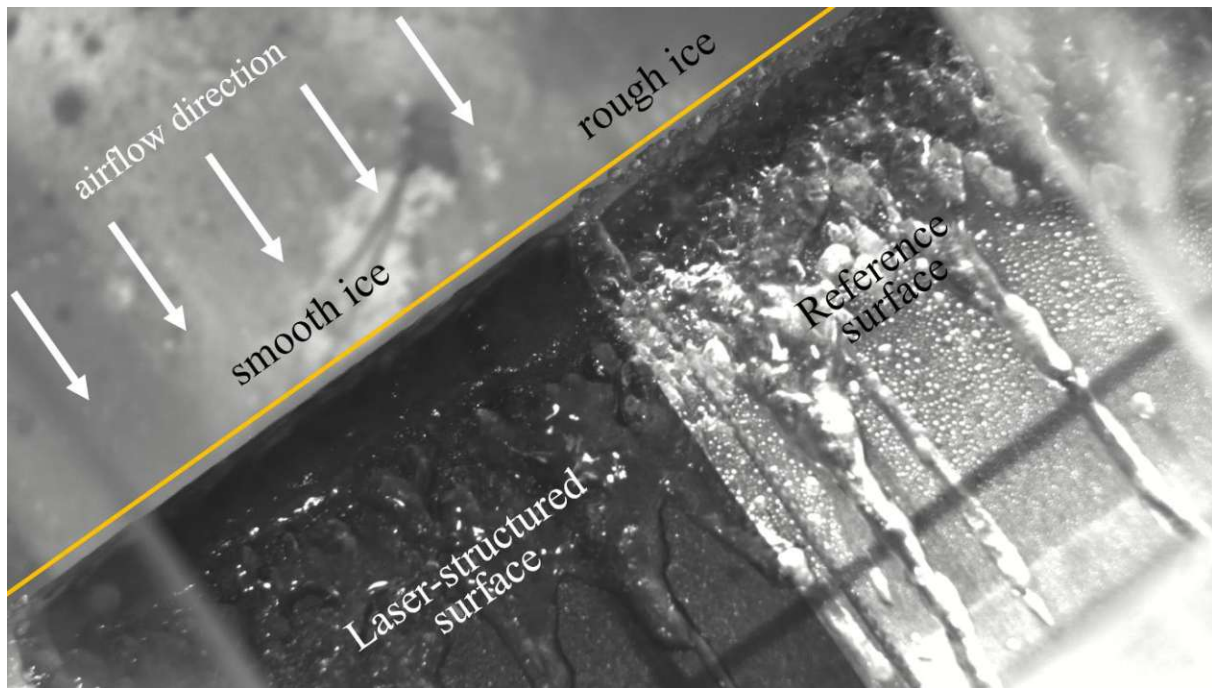


Figure 7. Top view of sample IWT#6 after 60 s, laser-structured sample (**left**) shows a smooth ice surface at the leading edge, while the same section on the reference surface (**right**) is already rough.

Ice beads increase the leading edge roughness and induce a local laminar-turbulent flow transition [23]. Beads grow partially frozen and partially liquid until a certain height is reached, which depends on the air speed, AoA, LWC, MWD and temperature [45]. Subsequently, the liquid part runs back and fills the gaps between the following beads, and the excess liquid drains away as runback water. In the case of the petrol immersed samples IWT#6, IWT#7 and IWT#8, the formation of beads was delayed compared to the reference steel foil (Figure 7). During this delay, the surface remained smooth, which positively affected the aerodynamics of the airfoil. Experimental investigations performed with single UAV rotor blades in Appendix C icing conditions [46] have shown that, even a short icing encounter of one to two minutes can result in critical ice accretion [47]. A similar result was observed for a full-scale multirotor UAV in [48], where significant amounts of ice accreted on the rotor blades within minutes. The observed delay in ice bead formation shown in this study can extend the time a UAV has to leave the critical icing condition or land safely.

For our calculations of the equivalent sand-grain roughness based on the method of Flack et al. [24,25] (Equations (1) and (2)), we decided to use the area root-mean-square height Sq instead of the line-based Rq and the same area equivalent Ssk for the skewness (Table 4).

Table 4. Measured roughness parameters of the samples tested in the IWT; equivalent sand-grain roughness k_s and chord length ratio k_s/c .

Structure Type	Sq (nm)	Ssk	k_s (μm)	k_s/c
LIPSS	82.2	0.18	0.46	2.28×10^{-6}
Grid	1816.4	-1.39	6.19	3.10×10^{-5}
Dimple	3190.6	0.07	15.51	7.75×10^{-5}
Triangle	2065.7	-1.28	6.54	3.27×10^{-5}

According to the results and conclusions of Prikhod'ko et al. [36], our laser-generated surface structures correspond to a smooth surface with an insignificant contribution to lift coefficient reduction, although the dimple structures showed a distinct micro-roughness. Based on that, no significant deterioration of aerodynamic performance was expected during our experiments since the highest equivalent sand-grain roughness that was tested resulted from dimple structures with $k_s = 15.5 \mu\text{m}$. Contrary to the findings of Prikhod'ko et al. [36], Bouhelal et al. [38] concluded that a roughness height above $k_s = 0.5 \mu\text{m}$ leads to a deterioration of the aerodynamics of an airfoil at moderate wind speeds. Since there is a significant discrepancy between those results for the critical roughness heights, reaching from $0.5 \mu\text{m}$ to $200 \mu\text{m}$, further work has to be carried out to evaluate the effect of the increased roughness of laser-structured surfaces on aerodynamics.

During the 180 s lasting icing cycle, a thick glaze ice layer built up on the leading edge, showing a horn-type ice shape (Figure 8). After the wind tunnel tests, the samples showed a significantly reduced SCA (Table 3). This phenomenon can be explained by the use of titanium-dioxide powder, which accumulated in the structures' roughness, thereby causing a transition from a Cassie–Baxter to a Wenzel wetting state. Attempts to remove the powder completely after the 3D ice scanning procedure failed. However, LIPSS nano-structures (IWT#1, IWT#5) were not affected similarly due to their shallow nature, resulting in a higher SCA.

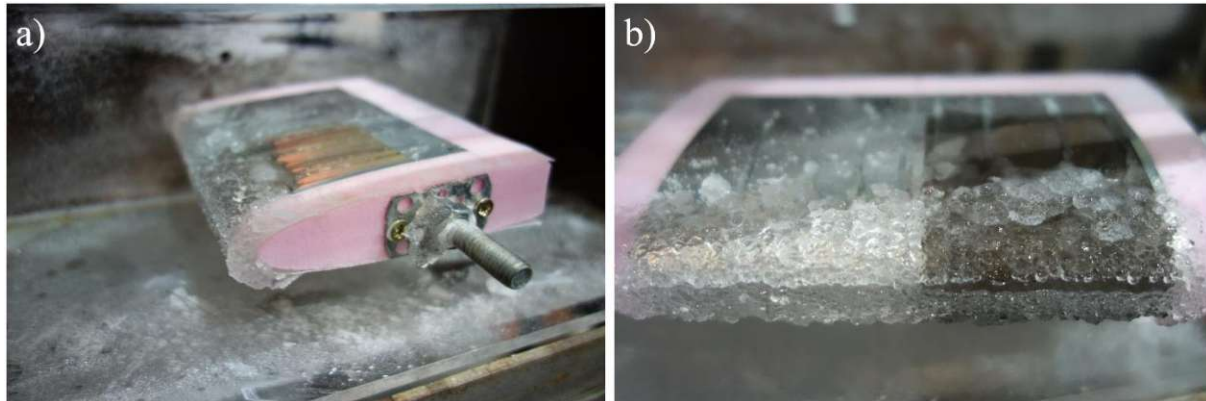


Figure 8. (a) Sample IWT#1 after 180 s of icing under glaze ice conditions, coloration of LIPSS due to diffraction; (b) Detail of the horn-like ice shape on the leading edge, laser-structured sample (right) and reference (left).

Example images of the 3D laser scans and the ice shapes in the leading edge area are shown in Figure 9. Unfortunately, it turned out that the icing time of 180 s was set too long, so the subsequent 3D ice measurement did not represent the delayed formation of ice beads on the laser-structured samples.

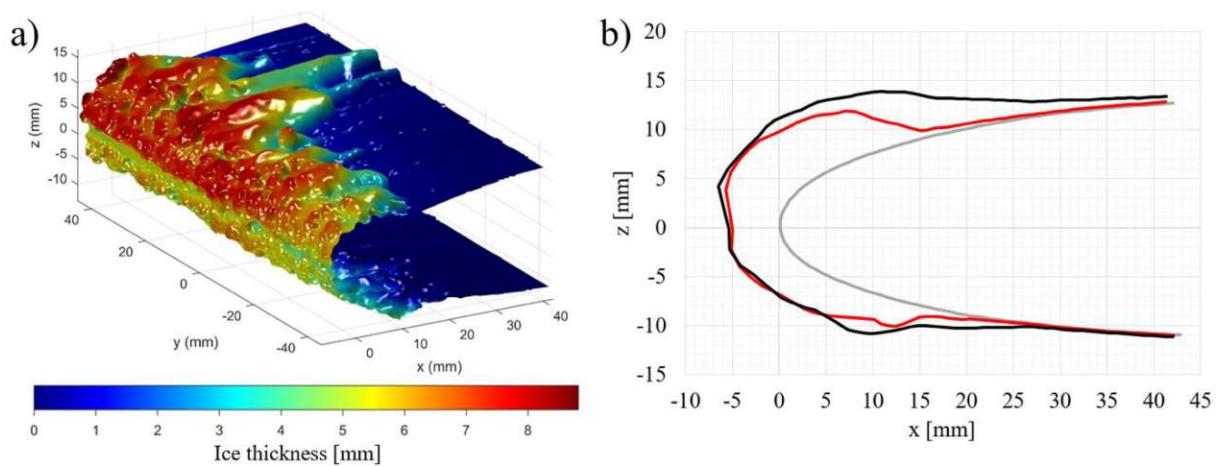


Figure 9. Result of a 3D laser scan of sample IWT#8 after 180 s in the icing wind tunnel; (a) ice accretion as a false color image—structured sample +y direction, reference –y direction; (b) averaged ice accumulation on the cross-section of the NACA 0012 airfoil (bold grey line); laser-structured surface (bold black line) shows increased ice accumulation compared to the reference sample (bold red line).

In contrast to the results of the video analysis, where samples IWT#6, IWT#7 and IWT#8 showed a smoother surface at the leading edge and a significantly delayed formation of ice beads, more ice volume accumulated on these surfaces after the entire test duration of 180 s. Since we did not use a chordwise parting strip between the structured and the reference surfaces, liquid water could have trickled from one side to the other, thereby influencing ice accumulation. Nevertheless, it could be shown that 4 h of Eurosuper petrol immersion could support the runback of impacting water droplets and positively influence the ice shape in the initial icing phase by effectively delaying the formation of beads (Table 3).

3.2. Erosion

A visual inspection of the samples, which had been attached to the rotor blades of a small-scale wind turbine for 6 months of field testing, revealed that they were physically still intact. The structural integrity of the steel foils remained unchanged, although the surface showed a slightly matte appearance. Due to the strong adhesive used to secure the samples on the rotor blades, the samples could not be removed without causing damage. Since the erosion of the blade has its maximum at the leading edge, the 3D topography characterization was therefore focused on these areas [49]. The surface topology was measured with 20 nm vertical and 1 μm lateral resolution. The spatial cut-off frequency λ_c was carefully selected to eliminate the leading edge curvature waveform while including the laser-generated structures in the resulting surface roughness (Table 5). Except for sample E#1, where LIPSS nano-structures were applied, all samples showed a reduction in surface roughness and also in the developed interfacial area ratio (*Sdr*), which describes the increase of surface area due to roughness and structures compared to the planar region. This reduction can be explained by erosion wear during 6 months of testing under cold climate conditions. Usually, the surface of wind turbine rotor blades is kept very smooth to reduce drag and extend the erosion incubation period. The only smooth surface in our experiment was sample E#1 with LIPSS applied. Due to the measurement system's limited lateral resolution, the surface characterization results of sample E#1 did not include the contribution of LIPSS. Further analysis of these structures via SEM and atomic force microscopy (AFM) revealed that LIPSS showed a mean spatial period of 560 nm and a vertical depth of 300 nm, consistent with previous findings for this laser/material combination [50].

Table 5. Surface topography after laser processing and after field testing; *Sa*—arithmetic mean deviation; *Sq*—root mean square height; *Sz*—maximum height; *Sdr*—developed interfacial area ratio; *Sk*—core height.

Sample ID	Structure Type	Cut-off, λ_c (nm)	<i>Sa</i> (nm)	<i>Sq</i> (nm)	<i>Sz</i> (μm)	<i>Sdr</i> (%)	<i>Sk</i> (μm)
E#1 Reference	LIPSS	75	64.4	82.2	0.90	0.08	0.21
E#1 \pm	LIPSS	75	109.8 70.5%	138.0 68.0%	2.24 149.0%	0.14 61.4%	0.30 45.6%
E#2 Reference	Grid	150	1362.9	1816.4	14.32	25.00	3.55
E#2 \pm	Grid	150	1049.8 -23.0%	1301.2 -28.4%	9.93 -30.7%	7.66 -69.3%	3.08 -13.2%
E#3 Reference	Dimple	300	2670.8	3190.6	19.26	136.53	9.66
E#3 \pm	Dimple	300	2448.9 -8.3%	2933.4 -8.1%	22.68 17.8%	66.25 -51.5%	8.28 -14.4%
E#4 Reference	Triangle	150	1604.4	2065.7	16.00	30.42	4.22
E#4 \pm	Triangle	150	1304.0 -18.7%	1685.7 -18.4%	18.95 18.4%	19.51 -35.9%	3.06 -27.5%

Despite this limitation, the increase of *Sa*, *Sz* and *Sdr* indicates erosion wear of surface E#1. This was confirmed by a visual comparison of the unworn reference surface and the sample attached to the rotor blade (Figure 10). The 3D scan reveals macroscopic marks with a depth of about 1 μm on the surface of sample E#1 (Figure 10d,e). SEM analysis showed micrometer- and sub-micrometer-scale scratches and erosion of the LIPSS peaks, resulting in a smeared impression on the SEM images (Figure 10c,d).

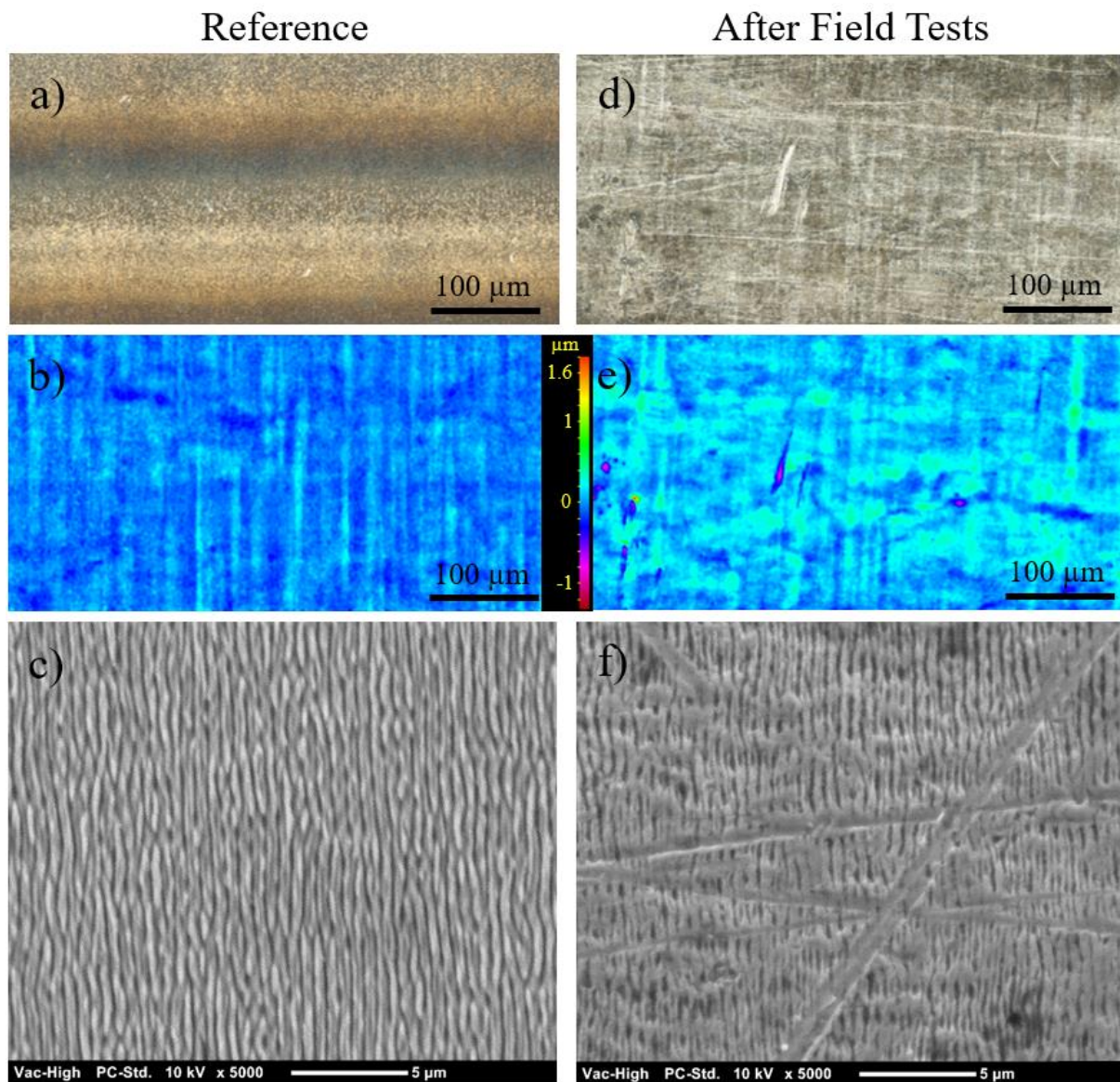


Figure 10. Three-dimensional scan of sample E#1 Reference (left) and sample E#1 after erosion test (right). Image of the measured field (a,d), 3D dataset in false colors (b,e) and SEM images of LIPSS nano-structures (c,f).

The visual inspection of the 3D surface topography of the larger structure types E#2, E#3 and E#4 revealed erosion wear consistent with the measured roughness (Figure 11, Table 5). The false color images indicated a reduction in the penetration depth of the roughness valleys, resulting from a shift of the mean roughness height towards the base material.

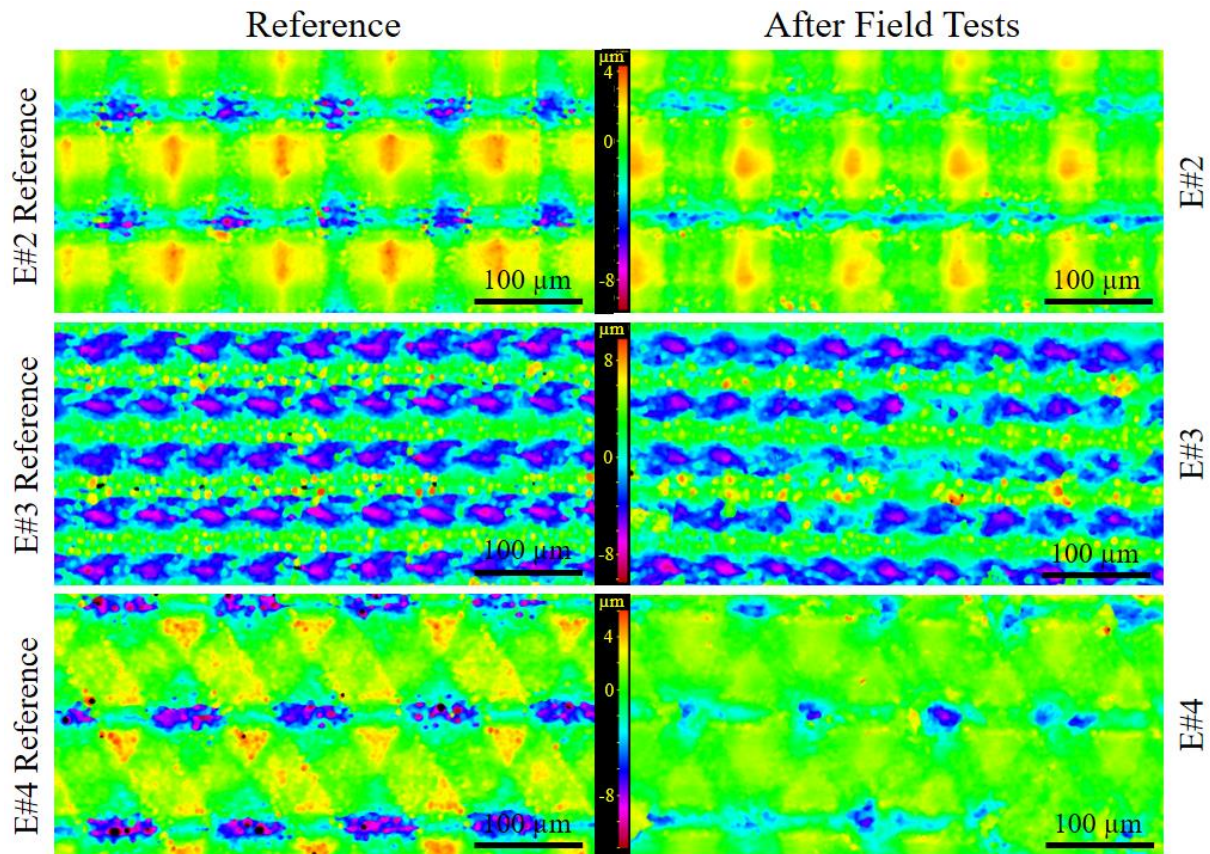


Figure 11. Three-dimensional scan of sample E#2 (grid), E#3 (dimple) and E#4 (triangle); reference samples (left) and eroded samples (right).

To improve laser-structured steel foils for erosion shield applications, other materials than 1.4301 could be investigated. Lee et al. [51], for example, performed droplet impact tests on various steels and demonstrated that erosion rates are coupled to the carbon content of the steel alloy and the surface hardness, where an increase in carbon and hardness leads to a decrease in erosion rate. According to DIN EN 10088-3:2022 the chemical composition of the used 1.4301 steel features a carbon content of 0.07 wt%, we measured a Vickers hardness of 182 HV. Following the correlation by Lee et al. [51], one could increase the lifetime of the laser-structured steel sheets by changing the composition to, e.g., 1.4305, which features a higher carbon content of 0.1 wt% and a ~10% higher hardness.

4. Conclusions

This paper studies the performance and durability of femtosecond laser-structured stainless steel of different topography. The focus was on the effect of the superhydrophobicity on the anti-ice properties under dynamic icing conditions (icing wind tunnel) and the erosion resistance of nano- and micro-structures in a long-term field test. To accelerate the wetting transformation time, improve hydrophobicity and reduce the ice adhesion, surfaces were stored in a vacuum and hydrocarbon liquid (EurosUPER petrol). The main conclusions are as follows:

- Femtosecond-laser-structured and petrol-treated stainless steel surfaces support the runback of impinging water droplets on an airfoil under glaze ice conditions.
- During the initial ice accretion, the petrol-treated samples showed a time delay of 50 s in ice bead build-up on the leading edge compared to the untreated reference surface. The accumulated ice was of a smoother shape, which should lead to improved aerodynamics during that phase.
- Long-term field tests demonstrated a high wear resistance of laser-generated structures on stainless steel, making them interesting for erosion shields in aviation and wind energy.

The measured delay in ice bead build-up could be very beneficial for, e.g., unmanned aerial vehicles (UAVs) which are very sensitive to icing and increase safety margins. Nevertheless, the wind tunnel tests showed an increased ice accumulation compared to the unstructured reference sample after a test duration of 180 s. Furthermore, it turned out that using titanium dioxide powder as a reflection enhancer

for the laser assisted ice shape measurements did deteriorate the microstructures. Further experiments with shorter icing durations are needed to determine the effect of the icing delay and the initial smoother ice surface at the leading edge on the aerodynamics of the wing (drag and lift force measurements, simulations). After the erosion field test, the micro-structures showed slight erosion, resulting in a decreased surface roughness. Wear marks such as scratches of different sizes and depths were found on the LIPSS sample, which led to an increase in surface roughness—the nano-structures were largely preserved. For better erosion resistance, steel with a higher hardness than 1.4301, like 1.4305 could be used. Another approach would be the application of thin layers of erosion resistant material such as metal- or ceramic-nitride compounds, although this impacts surface energy and hence wetting.

Supplementary Materials: The following supporting information can be downloaded at: www.mdpi.com/xxx/s1, Video S1: IWT#1; Video S2: IWT#2; Video S3: IWT#3; Video S4: IWT#4; Video S5: IWT#5; Video S6: IWT#6; Video S7: IWT#7; Video S8: IWT#8.

Author Contributions: Conceptualization, R.F. and G.L.; methodology, R.F.; software, R.F.; validation, R.F. and G.L.; formal analysis, R.F. and G.L.; investigation, R.F.; resources, G.L. and A.O.; data curation, R.F., G.G. and G.L.; writing—original draft preparation, R.F. and G.G.; writing—review and editing, R.F., G.L. and A.O.; visualization, R.F.; supervision, G.L. and A.O.; project administration, G.L. and R.F.; funding acquisition, G.L., R.F. and A.O. All authors have read and agreed to the published version of the manuscript.

Funding: This research has received funding from the Austrian Research Promotion Agency FFG “Take Off” program, project number 43317863 and the Austrian Climate and Energy Fund with FFG project number 871733.

Institutional Review Board Statement: Not applicable.

Informed Consent Statement: Not applicable.

Data Availability Statement: The original contributions presented in the study are included in the article/supplementary material, further inquiries can be directed to the corresponding author/s.

Acknowledgments: The authors acknowledge the FH Joanneum as well as the Austrian Institute for Icing Sciences for their support during the icing wind tunnel tests and the Energiewerkstatt for their contribution to the field tests. The authors also thank the University Service Centre for Transmission Electron Microscopy (USTEM) at TU Wien for their support on scanning electron microscopy. The authors acknowledge Open Access Funding by TU Wien.

Conflicts of Interest: The authors declare no conflicts of interest.

References

1. Muhammed, M.; Virk, M.S. Ice accretion on rotary-wing unmanned aerial vehicles—A review study. *Aerospace* **2023**, *10*, 261. <https://doi.org/10.3390/aerospace10030261>.
2. Kang, W.; Xue, Y.; Tian, H.; Wang, M.; Wang, X. The impact of icing on the airfoil on the lift-drag characteristics and maneuverability characteristics. *Math. Probl. Eng.* **2021**, *2021*, 5568740. <https://doi.org/10.1155/2021/5568740>.
3. Goshima, N.; Maeda, T.; Kamada, Y.; Tada, T.; Hanamura, M.; Pham, H.H.; Iwai, K.; Fujiwara, A.; Hosomi, M. Study on influence of blade icing on operational characteristics of wind turbine at cold climate. *J. Phys. Conf. Ser.* **2020**, *1618*, 052021. <https://doi.org/10.1088/1742-6596/1618/5/052021>.
4. Abdelaal, A.; Nims, D.; Jones, K.; Sojoudi, H. Prediction of ice accumulation on bridge cables during freezing rain: A theoretical modeling and experimental study. *Cold Reg. Sci. Technol.* **2019**, *164*, 102782. <https://doi.org/10.1016/j.coldregions.2019.102782>.
5. Karpen, N.; Diebald, S.; Dezitter, F.; Bonaccorso, E. Propeller-integrated airfoil heater system for small multirotor drones in icing environments: Anti-icing feasibility study. *Cold Reg. Sci. Technol.* **2022**, *201*, 103616. <https://doi.org/10.1016/j.coldregions.2022.103616>.
6. Parent, O.; Ilinca, A. Anti-icing and de-icing techniques for wind turbines: Critical review. *Cold Reg. Sci. Technol.* **2011**, *65*, 88–96. <https://doi.org/10.1016/j.coldregions.2010.01.005>.
7. Goraj, Z. An overview of the deicing and antiicing technologies with respects for the future. In Proceedings of the 24th International Congress of the Aeronautical Sciences, Yokohama, Japan, 29 August–3 September 2004.
8. Staples, C.A.; Boatman, R.J.; Cano, M.L. Ethylene glycol ethers: An environmental risk assessment. *Chemosphere* **1998**, *36*, 1585–1613.
9. Hu, H.; Liu, Y.; Gao, L. *Wind Turbine Icing Physics and Anti-/De-Icing Technology*; Elsevier: Amsterdam, The Netherlands, 2022; ISBN 978-0-12-824532-3.
10. Ramakrishna, D.M.; Viraraghavan, T. Environmental impact of chemical deicers—A Review. *Water Air Soil Pollut.* **2005**, *166*, 49–63. <https://doi.org/10.1007/s11270-005-8265-9>.

11. Hochart, C.; Fortin, G.; Perron, J.; Ilinca, A. Wind turbine performance under icing conditions. *Wind Energy* **2008**, *11*, 319–333. <https://doi.org/10.1002/we.258>.
12. Homola, M.C.; Virk, M.S.; Nicklasson, P.J.; Sundsbø, P.A. Performance losses due to ice accretion for a 5 MW wind turbine. *Wind Energy* **2011**, *15*, 379–389. <https://doi.org/10.1002/we.477>.
13. Seifert, H.; Wsterhellweg, A.; Kröning, J. Risk analysis of ice throw from wind turbines. *Boreas* **2003**, *6*, 2006-01.
14. Morgan, C.; Bossanyi, E.; Seifert, M.H. Assessment of safety risks arising from wind turbine icing. *Boreas* **1998**, *4*, 113–121.
15. Shu, L.; Li, H.; Hu, Q.; Jiang, X.; Qiu, G.; McClure, G.; Yang, H. Study of ice accretion feature and power characteristics of wind turbines at natural icing environment. *Cold Reg. Sci. Technol.* **2018**, *147*, 45–54. <https://doi.org/10.1016/j.coldregions.2018.01.006>.
16. Laakso, T.; Baring-Gould, I.; Durstewitz, M.; Horbaty, R.; Lacroix, A.; Peltola, E.; Ronsten, G.; Tallhaug, L.; Wallenius, T. *State-of-the-Art of Wind Energy in Cold Climates*; VTT: Espoo, Finland, 2010; Volume 152. (In English)
17. Battisti, L.; Fedrizzi, R.; Brighenti, A.; Laakso, T. Sea ice and icing risk for offshore wind turbines. In Proceedings of the OWEMES, Citavecchia, Italy, 20–22 April 2006; pp. 20–22.
18. Gao, L.; Tao, T.; Yongqian, L.; Hui, H. A field study of ice accretion and its effects on the power production of utility-scale wind turbines. *Renew. Energy* **2021**, *167*, 917–928. <https://doi.org/10.1016/j.renene.2020.12.014>.
19. Kjersem, H.A. Estimation of Production Losses Due to Icing on Wind Turbines at Kvitfjell Wind Farm. Master Thesis, Norwegian University of Life Sciences, Ås, Norway, 2019.
20. Huang, X.; Tepylo, N.; Pommier-Budinger, V.; Budinger, M.; Bonaccorso, E.; Villedieu, P.; Bennani, L. A survey of icephobic coatings and their potential use in a hybrid coating/active ice protection system for aerospace applications. *Prog. Aerosp. Sci.* **2019**, *105*, 74–97. <https://doi.org/10.1016/j.paerosci.2019.01.002>.
21. Slot, H.M.; Gelinck, E.R.M.; Rentrop, C.; van der Heide, E. Leading edge erosion of coated wind turbine blades: Review of coating life models. *Renew. Energy* **2015**, *80*, 837–848. <https://doi.org/10.1016/j.renene.2015.02.036>.
22. Soltis, J.; Palacios, J.; Eden, T.; Wolfe, D. Evaluation of Ice-Adhesion Strength on Erosion-Resistant Materials. *AIAA J.* **2015**, *53*, 1825–1835. <https://doi.org/10.2514/6.2013-1509>.
23. Milne, A.J.B.; Amirfazli, A. The Cassie equation: How it is meant to be used. *Adv. Colloid Interface Sci.* **2012**, *170*, 48–55. <https://doi.org/10.1016/j.cis.2011.12.001>.
24. Vercillo, V.; Tonnicchia, S.; Romano, J.-M.; García-Girón, A.; Aguilar-Morales, A.I.; Alamri, S.; Dimov, S.S.; Kunze, T.; Lasagni, A.F.; Bonaccorso, E. Design rules for laser-treated icephobic metallic surfaces for aeronautic applications. *Adv. Funct. Mater.* **2020**, *30*, 1910268. <https://doi.org/10.1002/adfm.201910268>.
25. Fürbacher, R.; Liedl, G. Investigations on the wetting and deicing behavior of laser treated hydrophobic steel surfaces. In Proceedings of the Laser-Based Micro-Nanoprocessing XV, Online, 6–12 March 2021. <https://doi.org/10.1117/12.2578138>.
26. Yang, Z.; Liu, X.; Tian, Y. Insights into the wettability transition of nanosecond laser ablated surface under ambient air exposure. *Adv. Colloid Interface Sci.* **2019**, *533*, 268–277. <https://doi.org/10.1016/j.jcis.2018.08.082>.
27. Hauschwitz, P.; Jagdheesh, R.; Rostohar, D.; Brajer, J.; Kopeček, J.; Jiříček, P.; Houdková, J.; Mocek, T. Hydrophilic to ultrahydrophobic transition of Al 7075 by affordable ns fiber laser and vacuum processing. *Appl. Surf. Sci.* **2020**, *505*, 144523. <https://doi.org/10.1016/j.apsusc.2019.144523>.
28. Cardoso, J.T.; Garcia-Girón, A.; Romano, J.M.; Huerta-Murillo, D.; Jagdheesh, R.; Walker, M.; Dimov, S.S.; Ocaña, J.L. Influence of ambient conditions on the evolution of wettability properties of an IR-, ns-laser textured aluminium alloy. *RSC Adv.* **2017**, *7*, 39617–39627. <https://doi.org/10.1039/c7ra07421b>.
29. Ngo, C.-V.; Chun, D.-M. Fast wettability transition from hydrophilic to superhydrophobic laser-textured stainless steel surfaces under low-temperature annealing. *Appl. Surf. Sci.* **2017**, *409*, 232–240. <https://doi.org/10.1016/j.apsusc.2017.03.038>.
30. Jagdheesh, R.; Diaz, M.; Marimuthu, S.; Ocana, J.L. Robust fabrication of μ -patterns with tunable and durable wetting properties: Hydrophilic to ultrahydrophobic via a vacuum process. *J. Mater. Chem.* **2017**, *5*, 7125–7136. <https://doi.org/10.1039/c7ta01385j>.
31. Fürbacher, R.; Liedl, G.; Otto, A. Fast transition from hydrophilic to superhydrophobic, icephobic properties of stainless steel samples after femtosecond laser processing and exposure to hydrocarbons. *Procedia CIRP* **2022**, *111*, 643–647. <https://doi.org/10.1016/j.procir.2022.08.016>.
32. Kadivar, M.; Tormey, D.; McGranaghan, G. A review on turbulent flow over rough surfaces: Fundamentals and theories. *Int. J. Thermofluids* **2021**, *10*, 100077. <https://doi.org/10.1016/j.ijft.2021.100077>.

33. Flack, K.A.; Schultz, M.P. Review of hydraulic roughness scales in the fully rough regime. *J. Fluids Eng.* **2010**, *132*, 041203. <https://doi.org/10.1115/1.4001492>.
34. Flack, K.A.; Schultz, M.P.; Barros, J.M. Skin friction measurements of systematically-varied roughness: Probing the role of roughness amplitude and skewness. *Flow Turbul. Combust.* **2019**, *104*, 317–329. <https://doi.org/10.1007/s10494-019-00077-1>.
35. Leach, R.K. Surface topography characterization. In *Fundamental principles of engineering nanometrology*, 2nd ed., William Andrew Publishing: Norwich, England, **2014**, pp. 211–262.
36. Prikhod'ko, A.A.; Alekseenko, S.V.; Chmovzh, V.V. Experimental investigation of the influence of the shape of ice outgrowths on the aerodynamic characteristics of the wing. *J. Eng. Phys. Thermophys.* **2019**, *92*, 486–492. <https://doi.org/10.1007/s10891-019-01955-1>.
37. Jung, Y.S.; Baeder, J. Simulations for effect of surface roughness on wind turbine aerodynamic performance. *J. Phys. Conf. Ser.* **2020**, *1452*, 012055. <https://doi.org/10.1088/1742-6596/1452/1/012055>.
38. Bouhelal, A.; Smaïli, A.; Masson, C.; Guerri, O. Effects of surface roughness on aerodynamic performance of horizontal axis wind turbines. In Proceedings of the 25th Annual Conference of the Computational Fluid Dynamics Society of Canada, CFD2017-337, Windsor, ON, Canada, 18–21 June 2017.
39. Tagawa, G.B.S.; Morency, F.; Beaugendre, H. CFD investigation on the maximum lift coefficient degradation of rough airfoils. *AIMS Energy* **2021**, *9*, 305–325. <https://doi.org/10.3934/energy.2021016>.
40. Han, W.; Kim, J.; Kim, B. Study on correlation between wind turbine performance and ice accretion along a blade tip airfoil using CFD. *J. Renew. Sustain. Energy* **2018**, *10*, 023306. <https://doi.org/10.1063/1.5012802>.
41. Zeng, D.; Li, Y.; Huan, D.; Liu, H.; Luo, H.; Cui, Y.; Zhu, C.; Wang, J. Robust epoxy-modified superhydrophobic coating for aircraft anti-icing systems. *Coll. Surf. A Phys. Eng. Asp.* **2021**, *628*, 127377. <https://doi.org/10.1016/j.colsurfa.2021.127377>.
42. Puffing, R.F.A.; Peciar, M.; Hassler, W. Instrumentation of an icing wind tunnel based on SAE standards. *Sci. Proc. Fac. Mech. Eng. STU* **2013**, *21*, 37–43. <https://doi.org/10.2478/stu-2013-0007>.
43. Thomareis, N.; Papadakis, G. Effect of trailing edge shape on the separated flow characteristics around an airfoil at low Reynolds number: A numerical study. *Phys. Fluids* **2017**, *29*, 014101. <https://doi.org/10.1063/1.4973811>.
44. Hu, J.; Wang, Z.; Zhao, W.; Sun, S.; Sun, C.; Guo, C. Numerical simulation on vortex shedding from a hydrofoil in steady flow. *J. Mar. Sci. Eng.* **2020**, *8*, 195. <https://doi.org/10.3390/jmse8030195>.
45. Fortin, G.; Ilinca, A.; Laforte, J.-L.; Brandi, V. New roughness computation method and geometric accretion model for airfoil icing. *J. Aircr.* **2004**, *41*, 119–127. <https://doi.org/10.2514/1.173>.
46. Airworthiness standards: Transport category airplanes. In *Code of Federal Regulations, Title 14, Chapter I, Subchapter C, Part 25, Appendix C*, 1-1-23 edition, Federal Aviation Administration: Washington, DC, USA, **2023**.
47. Kozomara, D.; Amon, J.; Puffing, R.; Neubauer, T.; Schweighart, S.; Diebald, S.; Rapf, A.; Moser, R.; Breiffuss, W. Experimental investigation of UAS rotors and ice protection systems in appendix C icing conditions. In Proceedings of the International Conference on Icing of Aircraft, Engines, and Structures, Vienna, Austria, 20–23 June 2023; SAE Technical Paper Series. <https://doi.org/10.4271/2023-01-1380>.
48. Kozomara, D.; Neubauer, T.; Puffing, R.; Bednar, I.; Breiffuss, W. Experimental investigation on the effects of icing on multicopter UAS operation. In Proceedings of the AIAA AVIATION, Virtual, 2–6 August 2021. <https://doi.org/10.2514/6.2021-2676>.
49. Liersch, L.; Michael, J. Investigation of the impact of rain and particle erosion on rotor blade aerodynamics with an erosion test facility to enhancing the rotor blade performance and durability. *J. Phys. Conf. Ser.* **2014**, *524*, 012023. <https://doi.org/10.1088/1742-6596/524/1/012023>.
50. Fuerbacher, R.; Liedl, G.; Murzin, S.P. Experimental study of spatial frequency transition of laser induced periodic surface structures. *J. Phys. Conf. Ser.* **2021**, *1745*, 012017. <https://doi.org/10.1088/1742-6596/1745/1/012017>.
51. Lee, G.M.C. The erosion resistance of plain carbon steels under water droplet impact conditions. *Wear* **1990**, *141*, 185–201.

Disclaimer/Publisher's Note: The statements, opinions and data contained in all publications are solely those of the individual author(s) and contributor(s) and not of MDPI and/or the editor(s). MDPI and/or the editor(s) disclaim responsibility for any injury to people or property resulting from any ideas, methods, instructions or products referred to in the content.